

# **Measurement of Atmospheric NO<sub>y</sub> Species Using Active and Lunar DOAS in an Urban and Forested Region**

Kevin M. Nikelski

A thesis submitted to the Faculty of Graduate Studies in partial  
fulfillment of the requirement for the degree of Master of Science

Graduate Program in Chemistry

York University

Toronto, Ontario

March, 2016

©Kevin Nikelski, 2016

## Abstract

The study of  $\text{NO}_y$  serves as an important undertaking in the understanding of both night and daytime atmospheric processes. Two separate datasets were collected over the course of this research using Differential Optical Absorption Spectroscopy. In the first study,  $\text{NO}_3$  vertical column densities (VCDs) determined using lunar DOAS were analysed in conjunction with surface mixing ratios found using active DOAS on two separate nights during the summer of 2015 to quantify the  $\text{NO}_3$  vertical profile present at York University. The second study focused on the determination of HONO mixing ratios based on full-day active DOAS measurements performed in a forested region at the AMS13 site near Fort McMurray, Alberta during a joint field study with Environment Canada. The average diurnal profile of HONO found in this study (and various other species) was used for calculating the daytime production of OH radical through HONO photolysis compared to other OH production mechanisms.

## Acknowledgments

I will admit, I was unsure what exactly I would find when I came to Toronto two years ago. I can say with certainty, however, that one of the most pleasant surprises is the abundance of wonderful people that supported me throughout my graduate work here at York University.

For initially giving me the chance to be here, giving me direction over the course of my project, and for acting as driver for many of our scientific adventures, I thank my supervisor, Dr. Robert McLaren. Your infectious good humor made it worth coming into work, even when things went wrong. You have my deepest gratitude.

I would also like to thank the other members of the McLaren group for the keen insight and enjoyable company. Thanks to Sabour Baray, Zoe Davis, and Ibraheem Nuaaman. In addition, the group had many excellent undergraduate research members. Special thanks go to Akshay Lobo and William Fujs, who I wish all the best for in medical school and graduate studies respectively.

It was a pleasure to be a part of the Centre of Atmospheric Chemistry here at York. It afforded me many opportunities that would not have been available otherwise. With this in mind, I would like thank Carol Weldon for her support in putting together the many events and trips I took part in over the course of my time here.

Of course, gratitude is not limited to those in Toronto. I would like to thank my parents and sister in British Columbia for the constant encouragement (and occasional gift-basket). I'm lucky to have you. Always have been.

A last thank you is necessary. To Brian Marshall Nikelski. This is the sum of many days and nights lived. There were good days and bad days. Moments of glorious success and crushing failure. All were worth it. All will continue to be worth it. That is the truth I present to you.

## Table of Contents

|   |               |
|---|---------------|
| Abstract .....  | ii            |
| Acknowledgments .....   | iii           |
| Table of Contents .....   | v             |
| List of Tables.....   | vii           |
| List of Figures .....   | viii          |
| <b>Chapter 1: Introduction.....</b>   | <b>- 1 -</b>  |
| <b>1.1: Structure of the Atmosphere.....</b>  | <b>- 3 -</b>  |
| <b>1.2: Oxides of Nitrogen in the Atmosphere:.....</b>  | <b>- 5 -</b>  |
| <b>1.3: The Nitrate Radical and Dinitrogen Pentoxide .....</b>  | <b>- 9 -</b>  |
| <b>1.4: Nitrous Acid.....</b>   | <b>- 17 -</b> |
| <b>1.5: Differential Optical Absorption Spectroscopy .....</b>  | <b>- 23 -</b> |
| <b>Chapter 2: Experimental .....</b>  | <b>- 29 -</b> |
| <b>2.1: Active DOAS Analysis .....</b>  | <b>- 29 -</b> |
| <b>2.1.1: Instrumental Set-up of Active DOAS.....</b>   | <b>- 29 -</b> |
| <b>2.1.2: Spectral Analysis Software.....</b>   | <b>- 30 -</b> |
| <b>2.1.3: Electronic Offset, Dark Current and Calibration Spectra.....</b>                              | <b>- 31 -</b> |
| <b>2.1.4: Xe Lamp Spectra.....</b>  | <b>- 35 -</b> |
| <b>2.1.5: HONO Fit Scenario.....</b>  | <b>- 36 -</b> |
| <b>2.1.6: Use of Two-Lamp Fit.....</b>  | <b>- 37 -</b> |
| <b>2.1.7: AMS13 Site .....</b>  | <b>- 39 -</b> |
| <b>2.2: Combined Active and Lunar DOAS Measurement .....</b>  | <b>- 40 -</b> |
| <b>2.2.1: Location and Instrumentation .....</b>  | <b>- 42 -</b> |
| <b>2.2.2: Lunar DOAS Fitting Procedure: .....</b>   | <b>- 45 -</b> |
| <b>2.2.3: NO<sub>3</sub> fitting procedure for lunar DOAS:.....</b>                                     | <b>- 46 -</b> |
| <b>2.2.4: NO<sub>3</sub> and NO<sub>2</sub> fitting procedure for active DOAS measurements:.....</b>    | <b>- 47 -</b> |
| <b>2.2.5: Temperature Dependence of NO<sub>3</sub> Cross Section: .....</b>                             | <b>- 48 -</b> |
| <b>2.2.6: NO<sub>x</sub> and O<sub>3</sub> measurement by chemiluminescence and UV photometry .....</b> | <b>- 50 -</b> |
| <b>2.2.7: Meteorological Measurements at York University .....</b>                                      | <b>- 51 -</b> |
| <b>Chapter 3: NO<sub>3</sub> Measurement at York University.....</b>                                    | <b>- 52 -</b> |
| <b>3.1: Measurement overview.....</b>   | <b>- 52 -</b> |
| <b>3.2: June 3<sup>rd</sup>-4<sup>th</sup> case study.....</b>  | <b>- 53 -</b> |
| <b>3.2: July 2<sup>nd</sup>-3<sup>rd</sup> case study .....</b>   | <b>- 58 -</b> |

|  |        |
|--|--------|
| <b>3.3: Stratospheric NO<sub>3</sub> levels on selected nights</b> .....               | - 61 - |
| <b>3.4: Vertical Distribution of NO<sub>3</sub></b> .....                              | - 63 - |
| <b>3.5: NO<sub>3</sub> VCDs taken in March 2011</b> .....                              | - 66 - |
| <b>Chapter 4: HONO Measurement at AMS13 site</b> .....                                 | - 71 - |
| <b>4.1: Measurement overview</b> .....   | - 71 - |
| <b>4.2: Method Development of Two Lamp Fitting Scenario</b> .....                      | - 72 - |
| <b>4.3: HONO mixing ratios from Aug 17<sup>th</sup> - Sept 4<sup>th</sup></b> .....    | - 77 - |
| <b>4.4: Diurnal profile of HONO at AMS13</b> .....                                     | - 83 - |
| <b>4.5: Determination of daytime levels and radical production rates of HONO</b> ..... | - 85 - |
| <b>4.6: Importance of HONO as an OH source</b> .....                                   | - 88 - |
| <b>4.7: Comparison of forested and urban HONO mixing ratios</b> .....                  | - 93 - |
| <b>Chapter 5: Conclusions and Future Work</b> .....                                    | - 96 - |
| <b>Chapter 6: References</b> .....   | - 98 - |

## List of Tables

### Chapter 2:

Table 2.1: AMS13 lamp spectra (collected in triplicate) ----- - 36 -

Table 2.2: Summary of calculated NO<sub>3</sub> cross sections and percent difference at varying temperatures----- - 49 -

### Chapter 3:

Table 3.1: Vertical distribution of NO<sub>3</sub> for both nights of analysis from 3:00-4:00 am ----- - 65 -

Table 3.2: Vertical distribution of NO<sub>3</sub> for March 19<sup>th</sup>, 2011 of from 3:40-4:40 am ----- - 68 -

### Chapter 4:

Table 4.1: HONO fit concentrations and chi-squared values fitting the Aug 17<sup>th</sup> ----- - 72 -

Table 4.2: Comparison of one-lamp and two lamp fits using lamp spectrum ----- - 75 -

Table 4.3: Comparison of average [HONO]<sub>PSS</sub> mixing ratios calculated using the PSS assumption 12:00pm-1:00pm and measured values----- - 87 -

Table 4.4: Summary Table of HONO and NO<sub>2</sub> mixing ratios from Aug 17<sup>th</sup>-Sept 4<sup>th</sup>----- - 93 -

Table 4.5: Comparison of median nighttime NO<sub>2</sub> and HONO mixing at (AMS13) and (York University) ----- - 94 -

## List of Figures

### Chapter 1:

|   |      |
|---|------|
| Figure 1.1: Schematic of the diurnal variation and dynamics of the Planetary Boundary Layer ---                                       | 5 -  |
| Figure 1.2 Nitrogen Oxide emission (1990-2013) (EC, 2013). -----  | 6 -  |
| Figure 1.3: Reaction Schematic for Atmospheric Processes Involving NO <sub>3</sub> and N <sub>2</sub> O <sub>5</sub> -----            | 10 - |
| Figure 1.4: Left: Profile of NO <sub>3</sub> and N <sub>2</sub> O <sub>5</sub> and potential temperature as a function of height ---- | 11 - |
| Figure 1.5: Diagram of Heterogeneous Hydrolysis of NO <sub>2</sub> (Source: Finlayson-Pitts 2003)-----                                | 21 - |
| Figure 1.6: Principle of DOAS -----   | 25 - |

### Chapter 2:

|  |      |
|--|------|
| Figure 2.1: Active DOAS apparatus used at AMS13 -----  | 30 - |
| Figure 2.2: Sample offset spectra collected Aug 20 <sup>th</sup> -----   | 32 - |
| Figure 2.3: Sample dark current spectra collected Aug 20 <sup>th</sup> 2013-----                                       | 33 - |
| Figure 2.4: Sample Hg lamp spectra taken Aug 20 <sup>th</sup> 2013 -----   | 34 - |
| Figure 2.5: High pressure Xe-arc lamp-----   | 35 - |
| Figure 2.6: HONO cross section Fit range (337-361 nm)-----   | 36 - |
| Figure 2.7: Solar background spectra used for daytime HONO fitting. Collected Aug 22 <sup>nd</sup> at 1:18<br>pm ----- | 37 - |
| Figure 2.8: DOASIS HONO fit output measured on Aug 21 <sup>st</sup> / 2013 at 10:06 pm-----                            | 39 - |
| Figure 2.9: AMS13 Measurement Site. Distance from Major Mining Facilities ~ 12 km -----                                | 40 - |
| Figure 2.10 Site Location for active and lunar measurement of NO <sub>3</sub> at York University -----                 | 43 - |
| Figure 2.11: Sample Hg lamp / laser spectra taken July 2 <sup>nd</sup> 2015 -----                                      | 46 - |
| Figure 2.12: DOASIS NO <sub>3</sub> fit output taken on July 2 <sup>nd</sup> 2015 -----                                | 47 - |

### Chapter 3:

|   |      |
|---|------|
| Figure 3.1: NO <sub>3</sub> VCDs collected on June 3 <sup>rd</sup> 2015 -----   | 53 - |
| Figure 3.2: NO <sub>3</sub> mixing ratios determined using active DOAS at the 56m beam height on June 3 <sup>rd</sup> ---<br>54 -   | 54 - |
| Figure 3.3: $\Delta T$ (9.5m-1.0m), wind speed, [O <sub>3</sub> ], [NO], [NO <sub>2</sub> ], and [NO <sub>2</sub> + O <sub>3</sub> ] June 3 <sup>rd</sup> -4 <sup>th</sup> , 2015- 56 - | 56 - |
| Figure 3.4: NO <sub>3</sub> VCDs collected on July 2 <sup>nd</sup> 2015-----  | 58 - |
| Figure 3.5: NO <sub>3</sub> mixing ratios determined using active DOAS at the 16m beam height on July 2 <sup>nd</sup> ----<br>59 -  | 59 - |
| Figure 3.6: $\Delta T$ (9.5m-1.0m), wind speed, [O <sub>3</sub> ], [NO], [NO <sub>2</sub> ], and [NO <sub>2</sub> + O <sub>3</sub> ] July 2 <sup>nd</sup> -3 <sup>rd</sup> -----        | 60 - |
| Figure 3.7: Global Distribution of NO <sub>3</sub> (25-50km) in 2003 (Hauchecorne et al. 2005) -----  | 62 - |
| Figure 3.9: NO <sub>3</sub> VCDs collected on March 19 <sup>th</sup> 2011. Sunrise occurs at 7:21 am-----   | 67 - |
| Figure 3.10: NO <sub>3</sub> , O <sub>3</sub> , and NO <sub>2</sub> mixing ratios collected using active DOAS March 19 <sup>th</sup> /2011 -----  | 68 - |
| Figure 3.11: Pie chart showing vertical distribution of NO <sub>3</sub> from 3:40-4:40am -----  | 69 - |

## Chapter 4:

|   |        |
|---|--------|
| Figure 4.1: Fit residual for fitted lamp spectra collected on Aug 17th in the 337-361 nm range excluding HONO from the fit.-----                  | - 73 - |
| Fig 4.2: Median night-time lamp fit coefficients Aug 29th-Sept 5th -----  | - 74 - |
| Figure 4.3: Fit residual for single and two lamp fits of Sept 5 <sup>th</sup> lamp spectrum -----   | - 76 - |
| Figure 4.4: HONO (10-minute averages) and NO <sub>2</sub> (2-minute averages) Aug 17 <sup>th</sup> -Sept 4 <sup>th</sup> -----                    | - 78 - |
| Figure 4.5: Wind speed and direction Aug 21 <sup>st</sup> at AMS13 -----  | - 79 - |
| Figure 4.6: Concentration of atmospheric species from 8:00pm Aug 21 <sup>st</sup> to 12:00pm Aug 22 <sup>nd</sup> --                              | - 81 - |
| Figure 4.7: HONO/NO <sub>2</sub> ratio for Aug 21st night-----  | - 82 - |
| Figure 4.8: Diurnal HONO profile at AMS13 Aug 17 <sup>th</sup> -Sept 4 <sup>th</sup> -----  | - 83 - |
| Figure 4.9: Diurnal HONO, NO <sub>2</sub> and HONO/NO <sub>2</sub> Ratio -84-   |        |
| Figure 4.10: <i>j</i> HONO Values at the AMS13 site from Aug 17th-Sept 4th- 86 -  |        |
| Figure 4.11: Comparison of OH production at AMS13 site -----  | - 90 - |
| Figure 4.12: Pie charts showing the relative importance of primary radical sources during the full day (left) and the early morning (right) ----- | - 91 - |
| Figure 4.13: Summary of observed HONO mixing ratios at noon (black) and calculated unknown daytime HONO sources (blue) - 95 -                     |        |

# Chapter 1: Introduction

The field of atmospheric chemistry and physics is a difficult area of study due to the fact that complicated physical and chemical mechanisms that work on both a local and global scale must be taken into account in order to determine the sources, sinks and transformation of pollutants present in the air we breathe. Differences between urban and rural environments in regards to the level of anthropogenic influence can show the impact of human changes to air quality, both in the immediate sense, and over the past two centuries of human advancement since the industrial revolution. Atmospheric chemistry has long been associated with daytime phenomena, such as photochemical smog (Finlayson-Pitts and Pitts Jr., 1999), ozone formation (Middleton et al., 1950), acid rain and the formation of secondary organic aerosol (SOA) (Vairavamurthy, Roberts et al., 1992). However the active chemistry that occurs in the atmosphere at night plays an equally important role in the observed gas and radical budgets observed in the atmosphere. Of particular importance are nitrogen oxide species ( $\text{NO}_y$ ), which are highly prevalent throughout the lower atmosphere. This is especially true in urban areas, in which  $\text{NO}_x$  [ $\text{NO} + \text{NO}_2$ ] can be released through a large number of natural and anthropogenic processes. Over the course of the night, nitrogen oxides plays a key role in several active chemical processes. The discovery of the nitrate radical within the nocturnal troposphere (Noxon et al., 1978, 1980, Platt et al. 1980), as well as the non-negligible presence of OH,  $\text{HO}_2$  and  $\text{RO}_2$  radicals during the night through the reaction of  $\text{NO}_3$  and  $\text{O}_3$  with unsaturated hydrocarbons (Cantrell et al. 1992, Vairavamurthy, Roberts et al., 1992) show that nocturnal processes play a key role in overall atmospheric composition of a given location. Likewise the interaction with  $\text{NO}_2$  with moist surfaces can produce nitrous acid ( $\text{HONO}$ ) (Finlayson-Pitts et al., 2003, Spataro

et al., 2014). This species acts as a nighttime reservoir for the OH radical, and subsequently undergoes rapid photolysis in the early morning (Harris et al., 1984, Young et al., 2012). This is of particular importance due to the fact that HONO can dominate as an early morning source of radicals over other daytime sources, such as ozone photolysis. For this reason, accurate measurement of nocturnal nitrogen species ( $\text{NO}_y$ ) is of significant importance in understanding radical and trace gas chemistry not only over the course the night, but also during the following daytime hours. Effective measurement of reactive trace gases in the atmosphere benefits from non-invasive instrumental techniques that suffer fewer interferences. For this research, Differential Optical Absorption Spectroscopy (DOAS) was used for the experimental analysis of nocturnal nitrogen oxide species. This technique makes use of the attenuation of light by trace gases in the atmosphere to determine their mixing ratios (Platt and Stutz, 2008). The light source used experimentally can be from an artificial light source (active), or from reflected, scattered or direct sun light (passive). Two separate research projects were performed over the course of this work. The first focused on the nighttime measurement of  $\text{NO}_3$  at York University using a combination of active and passive lunar DOAS. The primary aim was have simultaneous measurement of  $\text{NO}_3$  levels both from multiple points in the surface layer of the atmosphere, a total column measurement of  $\text{NO}_3$  in the troposphere and stratosphere. This would allow the determination of the column abundance of  $\text{NO}_3$  present in the residual layer (e.g. approximately 0.1 – 1.0 km a.s.l) at night if the quantity of  $\text{NO}_3$  present within the stratosphere is known. The second project focuses on the determination of HONO mixing ratios via active DOAS in a forested region directly impacted by Oil Sands processing close to Fort McKay, Alberta. The data were obtained as part of a joint field study with Environment Canada and multiple university research groups in the summer of 2013. Datasets for  $\text{NO}_2$  and  $\text{SO}_2$  were processed previously from the raw data by another student researcher (Akshay Lobo). Given that greater mixing ratios

of nitrous acid have been observed at ground level rather than aloft, measurement of point mixing ratios at the surface have value in the determination of potential impact which Oil Sands processing can have on both the night and daytime atmosphere in the Oil Sands region.

## 1.1: Structure of the Atmosphere

Due to diminishing mass of atmospheric gas with increasing altitude, atmospheric pressure is observed to decrease exponentially with height. Combined with variations in temperature, these factors act to divide the atmosphere into four layers: the troposphere, stratosphere, mesosphere and thermosphere. The troposphere is the region closest to the Earth's surface, and contains roughly 85% of its total mass, as well as 99% of its water vapour and aerosols. It extends from the ground to heights of ~ 10 km in the high latitudes, and 20 km in equatorial regions. The temperature lapse rate in this region is found to  $\sim 6^{\circ}\text{C km}^{-1}$ , slightly smaller than the adiabatic lapse rate of  $9.8^{\circ}\text{C km}^{-1}$ . The tropopause is located at an altitude of 10-15km, and consists of an isothermal zone of air with a temperature of  $-55^{\circ}\text{C}$ . The tropopause serves as a boundary separating the troposphere and stratosphere. The stratosphere contains majority of atmospheric ozone, and extends from the tropopause to roughly 50km a.s.l. Due to the absorption of UV-radiation by  $\text{O}_3$  a temperature inversion is observed in the stratosphere, as temperature is observed to increase with height. This inversion region, acts to prevent the vertical currents of the troposphere from spreading to the stratosphere. Since the troposphere is the closest region to the Earth's surface, the majority of the human produced atmospheric pollutants and their sources are located in this area. Additionally, determination of the total column abundance of  $\text{NO}_3$  may allow a rough determination of the component of the radical

species present in the lower stratosphere, which plays a crucial role in the nitrogen and ozone chemistry (see section 1.3). For this reason, the research presented in this thesis will focus upon these two layers of the atmosphere.

The region of the troposphere that is closest to the surface, and therefore is directly impacted by planetary emissions, is known as the Planetary Boundary Layer (PBL). A difficulty that arises when discussing nocturnal chemistry in the troposphere is the diurnal variation in solar radiation. Atmospheric turbulence via convection and wind shear leads to a well-mixed daytime PBL in the summer, though not necessarily in the winter. As the sun sets, the surface cools due to radiative energy loss, while the air above cools more slowly. The ensuing temperature gradient results in suppressed vertical mixing in the PBL, which inhibits upward transport of trace gases. This leads to the formation of the Nocturnal Boundary Layer inversion (NBL) at roughly 50-200 m above the surface. The NBL is characterized by the formation of a temperature inversion of warm buoyant air remaining above the cooler dense air at the surface. Between the top of the NBL and the free troposphere a residual layer forms, which contains air from the previous day decoupled from the ground. Trace gases can accumulate in the NBL before solar heating of the surface begins again during the morning. The subsequent breakup of the nocturnal temperature inversion by convection allows the reformation of the well mixed PBL.

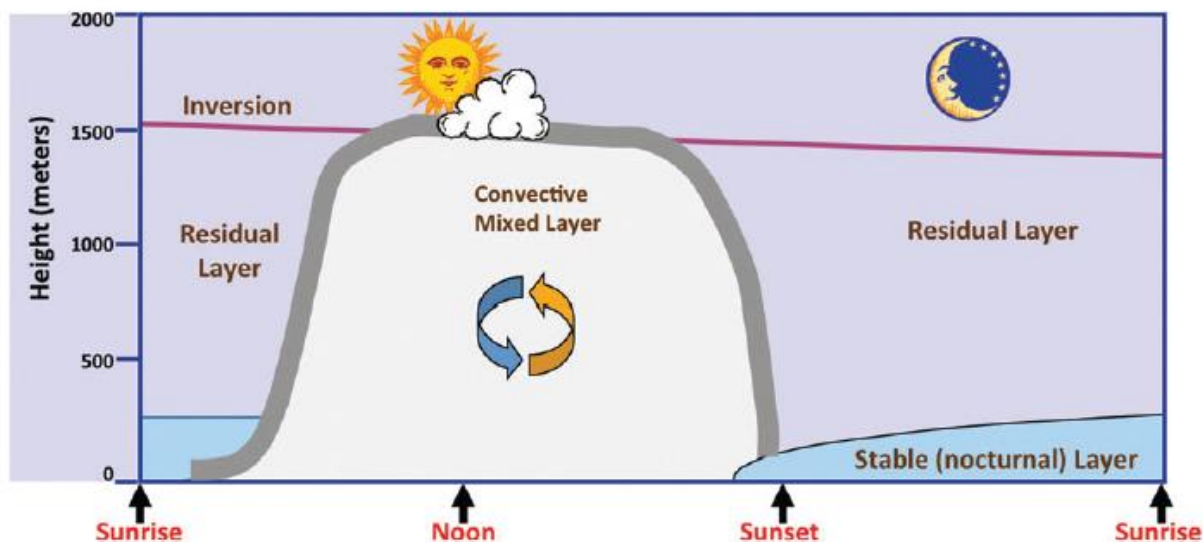


Figure 1.1: Schematic of the diurnal variation and dynamics of the Planetary Boundary Layer (Brown, S.S. and Stutz, J., 2012)

## 1.2: Oxides of Nitrogen in the Atmosphere:

The oxides of nitrogen  $\text{NO}$  and  $\text{NO}_2$  (defined as  $\text{NO}_x$ ) are key species in the chemistry of the lower atmosphere and significantly impact the degradation of most pollutants in both clean air and polluted regions. Along with  $\text{HO}_x$ , nitrogen oxides play a leading role in controlling the budget of tropospheric  $\text{O}_3$  (IPCC 2014), the production of the OH-radical and the formation of organic nitrates and nitrites through reaction with hydrocarbon degradation products.

Nitric oxide is by far the most significant species emitted by anthropogenic processes. It is primarily produced through the reaction of  $\text{N}_2$  and  $\text{O}_2$  in air during high temperature combustion processes. Small quantities of  $\text{NO}_2$  are likewise produced:



The fraction of NO to NO<sub>2</sub> produced from a given anthropogenic process varies based on the type of combustion, as well as the reaction conditions and type of fuel. While the majority of NO<sub>x</sub> emission is believed to be in the form of NO (>90%), the fraction of NO<sub>2</sub> emitted can range from 1-30% (Lenner, 1987). In Canada, anthropogenic emission of NO<sub>x</sub> was estimated to be 2061 kilotonnes in 2013 (figure 1.2), decreasing by 28% from 1990 levels (EC 2013).

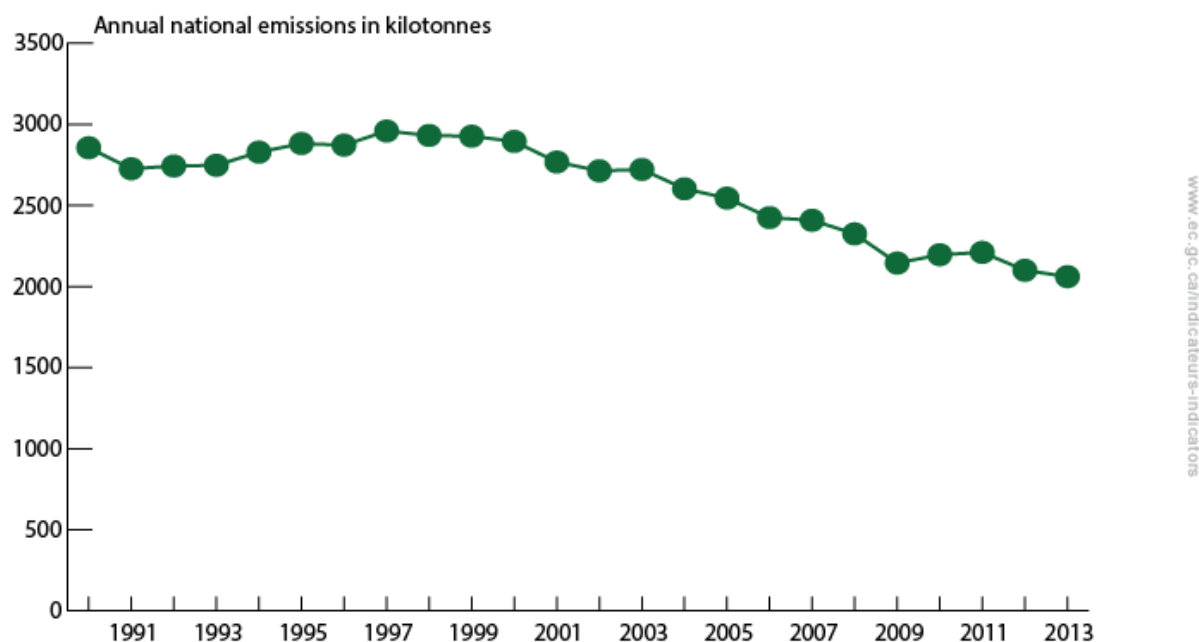
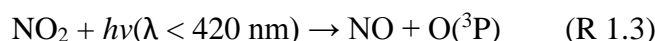


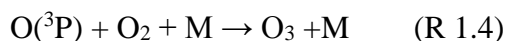
Figure 1.2 Nitrogen Oxide emission (1990-2013) (EC, 2013).

The primary anthropogenic source of NO<sub>x</sub> in 2013 can be attributed to transportation sources (road, off-road, rail, air, and marine), representing 55.5% of total national emissions. The remaining sources include industry (24.2 %), fuel from electricity and heating (10.6 %), and incineration of organic and inorganic matter, as well as other miscellaneous sources (9.7 %). The overall decrease in NO<sub>x</sub> emissions from transport over the years can be attributed to the progressive introduction of newer emission controls for vehicles. The largest increase observed over time is found to be in emissions from the oil and gas industry.

The photolysis of NO<sub>2</sub> and the OH-catalyzed reactions between NO<sub>x</sub> and hydrocarbon radicals acts as the major source of tropospheric ozone from anthropogenic sources. Under clear-sky conditions, the average lifetime of a NO<sub>2</sub> molecule is only on the order of ~ 2 min. at mid-latitudes [ $j_{\text{NO}_2} \approx 8 \cdot 10^{-3} \text{s}^{-1}$ ] Junkermann et al. 1989]. The resulting photolysis of NO<sub>2</sub> in the troposphere produces a ground state oxygen atom with two unpaired electrons O(<sup>3</sup>P) through the following reaction:



O(<sup>3</sup>P) then reacts rapidly with O<sub>2</sub> to form ozone:



where M denotes any atmospheric molecule that dissipates the unstable energy of the newly formed O<sub>3</sub> molecule. Tropospheric O<sub>3</sub> is a component of smog that is responsible for a variety of adverse health effects in humans, animals, and plants. In particular, it can act to aggravate asthma and increase susceptibility of respiratory infections and inflammation. Tropospheric ozone is also an important greenhouse gas, as well as a precursor to the OH radical, due to its oxidative nature:



Reaction of O<sub>3</sub> with NO rapidly oxidizes it back to NO<sub>2</sub>:



Thus, in high NO<sub>x</sub> environments, O<sub>3</sub> is rapidly removed from the troposphere through reaction with NO. The impact of NO<sub>x</sub> emissions on nighttime O<sub>3</sub> loss is assessed by nocturnal tropospheric odd oxygen (O<sub>x</sub>), defined as O<sub>3</sub> + NO<sub>2</sub> + 2NO<sub>3</sub> + 3N<sub>2</sub>O<sub>5</sub> (Brown et al. 2006). Ozone depletion is particularly prevalent during nights in which a shallow and stable nocturnal boundary

layer has formed, when the destruction of O<sub>3</sub> through reaction of surface emitted NO acts in addition to the dry deposition of ozone on surfaces. A well-mixed planetary boundary layer may reduce O<sub>3</sub>, due the dilution of NO into a larger air mass.

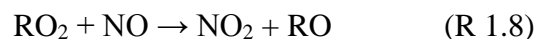
In the absence of organic compounds Reaction R 1.3, 1.4, and 1.7 lead to a photo-stationary state between O<sub>3</sub>, NO, and NO<sub>2</sub> during daylight hours. The relationship between the three species is defined by the Leighton ratio (Leighton 1961):

$$\frac{[NO][O_3]}{[NO_2]} = \frac{j_{NO_2}}{k_{(NO+O_3)}} \quad (E 1.1)$$

The ratio NO<sub>2</sub> to NO can therefore be given as:

$$\frac{[NO_2]}{[NO]} = [O_3] \cdot \frac{k_{(NO+O_3)}}{j_{NO_2}} \quad (E 1.2)$$

It can be seen from the above ratio that the key factor in tropospheric ozone formation is the chemical conversion of NO to NO<sub>2</sub>. The sum of O<sub>3</sub> and NO<sub>2</sub> are referred to as odd oxygen (O<sub>x</sub>). This sum remains constant given that O<sub>3</sub>, NO, and NO<sub>2</sub> mixing ratios are balanced by the Leighton ratio. As a result, no net ozone forms from reactions R 1.3, 1.4, and 1.7. The presence of VOC and free radical species in the atmosphere act to interfere with the Leighton relationship by converting NO to NO<sub>2</sub> without also destroying an O<sub>3</sub> molecule, leading to net ozone production. This includes reaction of NO with peroxy radical species (RO<sub>2</sub> and HO<sub>2</sub>) produced through OH-initiated oxidation of hydrocarbons in the troposphere:



The Leighton ratio undergoes daily variation due to varying  $\text{NO}_2$  photolysis rates as function of solar zenith angle (SZA). Non-chemical processes and fluxes in ground level NO sources can also act to allow the formation of tropospheric  $\text{O}_3$ . During sunrise and sunset, the rate of photolysis is slow, and thus the assumption of a photo-stationary state is found to be invalid (Calvert and Stockwell, 1983).

The sum of all reactive nitrogen species in the atmosphere including NO and  $\text{NO}_2$  is defined as  $\text{NO}_y$ . This includes other  $\text{NO}_z$  ( $\text{NO}_z = \text{NO}_y - \text{NO}_x$ ) species including nitric acid ( $\text{HNO}_3$ ), the nitrate radical ( $\text{NO}_3$ ), dinitrogen pentoxide ( $\text{N}_2\text{O}_5$ ), nitrous acid (HONO), peroxyacetylnitrate (PAN), organic nitrates and other secondary nitrogen species. In the nocturnal atmosphere, mixing ratios of  $\text{NO}_3$ ,  $\text{N}_2\text{O}_5$  and HONO are found to maximize.

### **1.3: The Nitrate Radical and Dinitrogen Pentoxide**

The nitrate radical ( $\text{NO}_3$ ) acts as one of the primary oxidants in the nocturnal atmosphere in both marine and terrestrial environments and is expected to be the dominant radical at night (Noxon, 1978, Brown et al., 2007). It plays an important role in the removal of  $\text{NO}_x$  and certain anthropogenic and biogenic VOCs. In particular, reactions with isoprene, terpenes, unsaturated hydrocarbons, cresols and dimethyl sulphide are of significance. A summary of the atmospheric processes which involve  $\text{NO}_3$  and the reservoir species  $\text{N}_2\text{O}_5$  are detailed in figure 1.2:

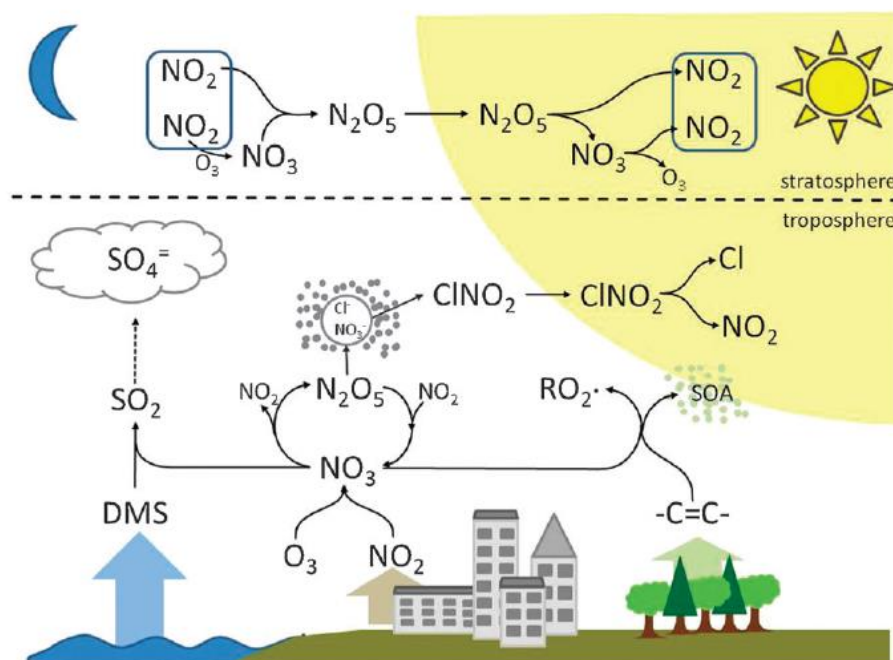


Figure 1.3: Reaction Schematic for Atmospheric Processes Involving  $\text{NO}_3$  and  $\text{N}_2\text{O}_5$  (Brown, S.S. and Stutz, J., 2012)

Mixing ratios of the nitrate radical at night can range from less than 5 ppt in remote areas to as much as 700 ppt during severe pollution episodes in an urban setting (Finlayson-Pitts, 1999, Friedeburg et al., 2002).  $\text{NO}_3$  mixing ratios have also been observed to vary widely over short vertical distances (roughly 10m or less). A field study performed at the Boulder Atmospheric Observatory (BAO) measured  $\text{NO}_3$  vertical profiles through use of a movable carriage situated on a 300m tower (Brown et al. 2007). It was found that mixing ratios were below 5 ppt at ground level, approximately 10-20 ppt in the NBL and 80 ppt in the residual layer (Fig. 1.4). This variability is due to a combination of the nocturnal stratification of the troposphere as well as increased lifetime of the  $\text{NO}_3$  radical with height due to a variation in the distribution of potential sinks for  $\text{NO}_3$  at height, as well as increased levels of  $\text{O}_3$  in the residual

layer. The observed variation can also serve to impact the observed NO<sub>3</sub> chemistry in the early morning, as the warming surface causes the nocturnal inversion layer to be broken.

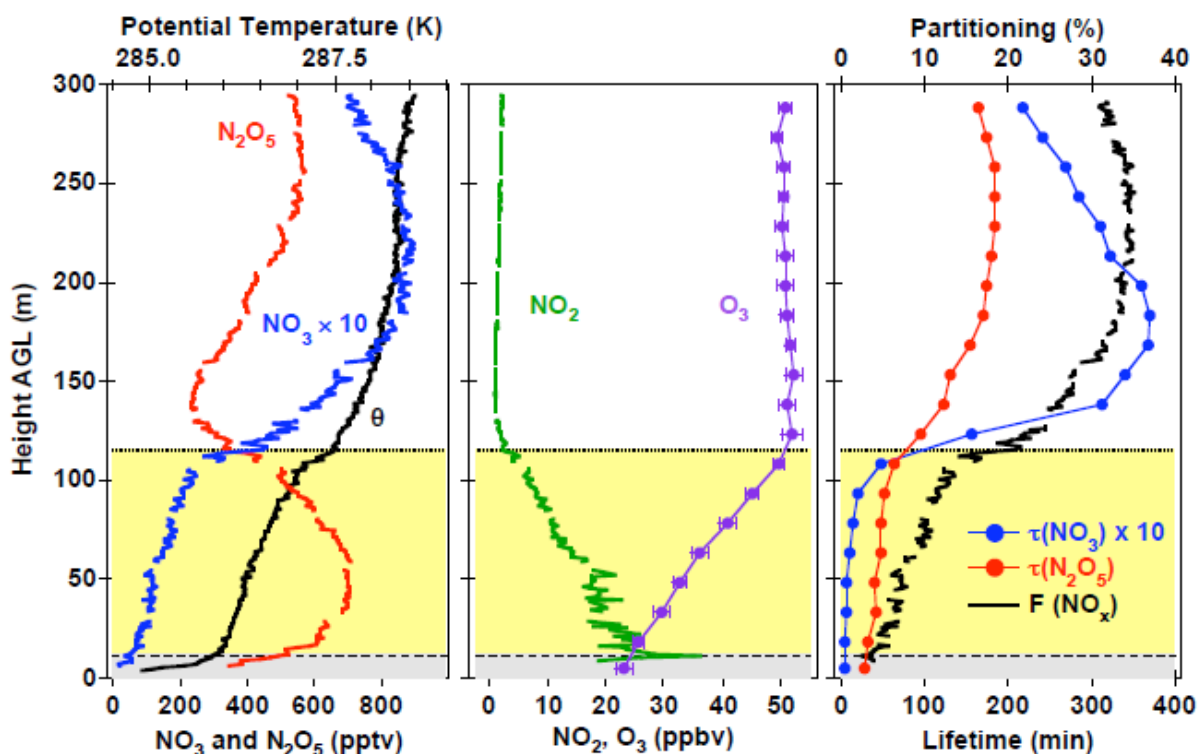


Figure 1.4: Left: Profile of NO<sub>3</sub> and N<sub>2</sub>O<sub>5</sub> and potential temperature as a function of height above ground level (NO<sub>3</sub> mixing ratios multiplied by 10) from 23:15-23:23 on Oct 4<sup>th</sup>, 2004. Center: Vertical profiles of O<sub>3</sub> and NO<sub>2</sub> calculated from measured NO<sub>3</sub>, N<sub>2</sub>O<sub>5</sub> and potential temperature. Right: Profile of calculated NO<sub>3</sub> and N<sub>2</sub>O<sub>5</sub> lifetimes and partitioning. The yellow portion of the graph signifies the nocturnal boundary layer (source: Brown et al. 2007)

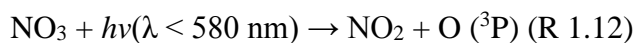
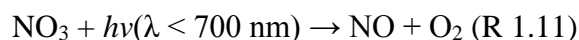
The nitrate radical is formed through the reaction of NO<sub>2</sub> and O<sub>3</sub> (R 1.1), both of which are present in significant concentration in the polluted atmosphere:



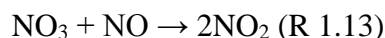
The rate of NO<sub>3</sub> production ( $P_{\text{NO}_3}$ ) can therefore be calculated via NO<sub>2</sub> and O<sub>3</sub> concentration:

$$\frac{d[\text{NO}_3]}{dt} = [\text{NO}_2] \cdot [\text{O}_3] \cdot k_{1.8} \quad (k_{1.8} = 3.2 \cdot 10^{-17} \text{ cm}^3 \text{ molecule}^{-1} \text{ s}^{-1}) \quad (\text{E 1.3})$$

During daylight hours, NO<sub>3</sub> absorbs solar radiation, rapidly undergoing photo-dissociation. Two possible reaction pathways can occur (Brown et al., 2007, McLaren et al., 2011):



Photolysis rates for noontime conditions are within the range of  $j_{1.11} = 0.156\text{s}^{-1}$  and  $j_{1.12} = 0.02 \text{ s}^{-1}$  resulting in a photolysis lifetime of about 5 seconds during the day. Rapid reaction of NO<sub>3</sub> with NO can also act to suppress NO<sub>3</sub> levels in urban environments:



For this reason, the lifetime of NO<sub>3</sub> is shortest when in close proximity to fresh NO<sub>x</sub> production. Using the rate constant of  $k_{(\text{NO}_3 + \text{NO})} = 2.6 \cdot 10^{-11} \text{ cm}^3\text{molec.}^{-1}\text{sec}^{-1}$  (Sanders et al. 2006), the lifetime of NO<sub>3</sub> at surface temperature and pressure is roughly 15 sec in the presence of 0.1 ppb of NO. This reaction is of particular importance during the night, when its rate exceeds that of photolysis.

The reaction of NO<sub>3</sub> with alkenes occurs via the addition of the nitrate radical to a C = C double bond. The resulting reaction forms a nitrate-radical intermediate. Using isoprene as an example (Cantrell et al., 1992):



Further reaction of the intermediate with O<sub>2</sub> leads to the production of a nitroalkylperoxy radical:



Alternatively, the nitroalkyl intermediate can produce an epoxide and NO<sub>2</sub> through reaction 1.16:

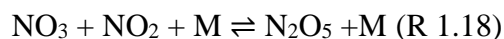


The nitroalkylperoxy radical can then undergo reaction with nitric oxide to form a nitroalkoxy radical or dinitrate, or react with other peroxy radicals, resulting in nitratoperoxides, nitratoalcohols and nitratocarbonyls. The interaction of  $\text{NO}_3$  with isoprene and terpenes can thus be seen to result in a large range of oxidative products, in addition to having a high impact on regional and global aerosol levels. This reactivity of  $\text{NO}_3$  towards VOCs is typically lower than of OH (McLaren et al. 2010). However, on a regional scale,  $\text{NO}_3$  + isoprene chemistry has been found to exceed OH + isoprene chemistry in terms of SOA production, and enhance aerosol production by 30-40% (Brown et al. 2009).

Recent publications have found that  $\text{NO}_3$  chemistry dominates the oxidation of DMS in coastal regions, and can even surpass the contribution from the OH radical over the course of the day (Allen et al. 2000). Thus, nighttime chemistry can be seen to impact the formation of the sulphate aerosol and CCN present in the marine atmosphere. In marine environments,  $\text{NO}_3$  acts as the dominant sink for dimethyl sulphide (DMS), which directly impacts the sulphur cycle in these regions. DMS is released into the atmosphere over the ocean via biological processes of phytoplankton. The nitrate radical acts to oxidize DMS through hydrogen abstraction, producing  $\text{HNO}_3$ :



The formation of  $\text{NO}_3$  is always accompanied by the formation and thermal decomposition of dinitrogen pentoxide ( $\text{N}_2\text{O}_5$ ). The thermal decomposition of  $\text{N}_2\text{O}_5$  is observed to have a strong dependence on temperature. A temperature-dependent equilibrium is established between  $\text{NO}_3$  and  $\text{N}_2\text{O}_5$  via the below reaction:



Under tropospheric conditions, the temperature dependant equilibrium constant can be expressed via the following equation (Osthoff et al. 2007):

$$K_{\text{eq}} = (5.1 \pm 0.8) \cdot 10^{-27} \cdot e^{(10871 \pm 0.46) / T} \quad (\text{E 1.4})$$

Lifetimes of  $\text{N}_2\text{O}_5$  have been observed to be roughly 40 seconds at 290K, increasing to ~700 seconds at temperatures of 270 K. Dinitrogen pentoxide is stable with respect to decomposition in the lower and middle stratosphere, with lifetimes in the range of months and years (Atkinson et al. 2004).

The hydrolysis of  $\text{N}_2\text{O}_5$  to form nitric acid ( $\text{HNO}_3$ ) acts as a major global sink for  $\text{NO}_x$  in the atmosphere (Crutzen and Denter, 1993). This reaction is known to occur on many surfaces. Reaction of  $\text{N}_2\text{O}_5$  with water contained in aerosol and cloud particles acts as the major heterogeneous channel for the reaction:



Homogenous reaction of  $\text{N}_2\text{O}_5$  can also occur with water vapour, but occurs at a considerably slower rate, and is considered a minor channel:

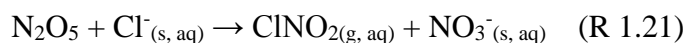


Nitric acid is then removed from the atmosphere through wet and dry deposition.

Accommodation coefficients ( $\gamma$ ) of  $\text{N}_2\text{O}_5$  on the surface of water droplets range between 0.014-0.1 (Hallquist et al. 2003), and  $< 0.0025$  for  $\text{NO}_3$  (Thomas et al. 1993). In addition, modeling studies predict that between 50-90% of  $\text{HNO}_3$  formation occurs by R 1.19 and R 1.20 in the

northern hemisphere, as well the adsorption of  $\text{NO}_3$  on wet surfaces (Dentener and Crutzen, 1993).

The uptake of  $\text{N}_2\text{O}_5$  on chloride containing aerosol can also act as a nocturnal reservoir of  $\text{NO}_x$ , as well a source of reactive Cl atoms the following morning. This reaction was initially believed only to be significant in the marine environment, through the heterogeneous reaction of sea salt aerosols formed through wind-induced bubble bursting at the ocean surface with  $\text{N}_2\text{O}_5$ :



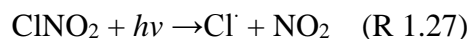
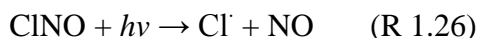
$\text{ClNO}_2$  was first observed in ambient air in Houston (Osthoff, 2008), and was found to be correlated with the loss rate of  $\text{N}_2\text{O}_5$ . From the 2010 CalNex study along the coast of California, nighttime maximum values exceeding 3.0 ppbv of  $\text{ClNO}_2$  were reported (Young et al., 2012, Riedel et al., 2014). The resulting Cl radical is observed to reach a daytime maximum of  $\sim 1 \cdot 10^5 \text{ atoms} \cdot \text{cm}^{-3}$  at 7:00 am, and reacts with VOCs to produce 2.2 times more organic peroxy radicals than in the absence of  $\text{ClNO}_2$  (Riedel et al., 2014). Furthermore, recent work suggests a significant fraction of tropospheric chlorine atoms many arise from anthropogenic sources (Thorton et al., 2010, Mielke et al., 2011). These sources include biomass burning, emission from cooling towers, coal combustion, and the use of road salt in the winter. Reactive chlorine atoms are observed to rainout of the atmosphere in the form of HCl, resulting in some surface deposition. It has been found that both  $\text{NO}_2$  and  $\text{N}_2\text{O}_5$  can react heterogeneously with HCl on solid substrates to produce ClNO and  $\text{ClNO}_2$  (Raff et al. 2009). These reactions are initiated by the uptake of  $\text{NO}_2$  and  $\text{N}_2\text{O}_5$  on the aerosol surface, resulting in the auto-ionization of both species:



The ionized species can then react with HCl:



These reactions were found to be enhanced in the presence of water via catalysis, and could thus have a significant contribution to Cl radical production in coastal urban areas. Accumulated ClNO and ClNO<sub>2</sub> undergo photolysis in the early morning:



The resulting chlorine radical then acts to enhance O<sub>3</sub> production in marine and non-marine regions (Osthoff et al., 2008, Mielke et al., 2011). However, it should be noted that ClNO has not yet been measured in the real atmosphere.

The first recorded measurement of the nitrate radical present in the atmosphere was performed in 1978 by Noxon et al. through absorption of light in the visible region (662 nm), using the moon as an ambient light source. Since then multiple measurements of NO<sub>3</sub> column densities have been performed in both urban and rural ground based sites employing DOAS. As has been established previously, vertical information regarding NO<sub>3</sub> and N<sub>2</sub>O<sub>5</sub> is highly important, given that they are predominantly present at night, when the boundary layer is shallow and little mixing occurs. Passive DOAS measurement of NO<sub>3</sub> SCDs over the course of the night

using moonlight can act to provide information on total vertical resolutions. These measurements can be performed through use ground based instruments (Aliwell et al. 1993, Wagner et al, 2000, Chen et al, 2011), or at height through use of balloons (Renard et al. 2001).

## 1.4: Nitrous Acid

Since it was first detected through use of differential optical absorption in a moderately polluted atmosphere (Perner and Platt, 1979), nitrous acid (HONO) has been identified as a key atmospheric species due to its role as a direct source of hydroxyl (OH) radicals during the day. This is achieved through the photolysis of HONO accumulated over the course the night at sunrise, producing both OH and NO:



Recent field and modeling studies have shown the photolysis of HONO contributes significantly to the OH-radical budget not only in the early morning but during the daytime as well. During the MEGAPOLI summer and winter field campaign downwind of Paris (Michoud et al. 2014), HONO mixing ratios ranging from 0.1-200ppt were observed during the summer campaign. Values were found to be higher during the winter campaign, with averaged daytime values ranging from 400-500 ppt, but potentially as high as 1.7 ppb. Additionally, daytime HONO mixing ratios between 0.5 – 1.0 ppb were reported at a non-urban site in China (Su et al. 2008). This underestimation of the contribution of HONO was mainly due to an incomplete understanding of the formation and sink processes of this trace gas in the troposphere during daylight hours, as well as a lack of ambient measurements. The observed increase in daytime HONO mixing ratios during the winter months could indicate that this missing source is

photolytic in nature, but a greater body of data will be need to prove this conclusively. Shortly after sunset, HONO is observed to increase up to several hundred ppt in rural areas, to several ppb in polluted urban environments. Median nighttime HONO levels at York University, for instance, have been found to be 1.0 ppb during atmospherically stable nights (Wojital 2013).

While photolysis of HONO was previously estimated to contribute 17-34% of the total OH production in polluted environments (Alicke et al. 2003), more recent work using a global chemistry-climate model simulating realistic HONO levels found HONO mixing ratios an order of magnitude higher than previously determined reference values (Elshorbany et al. 2012). Contributions to OH radical production by HONO up to 60 % have been reported in the literature (Spataro et al. 2014). HONO mixing ratios have been seen to show a vertical gradient, due to the most prominent HONO sources both during the day and being found close to the ground. Thus, the contribution of HONO to OH-radical production has been found to be higher in the lower boundary layer (Young et al. 2012). However, significant HONO mixing ratios (both day and night) have also been reported in the residual layer from zeppelin measurements in the troposphere, which were theorized to be caused by a reaction of NO<sub>2</sub> with a HO<sub>2</sub>·H<sub>2</sub>O complex (Li et al. 2014). These results indicate that all sources of HONO are not yet fully understood, and that there may be some overestimation in impact of HONO upon the abundance of OH in the troposphere. Overall HONO formation can be expressed via the following equation:

$$\frac{d\text{HONO}}{dt} = \left( \sum_i P_{i,\text{known}} + P_{\text{unknown}} \right) - (L_{\text{photo}} + L_{\text{HONO}} + L_{\text{OH}} + L_{\text{dep}}) + (T_v + T_h) \quad (\text{E 1.5})$$

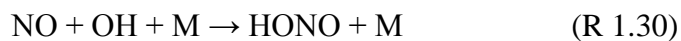
The missing daytime HONO sources are represented by the term  $P_{\text{unknown}}$ , while  $L_{\text{photo}}$  represents HONO photolysis. A small percentage of HONO is also expected to be destroyed by OH radicals:



Dry deposition of HONO is represented by  $L_{\text{dep}}$ . Vertical ( $T_v$ ) and horizontal ( $T_h$ ) transport processes can act as a source or a sink of HONO depending on the concentration in advected air in comparison to the concentration of the measurement site. For ground based HONO sources, vertical transport would act to dilute HONO concentration near the ground, and thus would act as sink. Under typical conditions, photolysis is assumed to be the major daytime sink, and reaction R 1.28 and R 1.29 result in the daytime HONO lifetime being roughly 10-20 minutes.

Several HONO formation pathways have been proposed. HONO can be directly emitted into the troposphere by combustion processes, vehicular exhaust, and industrial processes. Measurements of HONO,  $\text{NO}_2$ , NO, and  $\text{CO}_2$  within the Wuppertal Kiesbergtunnel in Germany found that direct HONO emission was more important than heterogeneous  $\text{NO}_2$  into HONO conversion on the surface of the tunnel wall during times of high traffic density (Kurtenbach et al. 2001). In contrast, during low traffic density, HONO mixing ratios were dominated by heterogeneous conversion of  $\text{NO}_2$ , and the overall traffic tunnel study overall found that only 0.3-0.8 % of  $\text{NO}_x$  could be attributed to direct HONO emission, dependent upon the type of fuel undergoing combustion. This serves to indicate that direct emission can significantly contribute to the formation of HONO in the troposphere only in area with high  $\text{NO}_x$  sources.

The reaction of the OH radical and NO is known to produce HONO through the following reaction:



Due to high levels of OH-radicals and anthropogenic NO present in urban areas, this reaction can act as significant HONO source in this setting. During daylight hours, homogenous HONO formation is assumed to reach an instantaneous photo-stationary state (PSS) with the photolysis of HONO (R 1.28). Using the photo stationary state approach, the HONO concentration ( $[HONO]_{PSS}$ ) can be determined through the following equation:

$$[HONO]_{PSS} = \frac{k_{(NO+OH)} \cdot [OH][NO]}{j_{HONO} + k_{(HONO+OH)}[OH]} \quad (E 1.6)$$

The photolysis frequency of HONO is represented by  $J_{HONO}$ , while  $k_{(NO+OH)}$  ( $9.8 \cdot 10^{-12} \text{ cm}^3 \cdot \text{molecule}^{-1} \cdot \text{sec}^{-1}$ ) and  $k_{(HONO+OH)}$  ( $6.0 \cdot 10^{-12} \text{ cm}^3 \cdot \text{molecule}^{-1} \cdot \text{sec}^{-1}$ ) represent R 1.29 and R 1.30 respectively at 298 K and 1010 hPa of pressure (Atkinson et al., 2004). However, field experiments have reported daytime HONO mixing ratios in urban and rural areas to be substantially higher than the calculated value of  $[HONO]_{PSS}$ . Thus, homogenous HONO production alone is insufficient to explain observed HONO mixing ratios.

The currently accepted HONO formation pathway, at least at night, involves the heterogeneous conversion of  $NO_2$  on humid surfaces. Laboratory studies have suggested the following reaction takes place with surface adsorbed water to convert  $NO_2$  into HONO and  $HNO_3$  (Finlayson-Pitts et al., 2003):



The reaction proceeds through the formation of a dimer of  $NO_2$  ( $N_2O_4$ ) on the surface film. The resulting dimer can undergo isomerization to form  $ONONO_2$ , which can then auto-ionize to form  $NO^+NO_3^-$ .  $NO^+NO_3^-$  can then react with water acts to form both HONO and  $HNO_3$ . Thus, reaction R1.31 becomes:



HONO can then diffuse from the surface to the gas phase, leaving HNO<sub>3</sub> behind on the surface.

It is worth noting that the ionization of ONONO<sub>2</sub> is in competition with the back reaction gas phase NO<sub>2</sub> to reform symmetric N<sub>2</sub>O<sub>4</sub>. The complete reaction mechanism is shown in figure 1.4 (Finlayson-Pitts 2003):

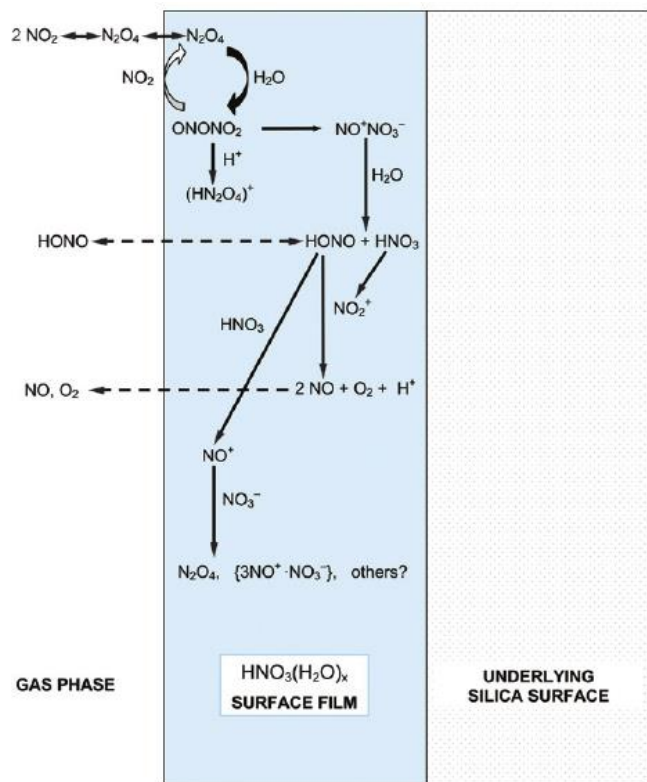


Figure 1.5: Diagram of Heterogeneous Hydrolysis of NO<sub>2</sub> (Source: Finlayson-Pitts 2003)

The overall rate of HONO formation is observed to be first order with respect to NO<sub>2</sub>, + 2 from the formation of N<sub>2</sub>O<sub>4</sub>, and -1 from back reaction with NO<sub>2</sub> with the ONONO<sub>2</sub> complex to reform the NO<sub>2</sub> dimer.

Currently, there is a great deal of research being devoted to determining the unknown daytime source of HONO that has been found through experimental observations (Su et al. 2008, Michoud et al. 2014). Li et al. (2008) proposed the reaction between electronically excited NO<sub>2</sub>

( $\lambda > 420$  nm) and water vapor as a major daytime HONO formation pathway. While most of the excited  $\text{NO}_2$  will collide with unreactive molecules present in the troposphere (M), relaxing to a lower energy state, water is a sufficiently abundant atmospheric constituent that some  $\text{NO}_2^*$  could react to produce HONO and OH:



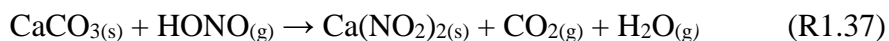
This process was later determined to be a two photon process (Amedro et al. 2011), indicating that it is not an important source of daytime HONO. The reduction of  $\text{NO}_2$  to HONO on various organic or inorganic photolytic substrates has also been proposed as a daytime HONO source. For example, the partitioning of soil nitrite ions through conversion of ammonium ( $\text{NH}_4^+$ ) to ( $\text{NO}_2^-$ ) by nitrifying microbes could act as a possible source for both HONO and OH:



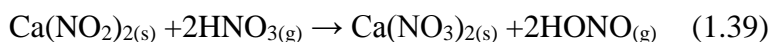
The  $\text{NO}_2^-$  produced as a result is only present in the aqueous phase and can undergo a reversible acid-base reaction to form  $\text{HONO}_{(\text{aq})}$ :



The resulting HONO can then partition reversibly from the aqueous phase into the gas phase in humid soil. Additionally, HONO is sufficiently acidic ( $\text{pK}_a = 3.29$ ) to react with carbonate salts in dust to form nitrite salts (Vandenboer et al. 2014):



The resulting nitrite can then undergo acid displacement to generate HONO:



In this way, this acid displacement mechanism could act as nighttime HONO reservoir and daytime HONO source. These processes could explain high daytime HONO values when coupled

with lack of near surface irradiance due to dense vegetation and high NO<sub>2</sub> mixing ratios. Further field measurement of NO<sub>2</sub>, NO, and HONO mixing ratios within the lower troposphere will be needed to characterize day and nighttime HONO processes, and to improve modeled HONO mixing ratios.

## 1.5: Differential Optical Absorption Spectroscopy

The use of absorption spectroscopy has been well established in the analysis of the chemical composition of gases. Differential optical absorption spectroscopy (DOAS) makes use of this concept to quantify the mixing ratios of trace gases based on the attenuation of light intensity as it passes through the open atmosphere. It was through this technique that the OH radical was first detected within the atmosphere, and thus increased understanding of HO<sub>x</sub> and ozone chemistry (Perner et al. 1976). This highlights one of the key advantages of DOAS; the non-invasive nature of the technique is useful in detecting highly reactive trace gases and radical species. The operation of DOAS is based upon the Beer Lambert law (Finlayson-Pitts, B. J. and Pitts Jr, 1999):

$$I(\lambda) = I_o(\lambda)e^{-\sigma(\lambda)Lc} \quad (\text{E 1.7})$$

where  $I_o(\lambda)$  is the initial intensity of a given light beam, and  $I(\lambda)$  is the radiation intensity of the beam after passing a layer of atmospheric absorbers of thickness  $L$  (cm) with analyte concentration  $c$  (molecules cm<sup>-3</sup>) and absorption cross section  $\sigma(\lambda)$ . Once these quantities are known, the average trace gas concentration can be determined by rearrangement of E 1.7:

$$c = \frac{\ln\left(\frac{I_o(\lambda)}{I(\lambda)}\right)}{\sigma(\lambda) \cdot L} = \frac{D}{\sigma(\lambda) \cdot L} \quad (\text{E 1.8})$$

The ratio of  $\ln(I_o(\lambda)/I(\lambda))$  is also known as the optical density (D) of a layer of a given atmospheric absorber:

$$D = \ln\left(\frac{I_o(\lambda)}{I(\lambda)}\right) = \sigma(\lambda)cL \quad (\text{E 1.9})$$

Light traveling through the open atmosphere encounters more than specific trace gases, however. As light travels through a given air parcel, scattering can occur, through interaction of photons with air molecules (Rayleigh scattering), and atmospheric aerosol (Mie scattering). Intensity can also be reduced through the transmissivity of the instrument (mirror and retroreflectors). Expansion of the Beer Lambert Law is therefore necessary to include atmospheric scattering. This is accomplished through the introduction of the Raleigh extinction coefficient  $\epsilon_R(\lambda)$  and Mie extinction coefficient  $\epsilon_M(\lambda)$ , which is defined as follows:

$$\epsilon_R(\lambda) \approx \sigma_{RO}(\lambda) \cdot \lambda^{-4} \cdot c_{\text{Air}} \quad (\text{E 1.10})$$

$$\epsilon_M(\lambda) = \epsilon_{MO} \lambda^{-n} \cdot N_A \quad (\text{E 1.11})$$

The Beer Lambert law then becomes:

$$I(\lambda) = I_o(\lambda)e^{-L(\sum(\sigma_j(\lambda)c_j) + \epsilon_R(\lambda) + \epsilon_M(\lambda))} \cdot A(\lambda) \quad (\text{E 1.12})$$

Instrumental effects and turbulence are summarized in the term  $A(\lambda)$ , and the absorption cross section is extended to a summation of all trace gas absorbers, j, in the atmosphere. The determination of a given trace gas concentration would in principle require the quantification of all factors influencing the transmitted intensity. This difficult task can be overcome through the measurement of the *differential absorption*, which is defined as the component of the total absorption of a given atmospheric molecule that varies rapidly as a function of wavelength (Platt

and Stutz, 2008). Aerosol extinction processes, turbulence effects, and many trace gas absorptions show very broad smooth spectral characteristics. Certain trace gas species, however, exhibit narrowband absorption structures (< 10nm). Thus, the separation of broad and narrowband structures in absorption spectra allows the isolation of these narrow trace absorptions, which serve as fingerprint bands for a given trace gas species. This separation is best represented by:

$$\sigma_j(\lambda) = \sigma_{j,o}(\lambda) + \sigma'_{j}(\lambda) \quad (\text{E 1.13})$$

where  $\sigma_{j,o}(\lambda)$  is the broadband component and  $\sigma'_{j}(\lambda)$  is the narrowband component. Applying this separation to equation E 1.12 yields:

$$I(\lambda) = I_o(\lambda)e^{-L(\Sigma(\sigma'_{j}(\lambda)c_j))} \cdot e^{(\Sigma(\sigma_{j,o}(\lambda)c_j) + \epsilon_R(\lambda) + \epsilon_M(\lambda))} \cdot A(\lambda) \quad (\text{E 1.14})$$

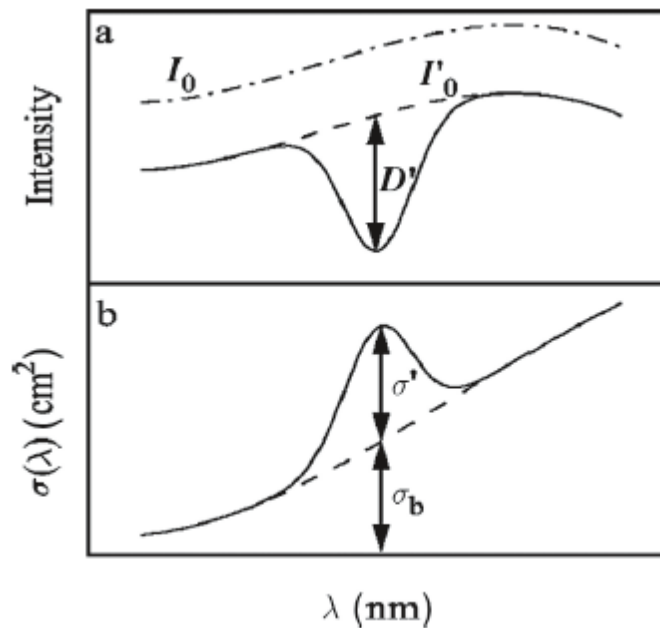


Figure 1.6: Principle of DOAS:  $I_0$  and  $\sigma$  are separated by an adequate filtering procedure into a narrow ( $D'$ , and  $\sigma'$ ) and broad ( $I'_0$  and  $\sigma_b$ ) component (Platt and Stutz 2008)

The first exponential now represents the effect of the structured differential absorption of the trace species, while the second represents the slowly varying absorptions, scattering effects and turbulence. The differential cross-section  $\sigma'_j(\lambda)$  can then be substituted into equation E 1.8 and E 1.9. Differential cross sections are determined in the laboratory, and are typically represented in the form of cross section reference spectra that are available for analysed chemical species.

Substitution of  $\sigma'_j(\lambda)$  into E 1.9 yields a differential optical density  $D'$ :

$$D' = \ln\left(\frac{I_o(\lambda)}{I(\lambda)}\right) = L\Sigma(\sigma'_j(\lambda)c_j) \quad (\text{E 1.15})$$

Rearrangement of the above equation yields the concentration of trace absorber j:

$$c = \frac{D'(\lambda)}{\sigma'_j(\lambda) \cdot L} \quad (\text{E 1.16})$$

A key advantage of the DOAS technique is that it allows simultaneous measurement of multiple trace gases from a single ambient spectrum, provided that cross section reference spectra are available. Calibration is likewise not necessary, provided that the absorption cross section is accurately known, as DOAS is an absolute measurement technique. DOAS can be performed with both an active and passive source of illumination. In the case of active measurement, an active light source is coupled with the optical set-up of the DOAS apparatus to send and receive light into the atmosphere. This set-up typically requires a method of folding the light beam at one end of the light path, such as through use of a retro-reflector. Spectroscopic detection is then performed upon this return signal by a spectrometer. Due to low mixing ratios of trace gases present in the troposphere, the path length required for active DOAS is fairly large (several km). The technique is usually employed in order to determine the composition of atmospheric species

in the troposphere, and thus often have light paths which are parallel to the ground. Active DOAS also finds use in simulated environments in the form of smog and aerosol chambers.

Passive DOAS makes use of light from natural source, most commonly the sun and moon. In the case of the sun, this method of measurement can be further subdivided into direct solar measurements, lunar DOAS (solar light reflected off the moon) and measurement of sky scattered sunlight using MAX-DOAS (Halla et al., 2013). Passive DOAS has the advantage of a relatively simple experimental set-up in comparison to active DOAS. However, due to the technique's dependence on natural light sources, there is an additional meteorological requirement (typically lack of clouds) in order to obtain useful data. This is especially true with lunar DOAS, as the full moon is necessary for the maximum illumination, yet is only present in the sky for a few days per month. Additionally, since the light path of passive DOAS crosses the entire vertical extent of the atmosphere, direct conversion of column densities to trace gas concentration requires extensive radiative transfer modelling. The column density, defined as trace gas concentration integrated along the effective light path, is instead determined as the direct results of these measurements:

$$SCD = \int_0^{\infty} c(s)ds \quad (E1.17)$$

This results in the determination of slant column density (SCD) of a given species of interest at a given elevation angle. Due to the dependence of the SCD upon both the elevation angle of the instrument of measurement (usually a telescope), as well as the light source (sun or moon), it is necessary to convert slant column densities into vertical column densities (VCD) which is independent of these parameters, where  $z$  is the vertical distance from the surface:

$$VCD = \int_0^{\infty} c(z) dz \text{ (E1.18)}$$

Thus, the use of active and passive DOAS have advantages and limitations to the scope of their application. Use of both techniques simultaneously, which occurs in this work, allows the determination of the vertical distribution of an atmospheric species of interest. Comparison of this vertical distribution to literature sources then provides valuable insight into chemical composition and structure of the nighttime atmosphere. The exact techniques utilized in both studies presented will be detailed in chapter 2.

# Chapter 2: Experimental

## 2.1: Active DOAS Analysis

### 2.1.1: Instrumental Set-up of Active DOAS

Both day and night-time active DOAS measurements of NO<sub>2</sub>, SO<sub>2</sub> and HONO were performed using a modified DOAS 2000 instrument set up at the primary analysis site (AMS13, see section 2.1.7). The instrument (Fig 2.1) is composed of a coaxial Cassegrain telescope with transmitting and receiving optics combined within the instrument. A 150 W high pressure Xenon lamp (Hamamatsu L2274) sits in the focal plane of the 8” primary mirror of the telescope. The outgoing beam is collimated on the outer edges of the primary mirror, and travels through the open atmosphere to the retro-reflector. A 30 corner cube retroreflector was set up at the end of a cleared forest path (Lat: 57.139°N, Long: 111.642°W), atop a 5.2 meter tower. The tower was positioned 1.152 km due south of instrument site, yielding a total path length of 2.304 km. Given the height of the telescope (roughly 1.5m), the resulting average height of the light beam was found to be 3.7 m above the surface. The return beam is focused by the inner portion of the primary mirror onto a 600 μm fibre optic cable and subsequently transmitted to the spectrometer optimized for the species of interest. Return spectra were collected with the USB2000 spectrometer (Grating #10, 2048 element CCD, 25μm slit) in the UV-visible region (287.8-492.1 nm) using Spectrasuite software, allowing determination of HONO, NO<sub>2</sub>, and SO<sub>2</sub>. Data was collected at 2 minute intervals from Aug 17<sup>th</sup>-Sept 11<sup>th</sup>. ). Instances of fog were observed to interfere with the light path, thus resulting in low light return levels. These periods have been removed from the dataset.

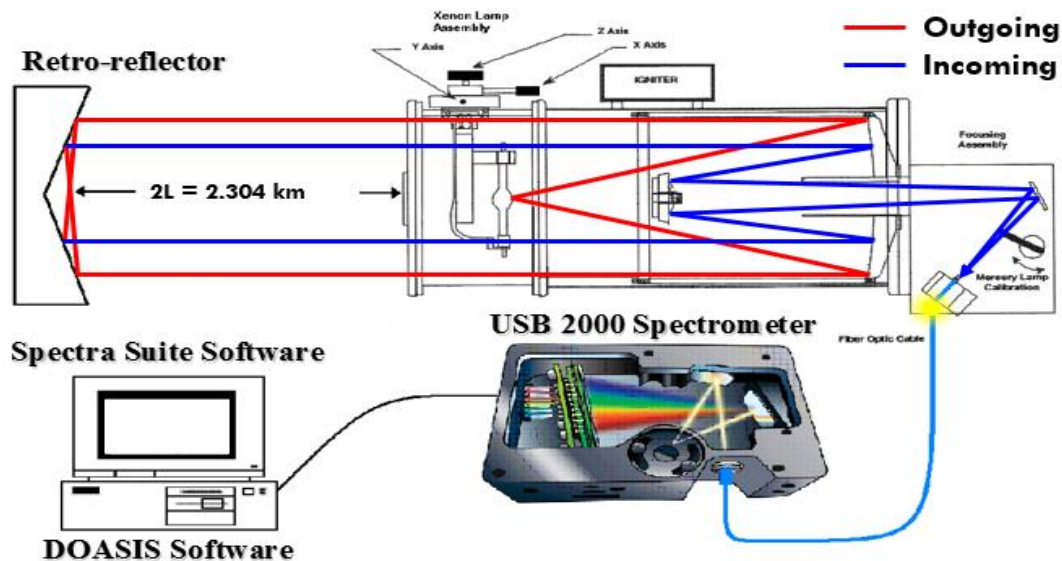


Figure 2.1: Active DOAS apparatus used at AMS13

### 2.1.2: Spectral Analysis Software

Measured ambient spectra were corrected and analysed using DOASIS software (Kraus, 2006). The software makes use of a Levenburg-Marquardt algorithm, which can be used to numerically solve non-linear systems (Levenburg et al. 1944). This is useful in the case of DOAS, since spectral alignment cannot be solved through use of linear least squares fitting techniques (Platt and Stutz, 2008). Thus, this method consists of a least squares fit where a linear component is used for retrieval of the trace gas absorption, while a non-linear component accounts for spectral shifts between the measured spectra and the chosen reference spectra. In this way, the non-linear component acts to minimize the residual noise left over after fitting the ambient spectra. The algorithm uses an iterative approach to converge upon the best estimate of the modelled parameters until the optimum solution is determined.

In order to fit a spectrum, DOASIS requires a predetermined fit scenario. This consists of a lamp spectrum, along with reference absorption spectra for all species present with significant

absorption features in the wavelength range of the spectrometer. The shift and squeeze exerted upon the measured spectrum is also controlled by the prepared fitting scenario. Upon application of the algorithm, the software computes a column density and fit error of each trace gas within the selected fit scenario. The fit residual, and chi squared value for the overall fit is computed as well. For active DOAS analysis, the trace gas concentration can then be computed from the known path length and number density of the air at a specific temperature and pressure. However, before fitting can be performed, measured spectra must be corrected, and reference spectra and wavelength calibrated. Likewise reference spectra must be convoluted in order to match the resolution of the spectrometer.

### **2.1.3: Electronic Offset, Dark Current and Calibration Spectra**

*An offset spectra* contains the baseline signal produced by the CCD detector over the course of data sampling and depends upon the electronics of the detector. This baseline subtraction is necessary in order to ensure that the observed signal intensity is attributed to the light projected and received by the DOAS telescope. Offset corrections are applied to each ambient spectra and lamp spectra through the subtraction of the offset spectra prior to the fit procedure. In the case of this field study data, offset spectra were collected by using a small integration time (to minimize effects of dark current) and a large number of averages (3ms, 10000 averages). Due to a negative dependence of the electronic offset with temperature, it must be collected at the same temperature as the ambient spectra. Figure 2.2 provides an example of an offset spectra taken on the 20<sup>th</sup> of August:

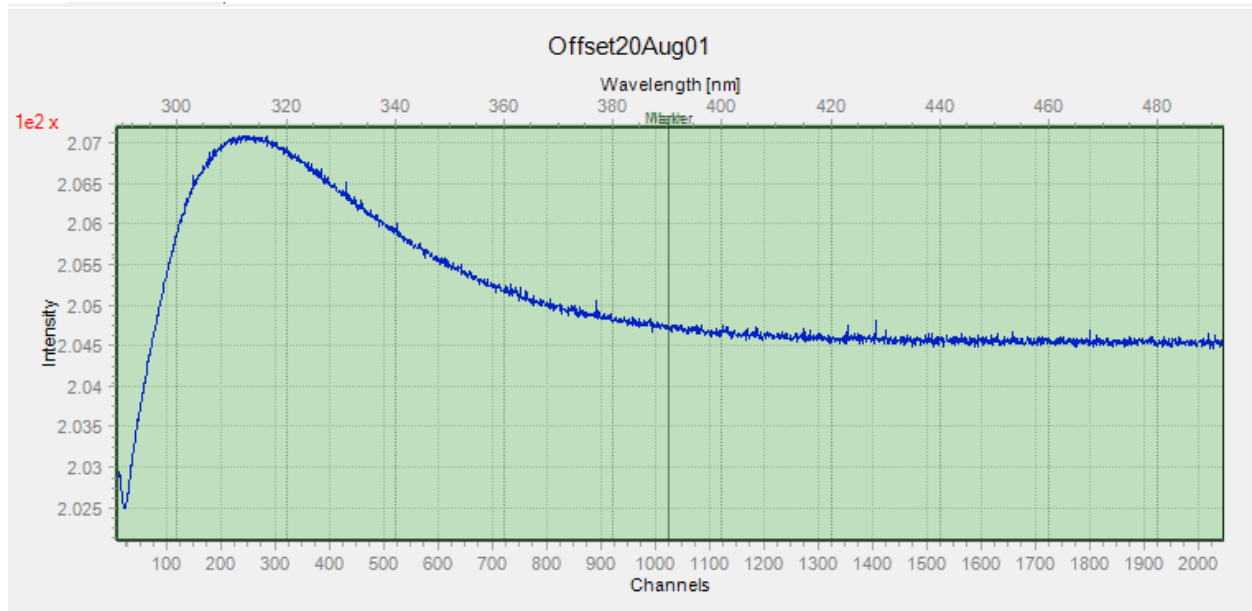


Figure 2.2: Sample offset spectra collected Aug 20<sup>th</sup> 2013 using the USB2000 spectrometer with integration time of 3 ms, 10,000 averages, and temperature control stabilized at 17°C

A *Dark Current spectra* is the signal obtained by the detector in the absence of light. It is the result of statistical variation in the number of thermally generated electron-hole pairs generated within the silicon structure of the CCD detector of the spectrometer caused by thermal noise. The resulting pixel to pixel variation shows positive correlation with temperature, with the exception of some “hot pixels” that display distinctly non-linear behavior. The correction of the lamp spectrum and ambient spectra for dark signal is achieved through the subtraction of a measured dark current spectrum taken at the same temperature. Unlike the electronic offset, dark current does increase with exposure time, since it is a continuous production of electron-hole pairs. Longer integration time therefore results in a linearly higher number of electrons generated by dark current. The dark current spectra collected during the field study purposefully had much longer integration times than the other collected spectra (20-25 sec, 5 averages). Before subtraction, the integration time of the dark current is adjusted to match the integration time of

spectra being dark noise corrected. An example of a corrected dark current spectrum used for correction of sample spectra is shown below in figure 2.3:

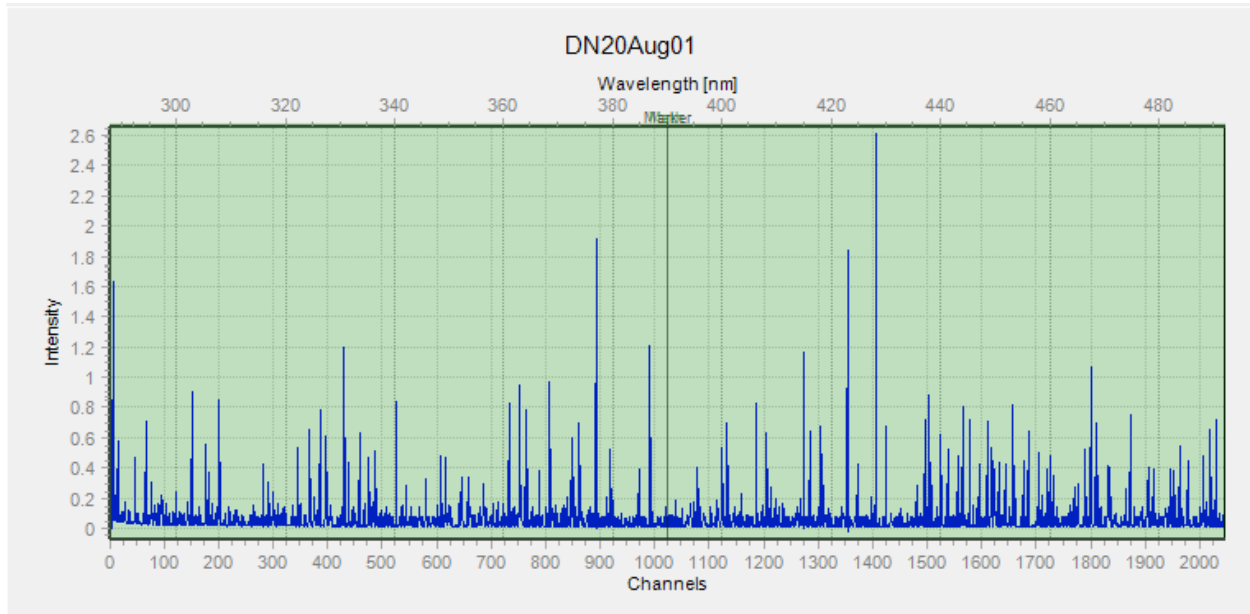


Figure 2.3: Sample dark current spectra collected Aug 20<sup>th</sup> 2013 using USB 2000 spectrometer with int. time 20 sec, 5 averages, and temperature stabilized at 17°C. Spectrum has been corrected for electronic offset and adjusted for correction of sample spectra

Wavelength calibration of the experimental data is accomplished through use of a *mercury lamp* spectrum. It was collected through the direction of light from a mercury lamp into the fibre optic cable while blocking all other incoming light sources. In the case of this experimental set-up, this was achieved mechanically; the position of the lamp was controlled by a switch, and moved to cover the fibre optic cable when calibration spectra needed to be taken. Total exposure time varied between 20-50 seconds (int. time 40-100 ms, 400-1000 averages), due to adjustment of the fibre optic cable over the course of the study. Wavelength calibration of sample spectra was performed using the published values of mercury lines present at 296.73nm,

302.15nm, 313.17nm, 334.15nm, 365.02nm, 404.66nm and 435.84nm. Each peak was fit with a Gauss function, the center of which was utilized for calibration. The mercury lamp calibration function was then determined through the application of a 3<sup>rd</sup> order polynomial applied to the wavelength vs pixel element number. Input of the calibration values into the automated sample script allowed all sample spectra to be wavelength calibrated.

Due to the higher resolution of the reference absorption spectrum compared to those of the spectrometer, reference spectra are convoluted in order to match the resolution of the spectrometer. The resolution of the spectrometer can be determined through the full width half maximum (FWHM) of emission lines of the mercury spectrum near the wavelength range used for fitting of sample spectra. In the case of the determination of HONO, the mercury line present at 334.15nm was chosen for calibration of the reference spectra. Based on the FWHM of this emission line, the resolution of the USB2000 spectrometer was found to be ~0.5 nm at 17°C. An example mercury lamp spectrum is shown on Figure 2.4:

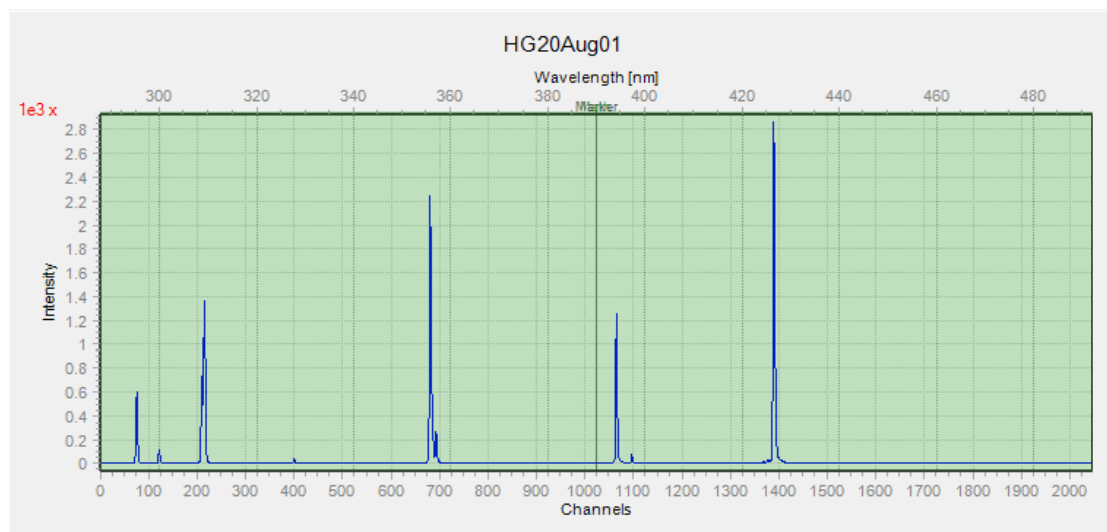


Figure 2.4: Sample Hg lamp spectra taken Aug 20<sup>th</sup> using USB 2000 spectrometer with int. time 50 msec, 400 averages, and temperature stabilized at 17°C. Corrected for offset and dark current.

### 2.1.4: Xe Lamp Spectra

The active lamp of the DOAS instrument is a 150 W high pressure Xe lamp. A small light arc develops in the centre of the quartz bulb due a high voltage applied between the anode and cathode (see fig. 2.5) which acts to ionize the Xe gas. Due to the high temperature of the arc (T= 6000-10000 K) Xe arc-lamps are found to be much brighter than incandescent lamps, as well as exhibiting a smooth spectrum in spectral range of interest. This includes the UV region, which allows measurement of both O<sub>3</sub> and SO<sub>2</sub>.

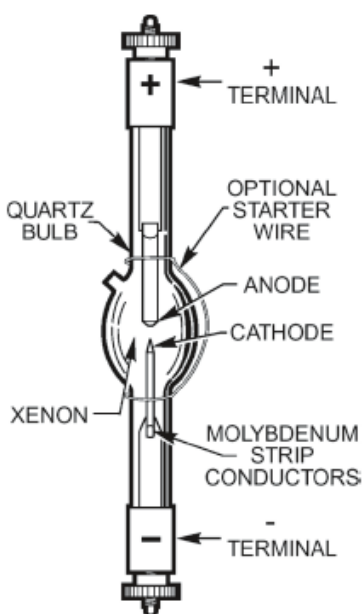


Figure 2.5: High pressure Xe-arc lamp. A small arc develops in the centre of the bulb between the anode and cathode (Platt and Stutz 2008)

Xe-lamp spectra were collected at several points throughout the study. They were collected primarily through adjusting the optics of the DOAS instrument such that a small portion of reflected lamp light was directed into the fibre optic cable without first travelling through the open atmosphere. A summary table of the collected lamp spectra, as well as the integration time and number of averages of each can be found below:

Table 2.1: AMS13 lamp spectra (collected in triplicate)

| Date of Analysis            | Int. Time (ms) | Number of Averages |
|-----------------------------|----------------|--------------------|
| Aug 17 <sup>th</sup> , 2013 | 40             | 6000               |
| Aug 19 <sup>th</sup> , 2013 | 40             | 6000               |
| Aug 20 <sup>th</sup> , 2013 | 25             | 6000               |
| Aug 21 <sup>st</sup> , 2013 | 50             | 6000               |
| Aug 28 <sup>th</sup> , 2013 | 20             | 12000              |
| Sept 5 <sup>th</sup> , 2013 | 30             | 12000              |

### 2.1.5: HONO Fit Scenario

HONO fitting was performed in the 337-361 nm regions of the spectra. Reference spectra for HONO (Bongartz et al. 1994), NO<sub>2</sub> (Vandele et al. 1997), the O<sub>2</sub>-O<sub>2</sub> collision dimer (Burkholder et al. 1990), and a Xe lamp spectra were used, in addition to a 3<sup>rd</sup> order polynomial.

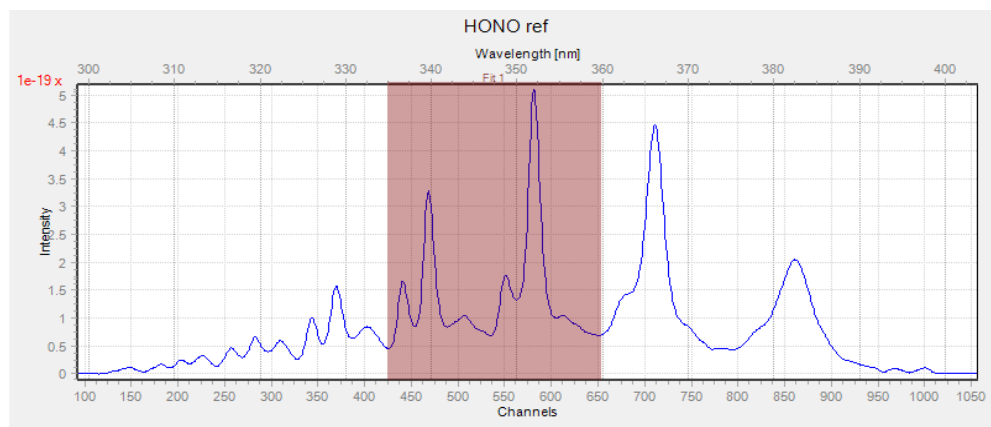


Figure 2.6: HONO cross section convoluted to the USB2000 spectrometer. Fit range (337-361 nm) shown in purple

During daylight hours, a daylight background spectrum was added to the fitting scenario in order to account for solar features. These spectra were collected in triplicate on the 22<sup>nd</sup> of August, 28<sup>th</sup> of August, and September 11<sup>th</sup>. Collection was performed by turning off the Xe

lamp while leaving all other aspects of the DOAS instrument untouched. It was found that the best possible fit in terms of precision (chi-squared) was observed when the background spectrum taken at 1:18 pm on the 22<sup>nd</sup> of August was used. This daylight background spectrum was used in all daytime HONO fitting. Removal of the background spectrum showed significantly negative HONO slant column densities being observed over the course of the day. A high pass binomial filter with 2000 iterations was also applied to the Xe lamp spectra, reference spectra, and sample spectra to further remove broadband features (Denis Poehler, personal communication).

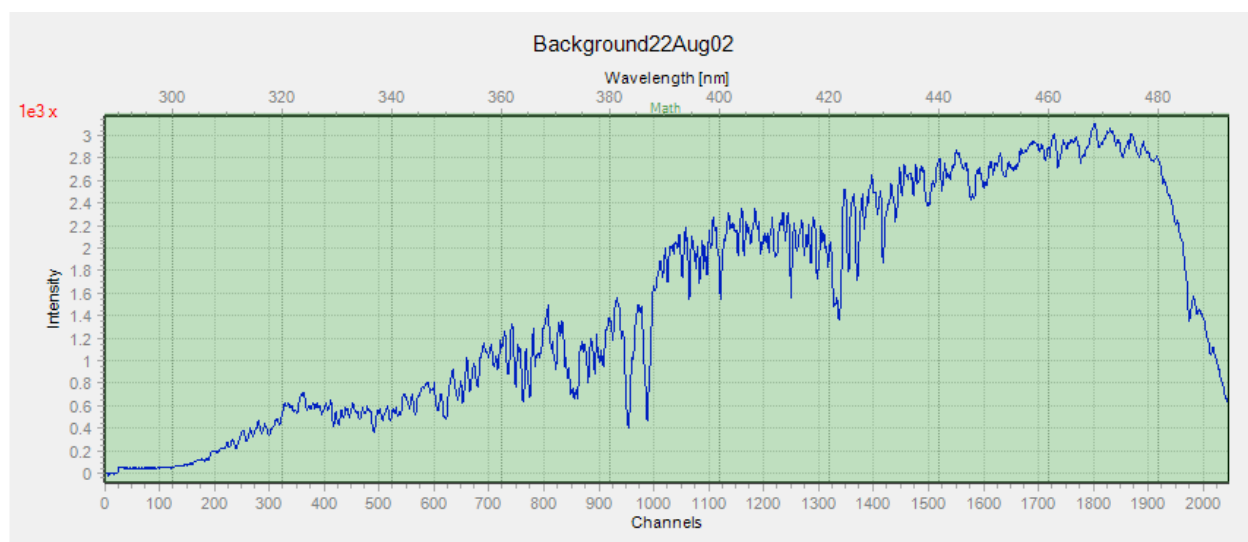


Figure 2.7: Solar background spectra used for daytime HONO fitting. Collected Aug 22<sup>nd</sup> at 1:18 pm

### 2.1.6: Use of Two-Lamp Fit

Initial attempts to fit the entirety of the collected dataset revealed an artifact that resulted in HONO mixing ratios decreasing with time, eventually becoming negative as the study progressed. This served to cast doubt not only on results found later in the study, but reduced confidence in initial results. Our best hypothesis is that something was changing experimentally

over time, as it seemed unlikely that HONO mixing would show such a trend, and in particular the appearance of negative mixing ratios. Experimentation with use of different lamp spectra in the HONO fit scenario found significant variation in the HONO column densities. From these results, it can be inferred that there is drift present in the Xe lamp used over the course of the study. There are many possibilities for the cause of such a drift. A variation in lamp temperature due to continuous running could result in changes in observed features in the region of fitting, which in turn could lead the variation between lamp spectra. Investigation into the structure of the Xe lamp used at AMS13 found that the continuous running of the xenon arc lamp could lead to reduction of luminous flux due to the deposition of evaporated tungsten on the walls of the quartz envelope over time (Zeiss Microscopy Online). It is noted here that the lamp used in this study was brand new and replaced just prior to the beginning of the field study. Despite this, due to continuous running of the lamp throughout the study could act to accelerate wear of the lamp electrodes (condensation of W on the quartz envelope). This would cause premature blackening of the lamp envelope. Lamp blackening acts to reduce output of the light and shifts the spectral characteristics of the output to a lower colour temperature. Thus, blackening of the lamp is one plausible explanation for the features which were found to form in the lamp spectra with time

The observed variation was accounted for through using the closest lamp spectra in time to the date being fit. However, since lamp spectra were only taken on six days throughout the study, there were large gaps of time with no lamp spectra being taken. Thus, sample spectra were fit using two lamp spectra, where the two lamp spectra bracketed the measurement spectra in time. The hope was that a linear combination of the two lamps might better fit the observed lamp spectrum than any individual lamp spectrum. However, this method does not account for periods

before the first lamp spectrum was taken (Aug 17<sup>th</sup>) as well as the period after the last lamp spectrum (Sept 5<sup>th</sup>) was taken. In the interest of maintaining a consistent methodology the final dataset was limited to sample spectra taken from Aug 17<sup>th</sup> and Sept 4<sup>th</sup>, 2013. An example of the two-lamp fit, taken at the point of highest observed HONO concentration over the course of the measured data is displayed in figure 2.8:

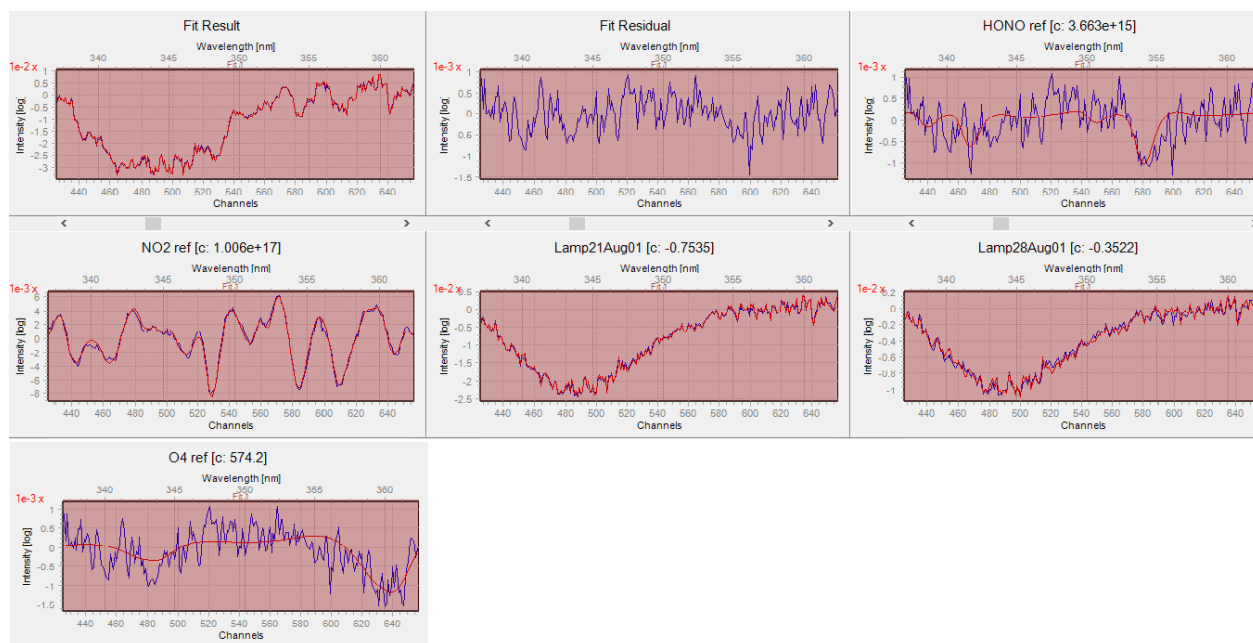


Figure 2.8: DOASIS HONO fit output measured on Aug 21<sup>st</sup> / 2013 at 10:06 pm. The HONO mixing ratio of the fit is  $0.64 \pm 0.07$  ppb

### 2.1.7: AMS13 Site

In the summer of 2013, a number of universities took part in a joint study conducted by Environment Canada to study Oil Sands emissions to the atmosphere. Research was conducted at the AMS13 site operated by Environment Canada, located north of Fort McKay (Lat: 57.149°N, Long: 111.642 °W). The site is located roughly 12 km north of the Syncrude Mildred Lake facility and 20 km northeast of the Suncor Oil Sands processing plants. Ground site measurements were taken in conjunction with 25 research flights using an instrumented research

aircraft, the National research Council Convair 580. Analysis was focused upon  $\text{NO}_y$ ,  $\text{SO}_x$ , VOCs and aerosols related to the extraction and combustion of bitumen. A map of the site and surrounding area is shown in figure 2.9:

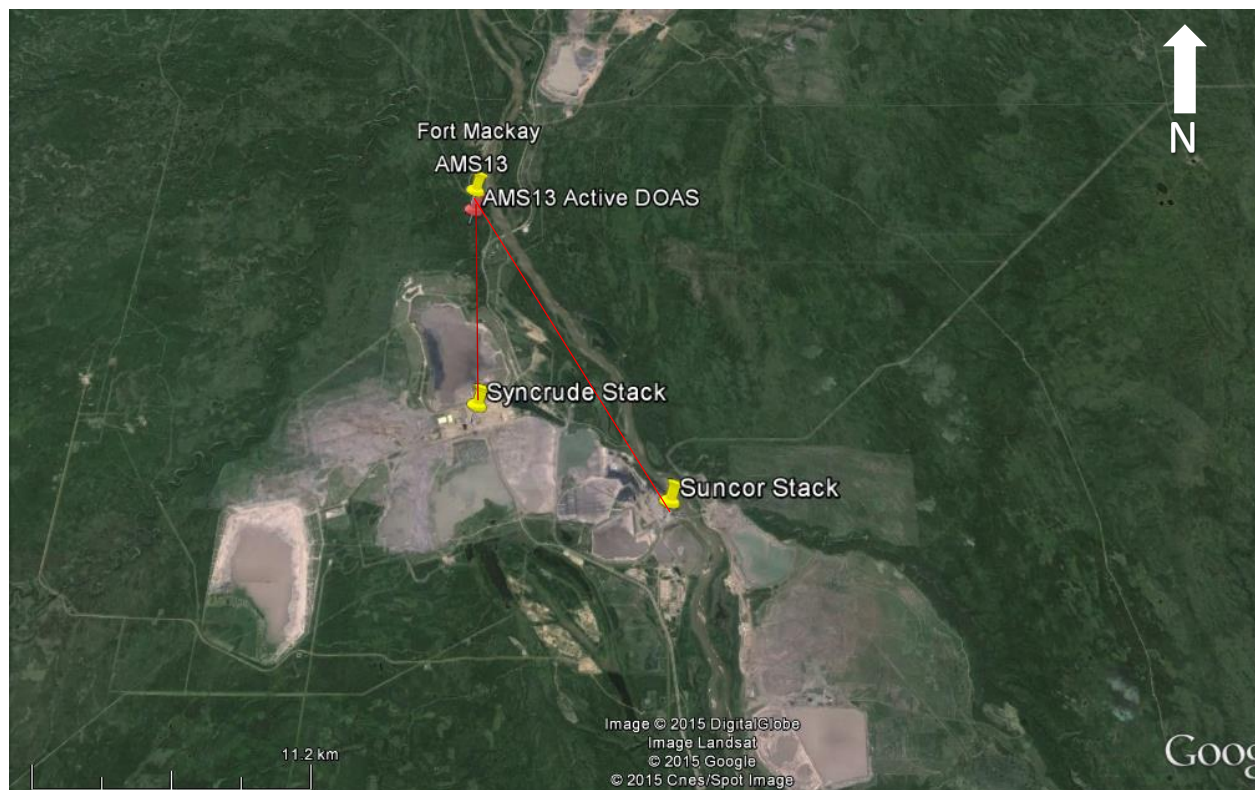


Figure 2.9: AMS13 Measurement Site. Distance from Major Mining Facilities ~ 12 km (source Google Earth)

## 2.2: Combined Active and Lunar DOAS Measurement

$\text{NO}_3$  slant column densities were obtained through application of lunar DOAS as part the proposed research. The conversion of measured SCD into vertical column densities can then be achieved through use of the trigonometric relationship between the light path and the lunar zenith angle (LZA), the angle made between the zenith (vertical), and the telescope lunar line of sight or alternately the lunar elevation angle (LEA) ( $\text{LEA} > 5^\circ$ ):

$$\text{VCD} = \text{SCD} \times (\cos(\text{LZA})) = \text{SCD} \times (\sin(\text{LEA})) \quad (\text{E 2.1})$$

It is important to note the equation E 2.1 cannot be used in instance when the moon is close to the horizon, as the curvature of the earth must then be taken into account (Wagner et al. 2000). This is not the case in the present work.

Measurements taken in low-latitude regions (Lal et al. 1996) have observed that the use of a high zenith angle solar spectrum and a low zenith angle lunar spectra as background helped to improve the overall fit of the nitrate radical. The inclusion of a cross section of water vapor in the  $\text{NO}_3$  fit region is also necessary in order accurately quantify  $\text{NO}_3$  column densities (Wagner et al 2000). Measurement of surface mixing ratios of  $\text{NO}_3$  through use of long path DOAS on different axis aligned over different altitude ranges has also been well established experimentally. This is achieved though mounting retro-reflectors at differing heights on tall buildings within an urban area (Stutz et al. 2004). The combination of these two methods of measurement on a given night is theorized to allow the determination of the change in  $\text{NO}_3$  abundance within different layers of the troposphere and stratosphere with increasing height. This method has been previously performed experimentally at the Table Mountain Facility in Boulder Colorado from May 2003 to September 2004 (Chen et al. 2011), with nocturnally averaged  $\text{NO}_3$  columns found to be  $\approx 5\text{--}7 \times 10^{13}$  molec  $\text{cm}^{-2}$  during the winter centered season (October through March), and  $5\text{--}22 \times 10^{13}$  molec  $\text{cm}^{-2}$  during the summer centred season (April through September). Comparison of the measured columns to values obtained from a 1-D stratospheric model found the model values to be much lower than the experimental results. This may be due to a significant quantity of  $\text{NO}_3$  present within the residual layer, yet still dependent upon  $\text{NO}_3$  present within the stratosphere. The determination of  $\text{NO}_3$  levels present both at the surface and at height within an urban setting (York University) thus serves as the primary purpose of the presented research.

### **2.2.1: Location and Instrumentation**

Measurements were performed using both active DOAS and lunar DOAS simultaneously at York University, Toronto (Lat: 43.773°N Long: 79.504° W). The area is strongly affected by anthropogenic emissions, particularly vehicular emissions due to its proximity to three major highways. Highway 400 (2.3 km east), Highway 401 (6 km south), and Highway 407 (1.7 north) acts as the major source of NO<sub>x</sub> within the region. Southern wind transport of freshly emitted pollutants from the downtown core of Toronto located 17 km to the southeast, as well as aged polluted air mass from the USA, can also serve to a potential source of NO<sub>x</sub> to the area. The northern air sector is typically cleaner, primarily composed of biogenic emissions, and aged air masses (Wojtjal et al. 2013). Finally, at the time of these experiments, there was a great deal of construction present near and within the University campus, as part of the preparations for the Pan and Para-Am games, and the construction of a dedicated subway line to the university. This may act to increase observed pollutant levels.

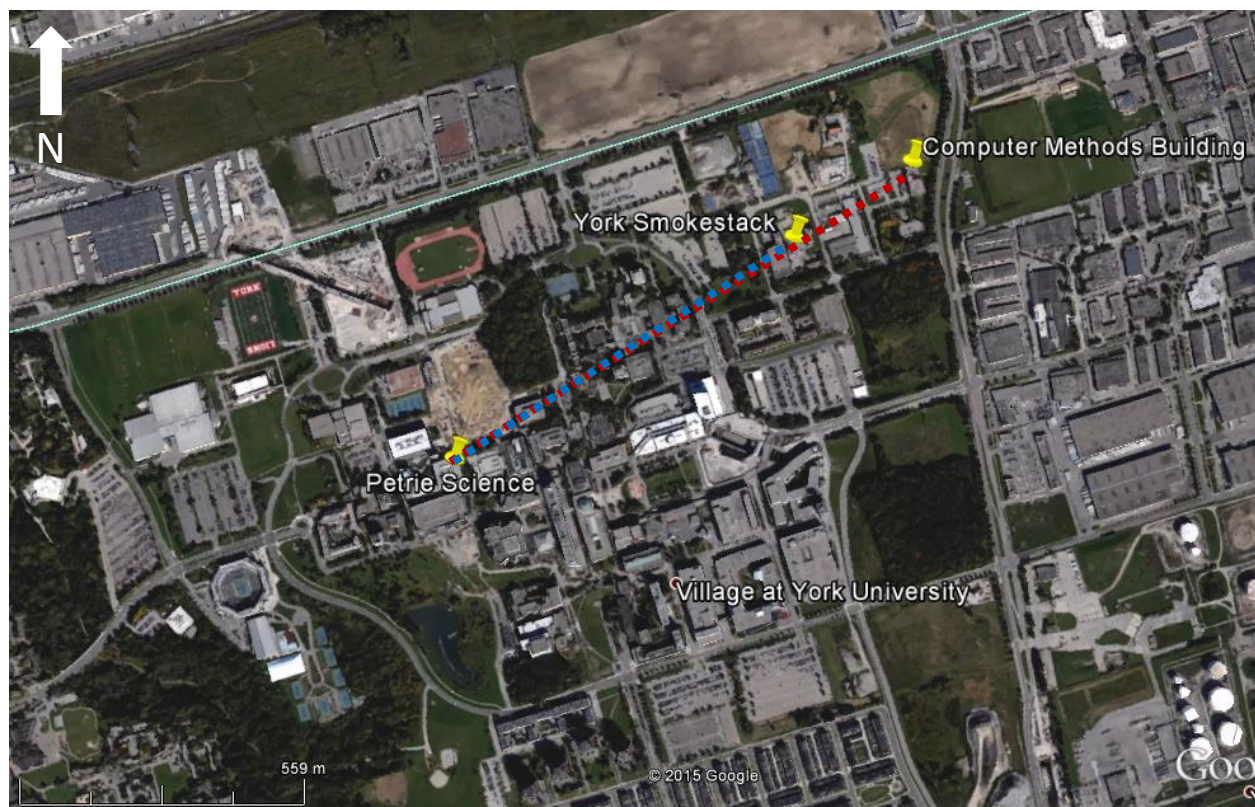


Figure 2.10 Site Location for active and lunar measurement of  $\text{NO}_3$  at York University. Coloured lines indicate the light beam paths of 30 corner cube (red) located on the Computer Methods Building and 7 corner cube (blue) retro reflector locate atop the York University Central Utilities Smokestack, comprising path lengths of 2.2 km and 1.6 km respectively (source Google Earth).

To obtain lunar DOAS measurements, a 40 cm Meade LX200 Schmidt-Cassegrain telescope (focal length: 4064mm, f/10), in the York University Observatory, was used during a five day period centred on the full moon. A computerized mount is used to keep the telescope tracked on the moon, accounting for the moon's progression across the night sky, with manual adjustment possible to maximize intensity. The angle covered by the diameter of the full moon is  $0.5^\circ$ , and thus the uncertainty in the LEA is  $0.25^\circ$ . Using equation 2.1 and the range of elevation angles used in these experiments (LEA =  $14\text{-}27^\circ$ ), the resulting propagated error in the VCD does not exceed 2%. The moonlight was directed into a  $0.6\ \mu\text{m}$  fibre optic cable through use of a custom fibre optic coupler placed in the telescope eyepiece (10mm focal length lens, f/2 BK-7

glass) connected. Spectra were collected by using an Ocean Optics USB2000+ spectrometer (Grating #6, 2048 element CCD, 25  $\mu\text{m}$  slit) with a wavelength range of 493.3-828.4 nm. Like the HONO data collected at AMS13, the raw data were transferred to a computer using a USB connection to be fit with DOASIS. Sample integration times range from 200-600 ms with 1000 averages depending on illumination of the moon on the date of analysis.

Active measurement was achieved through use of the same active DOAS apparatus used during the field study at AMS13. A weather-proofed, 30 corner cube retro-reflector was placed upon the Computer Methods Building of the York University Campus in the fall of 2013, which acts to reflect the light beam back to the telescope. The total return path length 2.2 km and the retroreflector is mounted roughly 17m above ground level. Taking the height of the telescope into account, the average height of the light beam is roughly 16m. A second 7 corner cube retro-reflector is mounted at an elevated position (57.6 m) upon the York University Central Utilities Smokestack, with at total path length of 1.6 km. This results in an average beam height of 56m. The DOAS telescope can be manually adjusted to focus on either of these two retro reflectors in order to obtain multiple point measurements of the nitrate radical at differing heights based on the overall return path length of the light beam. Like the passive lunar analysis, a 0.6  $\mu\text{m}$  fibre optic cable connects the telescope to a temperature regulated Ocean Optics S2000 spectrometer. The spectrometer is in turn connected to a computer for storing of the raw data. Due to an extremely high return signal from the 30-cube retro-reflector, a quartz glass diffusor was installed in the active DOAS apparatus to prevent the saturation of sample spectra. The resulting reduction of light intensity limited the integration for collection to 10 ms, but allowed the complete focussing of the return beam spot into the fiber optic. Active measurement of both  $\text{NO}_3$  and  $\text{NO}_2$  were performed by this apparatus to demonstrate the viability of the experimental set-up. These

measurements took place during the nights of May 31<sup>st</sup>-June 4<sup>th</sup> 2015, with additional data collected in July 1<sup>st</sup> and 2<sup>nd</sup>.

### **2.2.2: Lunar DOAS Fitting Procedure:**

Much like active fitting performed using the data from the AMS13 site, sample spectra were corrected through use of electronic offset and dark current spectra. Integration time for the offset spectra were 3 ms, with 10000 averages. Dark current spectra were taken with an integration time of 15 sec and 5-40 averages. Wavelength calibration was performed using a combination of both a mercury lamp and a red helium neon gas laser (Thorlabs Inc,  $\lambda = 632.8$  nm, int. time: 500 ms, 1000 averages). The fibre-optic cable was exposed to light from both the Hg lamp and laser, and calibration lines at 546.07 nm, 576.96 nm, and 579.09 nm, as well the HeNe line at 632.80 nm were collected. The laser line served as the convolution kernel for the reference spectra, being within the fit range for NO<sub>3</sub>. The FWHM for the convolution is of  $\approx 0.9$  nm at 15°C.

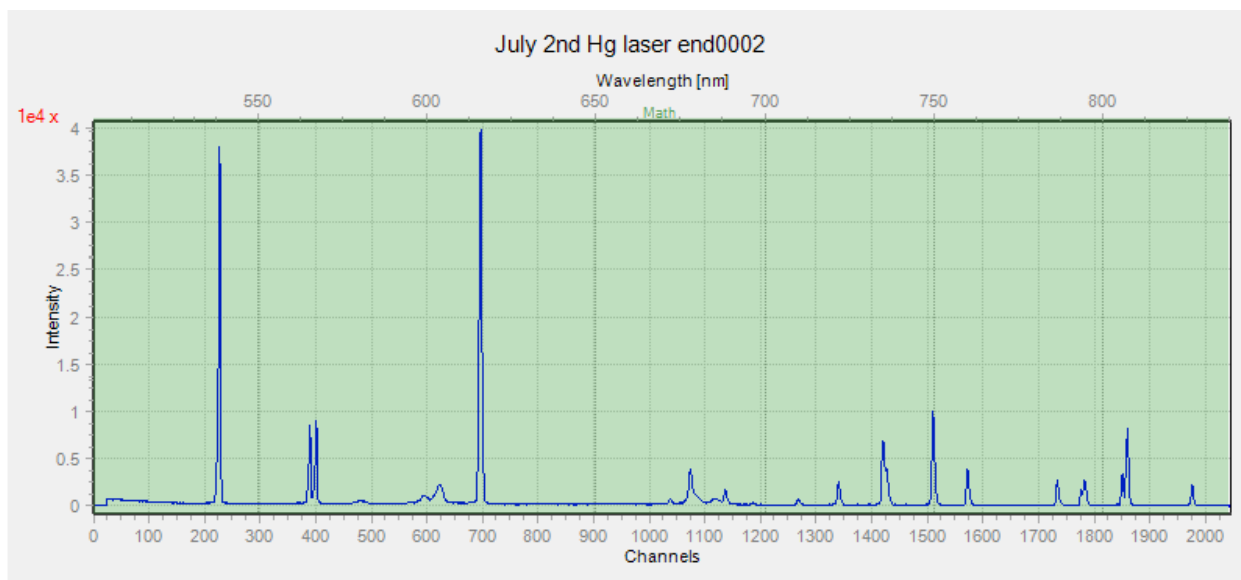


Figure 2.11: Sample Hg lamp / laser spectra taken July 2<sup>nd</sup> 2015 using USB 2000+ spectrometer with int. time 500 msec, 1000 averages, and temperature stabilized at 15°C. Corrected for offset and dark current.

### 2.2.3: NO<sub>3</sub> fitting procedure for lunar DOAS:

Fitting the sample spectra using lunar DOAS required a fit scenario containing reference spectra for NO<sub>3</sub> (Yokelson et al., 1994), water vapour (Coheur et al., 2002), Fraunhofer lines and moonlight reference spectra collected at sunrise when NO<sub>3</sub> concentration was known to be low. Due to the heterogeneity of atmospheric temperatures across the long path length of the collected moonlight, the NO<sub>3</sub> cross section used was taken at 280 K to account for the large range of potential temperatures in the slant column. A high pass binomial filter was applied to the sample and reference spectra, along with a 2<sup>nd</sup> order polynomial in order to account for broadband effects (Chen et al. 2011). NO<sub>3</sub> is known to have prominent absorption features present at 623 and 662 nm. However the presence of a hydrogen alpha line at 656 nm acts to interfere with the fit of NO<sub>3</sub>. Three separate fit ranges were tested using the 623 nm feature (617-633 nm), the 662 nm feature (658-671nm) and both features (617-671 nm). Through comparison of chi-squared values, it was found that the highest accuracy was observed through use of the 662 nm feature

only, and thus the 658-671 nm fit range was used for the presented results, although the 623 feature was used to ensure qualitatively the presence of  $\text{NO}_3$ .

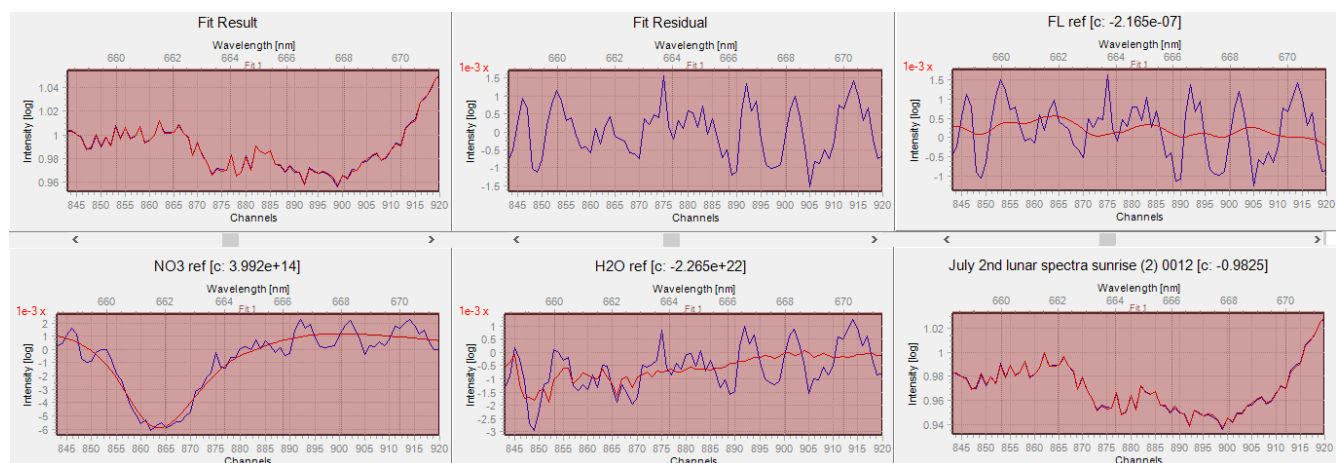


Figure 2.12: DOASIS  $\text{NO}_3$  fit output taken on July 2<sup>nd</sup> 2015 at 11:08 pm. The  $\text{NO}_3$  VCD is found to be  $1.0 \cdot 10^{14} \pm 8.0 \cdot 10^{12}$  molecules per  $\text{cm}^2$ .

## 2.2.4: $\text{NO}_3$ and $\text{NO}_2$ fitting procedure for active DOAS measurements:

Fitting of sample spectra collected through active DOAS for both  $\text{NO}_3$  and  $\text{NO}_2$  follows a similar procedure for fitting the data collect from lunar DOAS. In the case of  $\text{NO}_3$ , the same reference spectra and fitting range were used, the exception being the inclusion of lamp spectrum to account for the high pressure Xe-lamp.  $\text{NO}_2$  measurement made additional use of  $\text{NO}_2$  reference spectra (Vandele et al. 1998), as well as a lamp spectrum and a morning reference spectrum obtained from a sample spectra taken either at sunset or the early morning. The  $\text{NO}_2$  fit range used experimentally was 560-585 nm. Manual adjustment of the active DOAS instrument at regular intervals over the course of the night allowed the determination of both  $\text{NO}_3$  and  $\text{NO}_2$  mixing ratios at differing heights during nights of combined analysis.

### 2.2.5: Temperature Dependence of NO<sub>3</sub> Cross Section:

A key difficulty in lunar measurement of NO<sub>3</sub> is the variation of temperature along the path length. Direct measurement of moonlight provides information on trace gas concentration integrated along the total atmospheric column. Thus, the measured SCD always contains contributions from all layers of the atmosphere. Given that the absorption cross sections of both NO<sub>3</sub> and water are known to be temperature dependant, the variation of determined NO<sub>3</sub> VCDs due to temperature dependence acts as a key source of uncertainty for the presented results. Investigation into the temperature dependence of the NO<sub>3</sub> cross section at 662.2 nm over the temperature range of 298-388K was performed (Osthoff et al. 2007). When combined with previous data in the 200-298 K region, it was found that the absorption cross section  $\sigma$  could be expressed by the following equation:

$$\sigma_{662} = [(4.582 \pm 0.096) - (0.00796 \pm 0.00031) \cdot T] 10^{17} \text{ cm}^2 \cdot \text{molecules}^{-1} \quad (\text{E } 2.1)$$

The resultant measured values for  $\sigma$  found a net decrease with increasing temperature, and was observed to agree with predictions by Orphal et al. in 2003, who described the temperature dependence of the NO<sub>3</sub> cross section in the 200-298K range:

$$\sigma(T) = \sigma(298) \cdot \frac{1 - e^{-1096.4/T} - 2e^{-529.5/T}}{1 - e^{-1096/298} - 2e^{-529.5/298}} \quad (\text{E } 2.2)$$

Based on the above calculations, it was found that the NO<sub>3</sub> cross section can increase by roughly 34% as the temperature decreases from 298K to 200 K. Given that temperatures in the tropopause can reach -50°C (223 K), the observed change in the cross section is relevant to the component of the NO<sub>3</sub> VCD present both in the stratosphere and the free troposphere. For this reason a NO<sub>3</sub> reference spectra collected at lower than room temperature (Yokelson *et al.* (1994, 280K) was used in order to account for decreasing temperature with increased elevation above

ground level. Use of NO<sub>3</sub> reference spectra taken at 280 K acts to reduce the percent difference in the calculated values of  $\sigma_{662}$  as the atmospheric temperature decreases with height, as shown in Table 2.2:

Table 2.2: Summary of calculated NO<sub>3</sub> cross sections and percent difference at varying temperatures

| Temperature (K) | $\sigma_{662 \text{ calc}}$<br>( $10^{-17} \text{ cm}^2 \text{ molecule}^{-1}$ ) | Percent Difference<br>(298K) | Percent Difference<br>(280K) |
|-----------------|--|------------------------------|------------------------------|
| 298             | 2.29   |                              | -6.2                         |
| 290             | 2.36   | 2.9                          | -3.4                         |
| 280             | 2.44   | 6.6                          |                              |
| 260             | 2.61   | 13.8                         | 6.8                          |
| 240             | 2.77   | 20.9                         | 13.4                         |
| 220             | 2.93   | 27.7                         | 19.9                         |
| 200             | 3.07   | 34.2                         | 25.9                         |

Surface temperatures were observed to vary on both night of analysis between 20°C in the early night just after sunset to as low as 10°C in the early morning. At these temperatures the observed change in the absorption cross section is limited to a few percent when using both 298 and 280 K, and thus would not have significant impact upon the resulting NO<sub>3</sub> concentration determined through use of active DOAS. At temperatures found in the upper troposphere and stratosphere, use of a reference spectra taken at 280 K acts to generate smaller levels of percent error between the different constituents of the total atmospheric column, and thus provides a more accurate representation of the observed vertical profile. Use of stratospheric values of NO<sub>3</sub> taken from literature helped to minimize the potential error that could have been observed if solely measured values were used in the determination in the stratospheric component of the NO<sub>3</sub> VCD.

## **2.2.6: NO<sub>x</sub> and O<sub>3</sub> measurement by chemiluminescence and UV photometry**

As part of an effort to determine the potential impact of the Pan and Parapan-Am games taking place in Toronto over the summer of 2015 upon observed pollutant levels, the Ontario Ministry of Environment set up both a nitrogen oxide chemiluminescent analyser (Thermo Scientific Model 42i) and a UV photometric ambient ozone analyser (Thermo Scientific Model 39i) at York University in the CAC Air Quality Research Station (5<sup>th</sup> floor Petrie Building). The determination of NO<sub>x</sub> mixing ratios is performed through the initial reduction of all nitrogen oxides present to NO by passing the sampled air mass over a heated Mo catalyst. Reaction of the NO with O<sub>3</sub> produced in excess in the instrument yields NO<sub>2</sub>, a small percentage of which is in the excited state. The measurement of the light produced by the decay of this excited state of NO<sub>2</sub> allows the concentration of NO<sub>x</sub> to be determined. The automatic switching of the catalyst in and out of the sample line allows NO and NO+NO<sub>2</sub> to be determined alternately on an x second time scale. NO<sub>2</sub> is determined by difference of the two signals. A caveat of the instrument is that the NO<sub>2</sub> determined in this way may also include a small fraction of other nitrogen species that are reduced by Mo to NO. The fraction of interfering secondary species (HNO<sub>3</sub>, HONO, N<sub>2</sub>O<sub>5</sub>, etc.) is typically small in the urban area where primary NO<sub>x</sub> species dominate. Ambient O<sub>3</sub> mixing ratio is determined based on molecular absorption; the attenuation of light at 254 nm within an absorption cell, with an additional cell measuring a reference gas (ambient air flowing through a charcoal ozone scrubber). Both sample and reference cell switch after initial measurement, resulting in an average signal from both sample and reference based on the two cell measurements. Both instruments sample air from an inlet located on the roof of the Petrie Science Building (16 m a.g.l) within the same lab as active DOAS telescope beam start location.

### **2.2.7: Meteorological Measurements at York University**

Measurements of air temperature, relative humidity,  $\Delta T (T_{9.5m} - T_{1m})$ , corrected wind speed and direction, total precipitation, down welling short wave and long range radiation were all collected day and night by the Earth and Space Science and Engineering Meteorological Observation Station (EMOS). The station is located in front of the Tait Mackenzie Building, allowing real-time data collection of weather data on the York University campus. This data is of particular importance in the determination on whether the atmosphere of a given night is stable or unstable, which can drive differences in the mixing ratio and temporal behaviour of various chemical species.

# Chapter 3: NO<sub>3</sub> Measurement at York University

## 3.1: Measurement overview

Measurements of NO<sub>3</sub> at York University using lunar DOAS and active DOAS are summarized in the subsequent sections. Sample collection using the lunar DOAS apparatus was performed by the author, while measurement using active DOAS was done by William Fujs. Spectral fitting of data was performed by both William Fujs and the author. Difficulties in combined analysis stemmed from dependence of lunar DOAS on clear sky conditions and the lunar cycle. Even a small degree of cloud cover present across the sky acted to drastically reduce observed signal from the moon. Since the optimum period of collection for combined analysis was a five day period centred on the full moon (total illumination 95-99.9%), cloud cover acts as the significant limiting factor to this type of analysis. Additionally, measurement in the winter months proved difficult due to cold temperatures causing instrument failure in the computerized mount of the telescope. Data was collected during the months of June and July 2015, when both instruments were set-up and optimized for analysis. In particular, the nights of June 3<sup>rd</sup> and July 2<sup>nd</sup> will be presented, as they represent times when both active and passive measurements were taking place uninterrupted over the course of the night. Vertical column densities of NO<sub>3</sub> collected shall be presented alongside surface NO<sub>3</sub> mixing ratios for both nights. From these measurements, we can say something about the distribution of NO<sub>3</sub> vertically during the two nights of analysis. Ozone and NO<sub>2</sub> collected by the Thermo Scientific instruments are also presented. Lunar DOAS measurement for the selected nights of analysis commenced immediately following the moon becoming visible in the night sky. Due the proximity of the York University Observatory to surrounding buildings, collection of lunar spectra precisely at

sunset was not viable, as the moon usually took roughly an hour to become fully visible to the telescope. For this reason, a lunar reference spectra collected at dawn is used for both nights of analysis. This had the added advantage of decreasing the possibility of an unknown quantity of  $\text{NO}_3$  being present within the reference spectra due to daytime photolysis.

### 3.2: June 3<sup>rd</sup>-4<sup>th</sup> case study

The  $\text{NO}_3$  VCDs for the June 3<sup>rd</sup> night is presented in Figure 3.1:

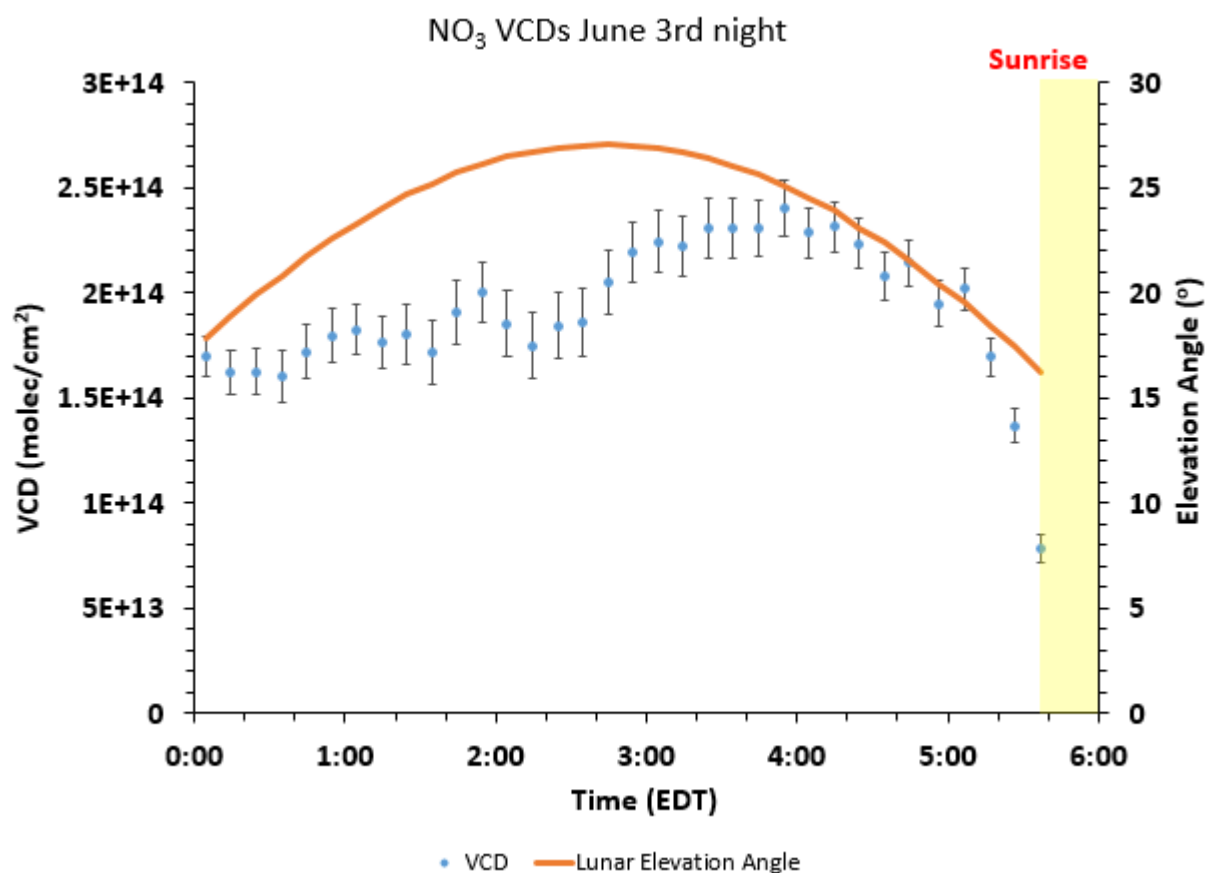


Figure 3.1:  $\text{NO}_3$  VCDs collected on June 3<sup>rd</sup> 2015

Spectra collected on June 3<sup>rd</sup> had reduced intensity due to the moon being in the waning gibbous phase (total illumination 96.8%). An integration time of 600 ms was used in order to

account for this, although this acted to limit the total number of data points collected over the night. Slant column densities were converted into vertical column densities based on the known lunar elevation angle (LEA) and equation 2.1. It was found that that the  $\text{NO}_3$  VCDs increased as  $\text{NO}_3$  built up during the night until reaching a nocturnal steady state. The  $\text{NO}_3$  column then undergoes rapid decay at sunrise (5:00-6:00 am). Maximum observed  $\text{NO}_3$  VCDs were found to be  $2.4 \cdot 10^{14}$  molecules $\cdot\text{cm}^{-2}$ , occurring at roughly 4:00am.

$\text{NO}_3$  mixing ratios determined at the 56m beam height are shown in Figure 3.2:

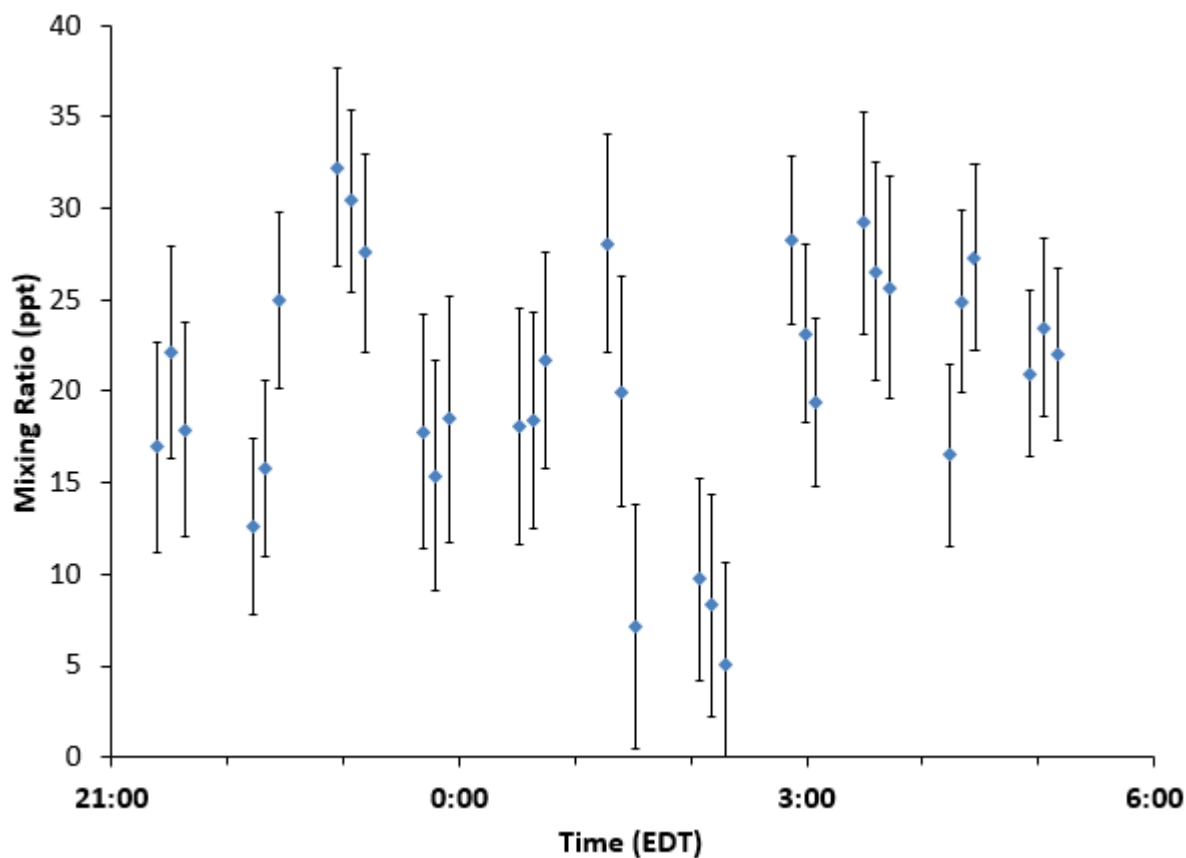


Figure 3.2:  $\text{NO}_3$  mixing ratios determined using active DOAS at the 56m beam height on June 3<sup>rd</sup>

In regard to the mixings ratios taken using active DOAS, it was found that the required integration time was much higher with respect readings taken at the 56m beam height, largely due to the fact that a smaller retro-reflector was mounted in that position (200 ms int. time, 2000 averages). In comparison, the 16m position displayed an excellent return signal (7 ms int. time, 30000 averages). The collected data was fit using the 657-662 nm (one feature) fitting range. Low values were found to occur predominantly, with maximum values ~ 30 ppt observed at the 56m beam height. Investigation into the conditions present during the night of analysis found possible interference in the 16m light path by steam from a nearby smokestack, and as such this data is not presented. This is a persistent problem with the current experimental set-up, and may have to be addressed in future work, as it has been seen to reduce the intensity of the reflected light, and thus the determined  $\text{NO}_3$  abundance.

A summary of the meteorological conditions present during June 3<sup>rd</sup> – 4<sup>th</sup> is presented in figure 3.3:

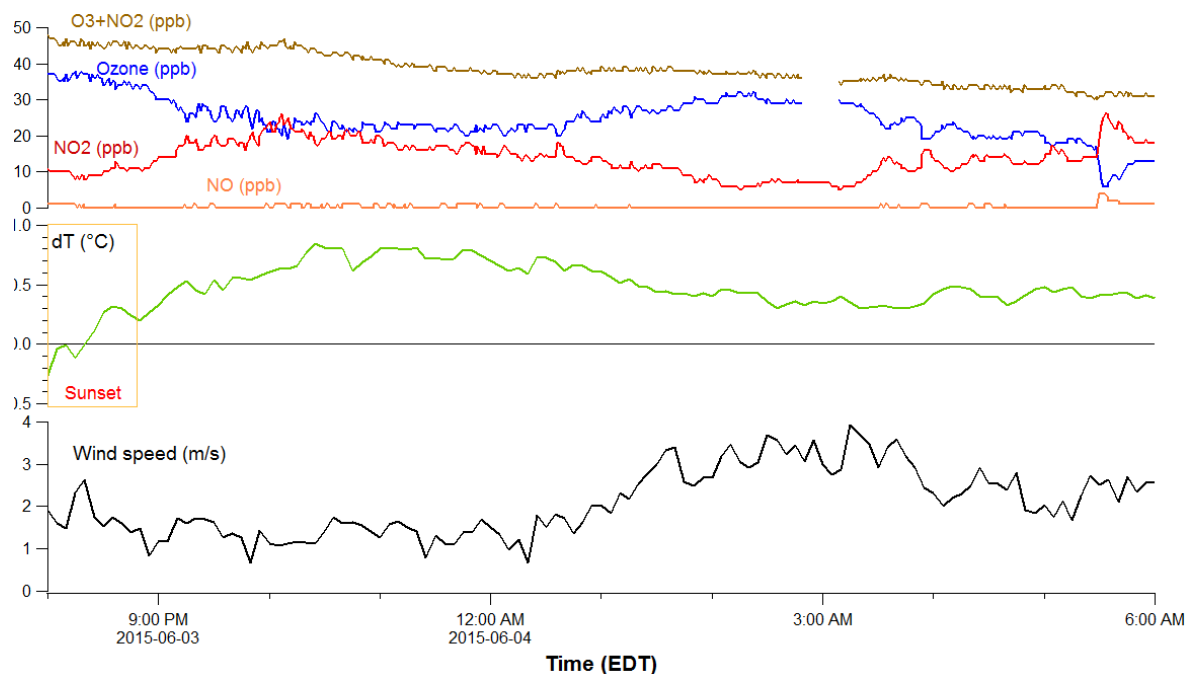


Figure 3.3: Summary of  $\Delta T_{(9.5\text{m}-1.0\text{m})}$ , wind speed,  $[\text{O}_3]$ ,  $[\text{NO}]$ ,  $[\text{NO}_2]$ , and  $[\text{NO}_2 + \text{O}_3]$  from 20:00 to 6:00 on the night of June 3<sup>rd</sup>-4<sup>th</sup>, 2015. Sunset occurred at 20:54

The formation of significant  $\text{NO}_3$  over the course of the night requires unstable meteorological conditions, such that sufficient vertical mixing can occur to prevent ozone from being titrated out through reactions during the night. Such nights are characterized both by a high observed wind speed (greater than 3 m/s), and a negative air temperature gradient with increasing height ( $\Delta T_{9.5\text{m}-1.0\text{m}} < 0.2^\circ\text{C}$ ), which serve to indicate some degree of vertical mixing in the air mass. Additionally, high ozone mixing ratios also serve as a good indicator of formation of the nitrate radical, as well as unstable nighttime atmospheric conditions.  $\text{O}_3$  mixing ratio above 5 ppb are necessary for reaction R 1.10 to occur significantly. However, given that  $\text{NO}$  also reacts with ozone to form  $\text{NO}_2$ , low mixing ratios of  $\text{NO}$  ( $< 2$  ppb) present on a given night can also serve to indicate measureable quantities of  $\text{NO}_3$  are present. Based on these factors, it can be determined if a stable or unstable airmass was present during the displayed nights of combined analysis.

In the case of June 3<sup>rd</sup>-4<sup>th</sup> (fig 3.3), decreasing ozone concentration was initially observed as the night progressed. This was followed by a slight increase observed to occur just after midnight, with O<sub>3</sub> mixing ratios of 29-30 ppb being observed until roughly 3:00 am. Overall, ozone mixing ratios were sufficiently high to allow NO<sub>3</sub> formation, and NO mixing ratios are found to be zero for the vast majority of the night before rising during the morning due to the daily commute. NO<sub>2</sub> levels were increased in the early evening until ~10:00pm, before decreasing as O<sub>3</sub> mixing ratios increased. Wind speeds were found to be low until after midnight, after which they increased above 3 m/s until 3:00 am, serving as an indication of unstable conditions. Wind direction was found to be predominantly ENE, indicating that the observed pollutant levels are due to local sources of NO<sub>x</sub>. Likewise a decrease in  $\Delta T$  is observed to occur over the course of the night during the same timeframe. Both factors serve to indicate moderately unstable night-time conditions on June 3<sup>rd</sup>.

### 3.2: July 2<sup>nd</sup>-3<sup>rd</sup> case study

The NO<sub>3</sub> VCDs observed during the July 2<sup>nd</sup> night are presented in Figure 3.4:

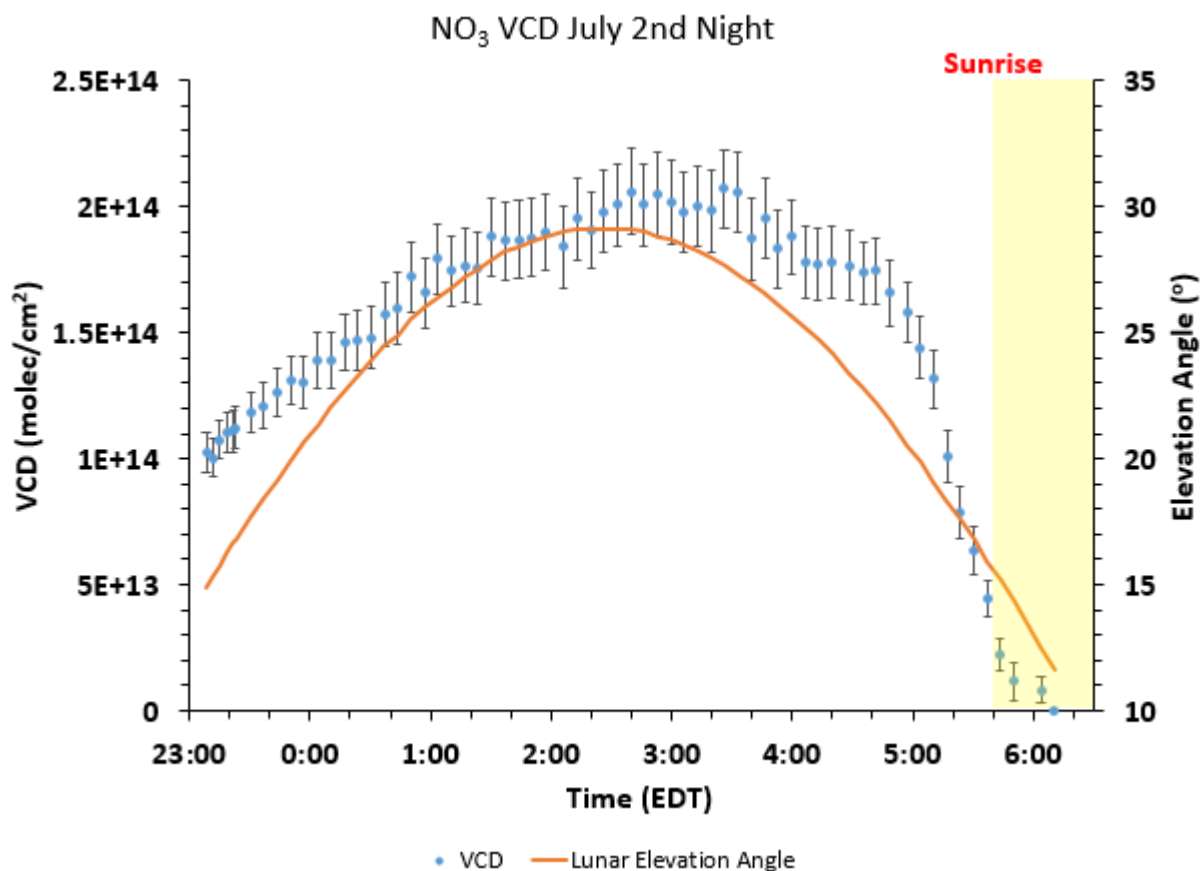


Figure 3.4: NO<sub>3</sub> VCDs collected on July 2<sup>nd</sup> 2015

Data collected on the second night of analysis (July 2<sup>nd</sup>) was collected closer to the date of the full moon (total illumination 99.8%). Thus a smaller integration time of 200 ms was possible, resulting in a larger number of data points being available. Like June 3<sup>rd</sup>, July 2<sup>nd</sup> is characterized by a slow buildup of NO<sub>3</sub> observed at the start of analysis, followed by steady values until the eventual decay observed at sunrise. Maximum observed NO<sub>3</sub> was found to be  $2.0\text{--}2.1 \cdot 10^{14}$  molecules·cm<sup>-2</sup> between 2:30 and 3:30 am.

Measurements of NO<sub>3</sub> mixing ratios along the 56m beam height were not available on July 2<sup>nd</sup>. However, measurements using the 16m beam height were performed, with similar integration to the data previously presented (7 ms int. time, 30000 averages), as presented in Figure 3.5:

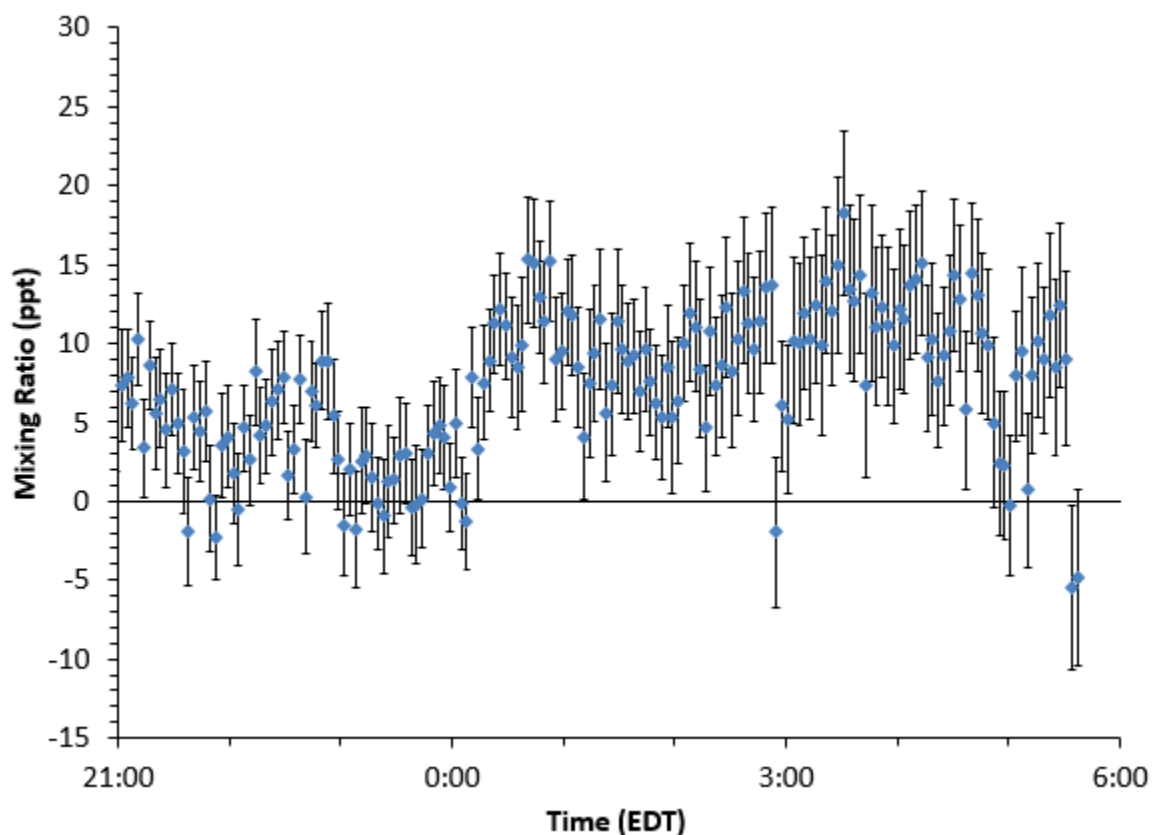


Figure 3.5: NO<sub>3</sub> mixing ratios determined using active DOAS at the 16m beam height on July 2<sup>nd</sup>

The resulting mixing ratios are seen to vary between 10-18 ppt throughout the night. A sharp decrease is observed to occur just before 11:00 pm. This decrease is most likely due to a combustion event, as there is a rapid decrease in ozone and increase in NO and NO<sub>2</sub> observed at the same time. NO<sub>3</sub> mixing ratios are likewise noted to be consistently greater than those observed on the previous night of combined analysis. Unlike the previous month, there appears to be little steam interference over the course of the night, resulting in better fitting.

Meteorological conditions for July 2<sup>nd</sup>-3<sup>rd</sup> are summarized in Figure 3.6:

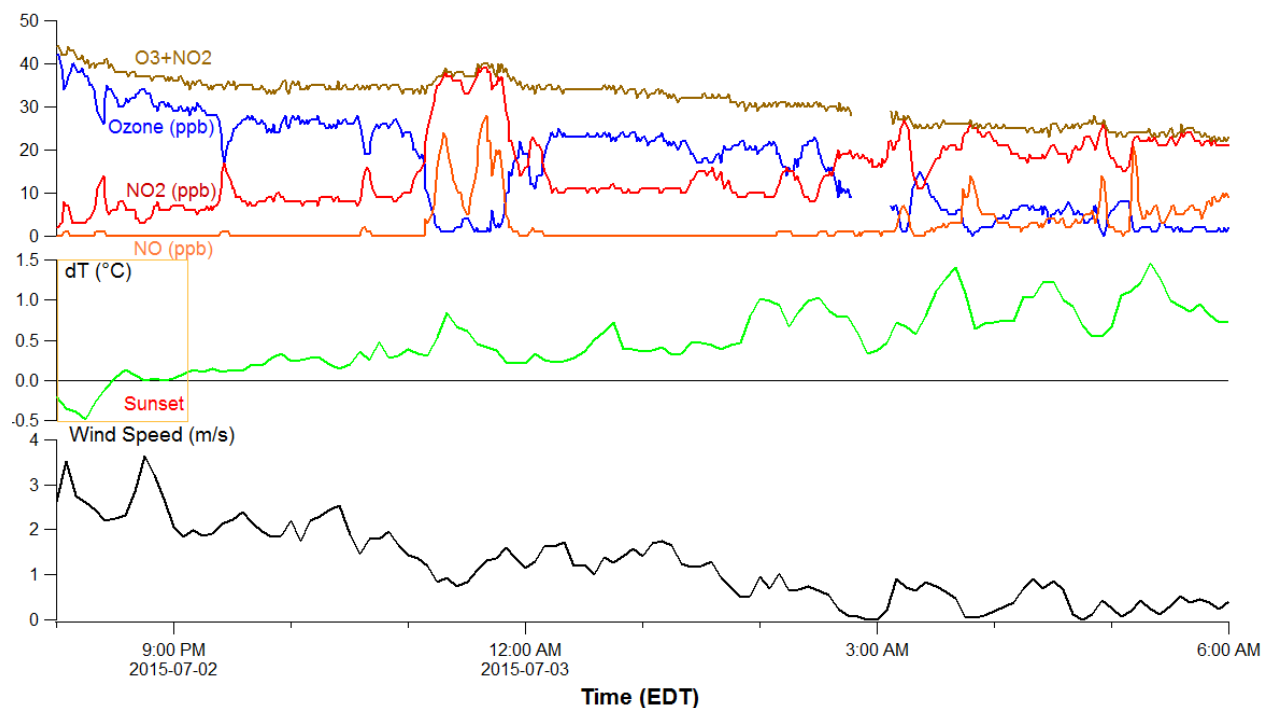


Figure 3.6: Summary of  $\Delta T$  ( $_{9.5m-1.0m}$ ), wind speed,  $[O_3]$ ,  $[NO]$ ,  $[NO_2]$ , and  $[NO_2 + O_3]$  from 20:00 to 6:00 on July 2<sup>nd</sup>-3<sup>rd</sup>. Sunset occurs at 21:03

Ozone,  $NO_2$  and  $NO$  levels during the night of July 2<sup>nd</sup> are found to undergo rapid fluctuations both from 11:00pm-12:00am, and in the early morning (3:00 am- 4:00 am). In both instances,  $[O_3]$  rapidly decreases to near-zero mixing ratios due to a sudden increase in  $NO$  and  $NO_2$ , most likely caused by local emissions. Overall wind speeds were observed to decrease as the night progresses, with the primary wind direction being from the NW. This once again acts to limit the influx of polluted air mass present, indicating the observed  $NO$  likely originated from a local source. Values for  $\Delta T_{9.5m-1.0m}$  were found to be lower overall than the previous month, but a net increase was still observed as the night progressed. Despite these factors, there is

sufficient  $O_3$  for most of the night to indicate a moderately unstable night overall, with moderate observed  $[NO_3]$  found at the surface.

### **3.3: Stratospheric $NO_3$ levels on selected nights**

The column abundance of  $NO_3$  in the stratosphere appears to display a close relationship with the highest latitude experienced by the stratospheric air mass prior to its arrival in mid latitude regions (Norton and Noxon, 1986). Stratospheric air transported from higher latitudes are observed to have lower  $NO_3$  due to the low temperatures (below 240 K) present shifting the thermal equilibrium to favor  $N_2O_5$  formation (Norton and Noxon, 1986). Likewise,  $NO_3$  abundance in the stratosphere is often observed to dip below instrumental detection limits during the winter months, with  $NO_3$  VCDs of  $1.0 \cdot 10^{13}$  molecules/cm<sup>2</sup>. Determination of the total  $NO_3$  column abundance present in the stratosphere globally through use of the space borne Global Ozone Monitoring by Occultation of Stars (GOMOS) instrument found values below  $2.0 \cdot 10^{13}$  molecules/cm<sup>2</sup> during polar fall and winter, increasing to as high as  $4.0 \cdot 10^{13}$  during the spring and summer (Hauchcorne et al. 2005). This observed variation has been link to the temperature of the upper stratosphere. Figure 3.4 demonstrates the global distribution of stratospheric  $NO_3$  during the year at differing latitudes:

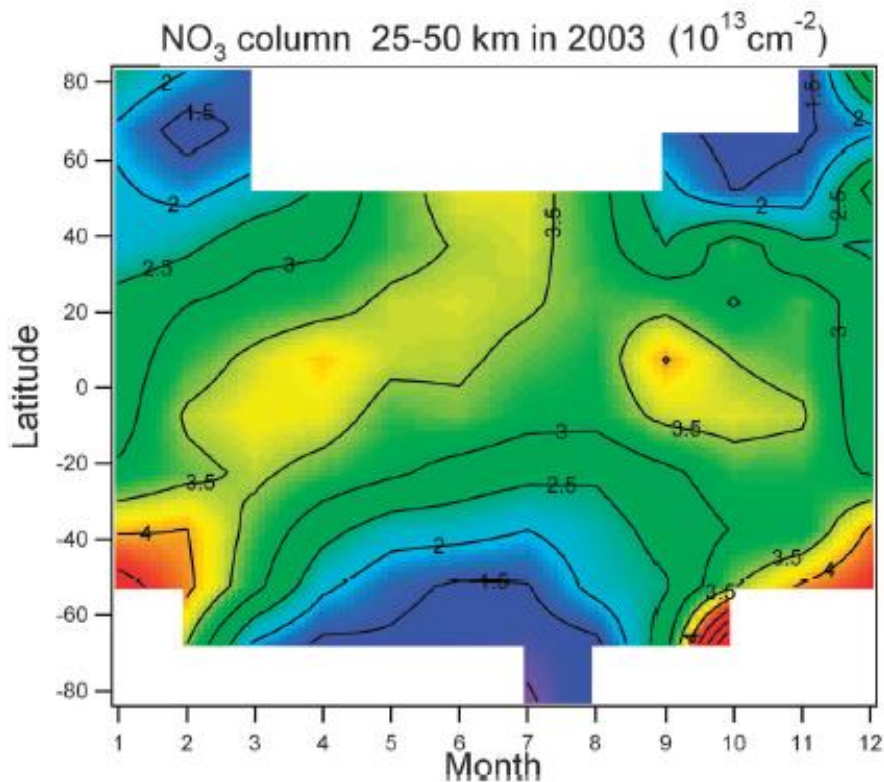


Figure 3.7: Global Distribution of  $\text{NO}_3$  (25-50km) in 2003 (Hauchecorne et al. 2005)

Both nights of analysis take place during the early summer in an urban environment, with large potential  $\text{NO}_x$  present nearby in the planetary boundary layer from urban sources. Due to the large timescales involved in the vertical transport of polluted air mass to the stratosphere (months), the observed stratospheric abundance at the site should not differ too greatly from the global distribution presented in literature. Thus, the stratospheric component for both nights is estimated to be in the range of  $3.5\text{-}4.0 \cdot 10^{13}$  molecules / $\text{cm}^2$ . Similar values for  $\text{NO}_3$  vertical profiles have been reported in mid-latitude regions through use of stellar and lunar occultation over the course of several research studies, through use of ground measurements, (Smith and Solomon, 1990), balloon measurements (Naudet et al., 1989, Renard et al., 2001, Renard et al., 2005), as well as geographical coverage via satellite (Amekudzi, et al. 2005). In each of these studies, maximum  $\text{NO}_3$  mixing ratios were observed at an altitude of 32-40km, due to the fact

that atmospheric temperature below 35 km is observed to be low enough to render the thermal decomposition of  $\text{N}_2\text{O}_5$  negligible. Maximum concentrations have been found to vary between  $2.0\text{-}3.4\cdot 10^7$  molecules /  $\text{cm}^3$  within this altitude range. However, enhancements in the lower stratosphere (as low as 16km) during some of the balloon based measurements (Renard et al. 2001). These variations cannot be explained through use of temperature gradients, and are not observed by ground-based measurements. While these enhancements were found to result in a slight increase in observed  $\text{NO}_3$  VCDs in the stratosphere, they should be given due consideration as a source of uncertainty in the suggested values for stratospheric  $\text{NO}_3$  abundance. Despite this, given previously established research into  $\text{NO}_3$  vertical profiles the expected column densities at the experimental latitude ( $43^\circ\text{N}$ ) of  $3.5\text{-}4.0\cdot 10^{13}$  molecules/ $\text{cm}^2$ . This shows that the stratospheric component of the  $\text{NO}_3$  VCD is a small fraction of the total VCD we have measured by Lunar DOAS on both nights.

### 3.4: Vertical Distribution of $\text{NO}_3$

Based on the  $\text{NO}_3$  VCDs collected for both nights, a simple tabulation of overall vertical distribution of  $\text{NO}_3$  can be performed.  $\text{NO}_3$  abundance during a given night is spread between the stratosphere, free troposphere, residual layer, and nocturnal boundary layer:

$$\text{VCD}_{\text{total}} = \text{VCD}_{\text{Lunar}} = \text{VCD}_{\text{NBL}} + \text{VCD}_{\text{RL}} + \text{VCD}_{\text{Free trop.}} + \text{VCD}_{\text{strat.}} \quad (\text{E } 3.1)$$

Previous determination of vertical profiles of tropospheric  $\text{NO}_3$  through spectroscopy of scattered sunlight in off-axis geometry during sunrise of a polluted urban environment found the maximum at  $\sim 350\text{m}$  (Friedelburg et al. 2002). Given the vertical stratification of the PBL at night, and the

limited degree of airborne pollutant emissions entering the free troposphere,  $VCD_{\text{Free trop.}}$  is presumed to be  $\sim 0$ . Stratospheric  $\text{NO}_3$  abundance used for these calculations will be  $3.5 \pm 0.5 \cdot 10^{13}$  molecules/cm<sup>2</sup>, based on data presented in section 3.3.

As reported in the introduction the height of the nocturnal boundary layer can occur at an altitude between 50-200m. Both nights experienced clear sky conditions with lower wind speeds observed as the night progressed, which encouraged rapid radiative cooling of the surface and slow transfer of heat from air to surface. Under these moderately unstable conditions, it is reasonable to assume that the boundary layer height for both nights began at roughly 100-150m. The abundance of  $\text{NO}_3$  can then be calculated on both night based on the surface mixing ratios determined through active DOAS, and the estimated thickness of the NBL ( $150 \pm 100$ m). The average  $\text{NO}_3$  mixing ratio was determined between 3:00-4:00am, at which time all the  $\text{NO}_x$  present should have come to equilibrium. It was found that the average  $\text{NO}_3$  mixing ratio at these times was found to be 25 ppt on June 3<sup>rd</sup>-4<sup>th</sup>, and 12 ppt on July 2<sup>nd</sup>-3<sup>rd</sup>. A greater degree of accuracy could be applied to these finding had both retro-reflectors been operating at optimum capacity during both night, and the experimental error that prevented this from occurring will have to be addressed in future work. However based on the values obtained, an estimate of  $VCD_{\text{NBL}}$  can be calculated for June 3<sup>rd</sup>-4<sup>th</sup> and July 2<sup>nd</sup>-3<sup>rd</sup> to be  $0.92 \cdot 10^{13}$  molecules/cm<sup>2</sup> and  $0.44 \cdot 10^{13}$  molecules/cm<sup>2</sup> respectively.  $\text{NO}_3$  abundance within the residual layer can thus be calculated through rearrangement of equation E 3.1. The results are tabulated in Table 3.1:

|                                       | VCD <sub>Lunar</sub><br>(molecules/cm <sup>2</sup> ) | VCD <sub>Free trop.</sub><br>(molecules/cm <sup>2</sup> ) | VCD <sub>strat</sub><br>(molecules/cm <sup>2</sup> ) | VCD <sub>NBL</sub><br>(molecules/cm <sup>2</sup> ) | VCD <sub>RL</sub><br>(molecules/cm <sup>2</sup> ) |
|---------------------------------------|--|---|--|--|---|
| June 3 <sup>rd</sup> -4 <sup>th</sup> | 2.3±0.06·10 <sup>14</sup>                            | 0   | 3.5 ± 0.5 ·10 <sup>13</sup>                          | 0.92 ± 0.06·10 <sup>13</sup>                       | <b>1.9±0.1·10<sup>14</sup></b>                    |
| July 2 <sup>nd</sup> -3 <sup>rd</sup> | 1.9±0.06·10 <sup>14</sup>                            | 0   | 3.5 ± 0.5 ·10 <sup>13</sup>                          | 0.44 ± 0.04·10 <sup>13</sup>                       | <b>1.5 ± 0.1·10<sup>14</sup></b>                  |

Table 3.1: Vertical distribution of NO<sub>3</sub> for both nights of analysis from 3:00-4:00 am

A pie chart for of the percentage contribution NO<sub>3</sub> for each atmospheric layer is shown in figure 3.8:

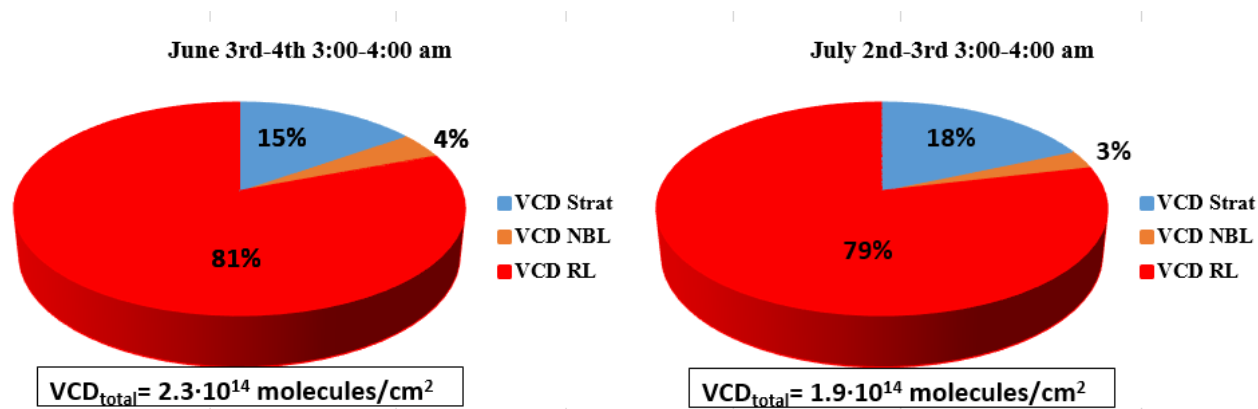


Figure 3.8: Pie charts showing vertical distribution of NO<sub>3</sub> for both nights of analysis from 3:00-4:00am

It can be seen that the majority of the NO<sub>3</sub> VCD for both nights is found to be in the residual layer during the calculated time (VCD<sub>RL</sub> > 50 %). As a result, it can be inferred that some degree of partitioning between the night-time boundary layer and residual layer is occurring, resulting in an abrupt shift in NO<sub>3</sub> abundance. Additionally, both high levels of O<sub>3</sub> present within the residual layer and the lack of ozone loss sources present due to nighttime inversion (surface NO emissions and ozone deposition chief among them) further increase the observed NO<sub>3</sub> abundance. The lack of surface NO emissions would also act to increase the NO<sub>3</sub> lifetime present within the residual layer, as shown by Brown et al. (2007). The findings of these experiments are noticeably larger than those calculated via data collected by Brown et al. (2007),

$VCD_{RL}$ :  $0.3-0.9 \cdot 10^{14}$  molecules/cm<sup>2</sup>, estimated from data therein (see Fig 1.4 in Introduction).

This may be due to differences between the two sites of measurement, both in terms of geography and month of collection (Brown data collected October 4<sup>th</sup>-5<sup>th</sup>, 2004). Due to the limited number of nights available for analysis, the evidence is by no means conclusive. However, the findings presented in this research are sufficient to indicate NO<sub>3</sub> mixing ratios taken along both light paths via active DOAS cannot explain the total NO<sub>3</sub> VCDs observed using lunar DOAS. This serves to indicate NO<sub>3</sub> abundance can display a great deal of variation over short vertical distances at night, and lends credence to previous findings that the majority of the total NO<sub>3</sub> Vertical column density for a given night being present within the residual layer.

### **3.5: NO<sub>3</sub> VCDs taken in March 2011**

A similar experiment in the determination of NO<sub>3</sub> column abundance using both active and lunar DOAS was performed on March 19<sup>th</sup>, 2011 (the night of the full moon) by Patryk Wojtal as part of his research. Integration times were varied between 100-250 ms with 2000 averages. The moonlight spectra were fit in the 657-671 fitting region by Patryk Wojtal using the same reference spectra as the two nights presented in the above research. The resulting NO<sub>3</sub> VCDs are shown below in figure 3.9:

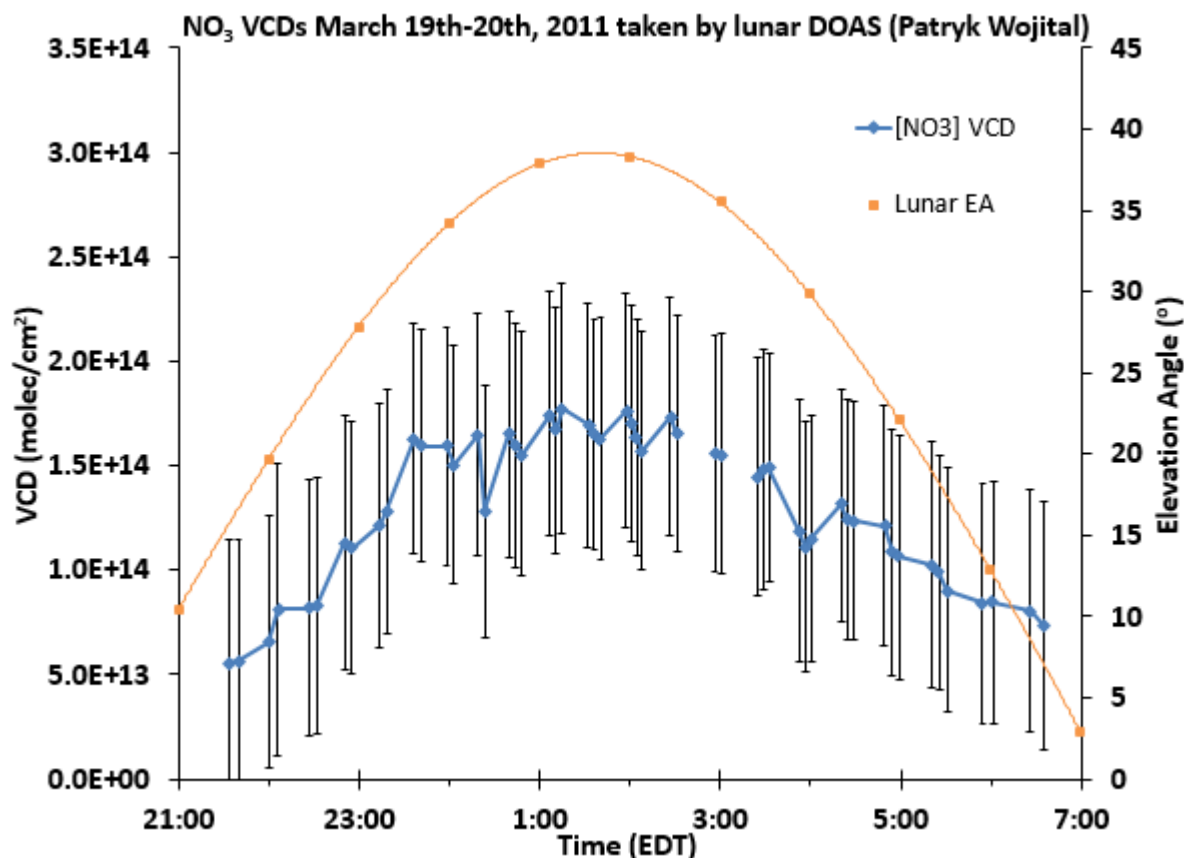


Figure 3.9: NO<sub>3</sub> VCDs collected on March 19<sup>th</sup> 2011. Sunrise occurs at 7:21 am

The results differ from trends found to occur in the NO<sub>3</sub> VCDs collected over the summer of 2015, with a gradual decrease in the early morning hours prior to sunrise (~7:00 am). The maximum NO<sub>3</sub> VCD was found to be  $1.8 \cdot 10^{14}$  molecules/cm<sup>2</sup>, slightly lower than those found in the present research. This could be attributed to seasonal differences, as in early spring, the lower temperatures would shift the equilibrium of NO<sub>3</sub> and N<sub>2</sub>O<sub>5</sub> to reduce observed NO<sub>3</sub> VCDs. Surface mixing ratios of NO<sub>3</sub> were also calculated by using the same 16m path height (Fig 3.5) as the current research (2.2 km return path). The results are shown in figure 3.10:

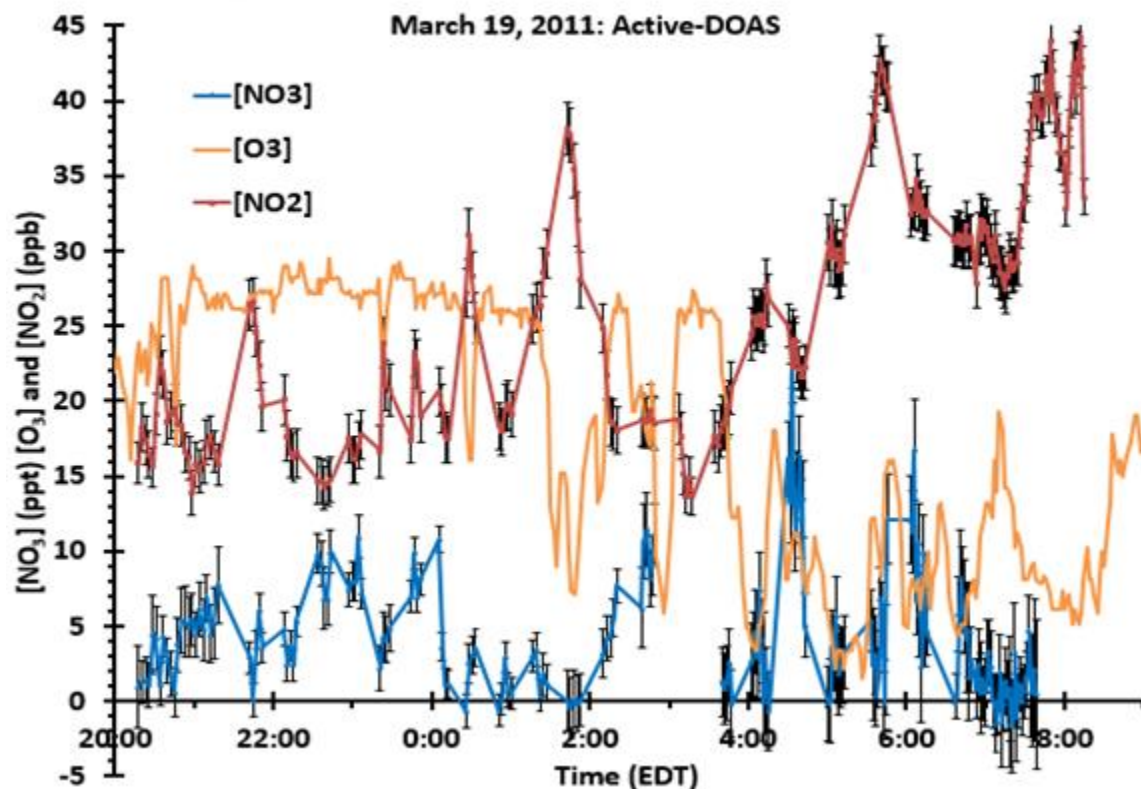


Figure 3.10: NO<sub>3</sub>, O<sub>3</sub>, and NO<sub>2</sub> mixing ratios collected using active DOAS March 19<sup>th</sup>/2011  
 Maximum NO<sub>3</sub> mixing ratios are observed to be 22 ppt at 4:30 am, shortly after a minor peak in O<sub>3</sub>. Increases in NO<sub>2</sub> during the night are found to correspond with decreases in ozone, and thus [NO<sub>3</sub>], which is expected due to reaction R 1.7. The vertical distribution of NO<sub>3</sub> of March 19<sup>th</sup> can thus be determined via equation E 3.1. Unlike the data collected during summer 2015, NO<sub>3</sub> VCDs were averaged from 3:40-4:40 am, as there is a gap in the collected NO<sub>3</sub> mixing ratios occurring at 3:00 am. The results are shown in Table 3.2:

|  | VCD <sub>Lunar</sub><br>(molecules/cm <sup>2</sup> ) | VCD <sub>Free trop.</sub><br>(molecules/cm <sup>2</sup> ) | VCD <sub>strat</sub><br>(molecules/cm <sup>2</sup> ) | VCD <sub>NBL</sub><br>(molecules/cm <sup>2</sup> ) | VCD <sub>RL</sub><br>(molecules/cm <sup>2</sup> ) |
|--|--|---|--|--|---|
| March 19 <sup>th</sup> -20 <sup>th</sup> | 1.2±0.1·10 <sup>14</sup>                             | 0   | 3.5 ± 0.5 ·10 <sup>13</sup>                          | 0.23 ± 0.002·10 <sup>13</sup>                      | <b>8.3±1·10<sup>13</sup></b>                      |

Table 3.2: Vertical distribution of NO<sub>3</sub> for March 19<sup>th</sup>, 2011 of from 3:40-4:40 am

The resulting pie chart for of the percentage contribution  $\text{NO}_3$  for each atmospheric layer is presented in Figure 3.11:

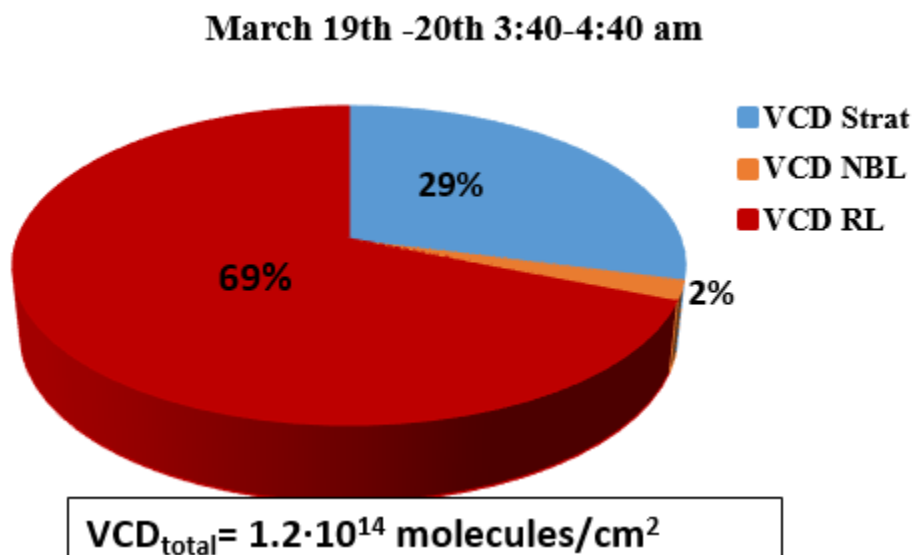


Figure 3.11: Pie chart showing vertical distribution of  $\text{NO}_3$  from 3:40-4:40am

The majority of the  $\text{NO}_3$  VCD is once again found to be in the residual layer lending further credence to the finding that the majority of the  $\text{NO}_3$  column abundance is located with the residual layer over the course of the night. However, further analysis would be necessary to cement this finding. As well, much like MAX-DOAS, interference in lunar DOAS by cloud cover was found to be a central hindrance to obtaining results with this method of combined analysis. Unlike MAX DOAS, maximum illumination of the reflected sunlight off the moon is found to occur over the course of a five day period centred on the full moon, placing greater importance upon having clear sky conditions during available nights of analysis. Attempting this analysis method in a mid-latitude area with a drier climate may allow the collection of a more consistent set of data using combined DOAS analysis, allowing comparison to  $\text{NO}_3$  VCDs

collected at both high latitudes (Wagner et al. 2000), and other urban environments (Chen et al. 2011).

# Chapter 4: HONO Measurement at AMS13 site

## 4.1: Measurement overview

HONO mixing ratios were determined from Aug 17<sup>th</sup> to Sept 4<sup>th</sup> using active DOAS during a joint field study over the summer of 2013 at the AMS13 site near Fort McMurray, Alberta. Spectral fitting was performed for NO<sub>2</sub> and SO<sub>2</sub> by Akshay Lobo, and HONO by Kevin Nikelski. Initial attempts to fit the entirety of the collected dataset identified that HONO mixing ratios decreased with time as the study progressed, eventually becoming negative when a single lamp spectra was used as the reference for the entire study. Clearly something was wrong and it alluded to the most probable problem being that the spectrum of the lamp was changing with time that somehow affected the retrieved HONO concentrations. Experimentation found significant variation in the retrieved HONO mixing ratios for a given sample spectra when different lamp spectrum, collected at different times during the study, were used as reference spectra in the fit scenario. Moreover, the retrieved concentration of HONO for a given sample spectra increased as lamp spectrum collected progressively later in the study were used in the fit scenario. This serves to suggest that there was a real change in time of the lamp spectrum. Investigation of the lamp spectra collected during the field study was performed in order test the hypothesis above that the lamp spectrum was changing with time and to develop a revised fitting scenario that would correct this drift.

## 4.2: Method Development of Two Lamp Fitting Scenario

In order to determine if the negative trend in HONO fit retrievals with time was due to the DOAS lamp source changing in time (i.e.; degrading), some additional fits were completed. To this end, a lamp spectrum collected on Aug 17<sup>th</sup> was fit successively using other lamp spectra collected during the study using the same method as the sample spectra. A HONO reference spectra was used in the fit regardless of the fact that the retrieved HONO should theoretically be zero in every case since the light in the “lamp” spectra has not transited through the atmosphere. Calibration spectra taken Aug 17<sup>th</sup> were used to minimize the possibility of the observed drift being due to a calibration error. The lamp spectra was then high-filtered (2000 iterations) and fit in the 337-361 nm range. The results are shown in Table 4.1:

| Night lamp spectra collected | HONO fit mixing ratio (ppb) | Chi-squared           |
|------------------------------|-----------------------------|-----------------------|
| Aug 17 <sup>th</sup>         | -0.010 ± 0.02               | 2.23·10 <sup>-6</sup> |
| Aug 19 <sup>th</sup>         | 1.1 ± 0.1                   | 7.44·10 <sup>-5</sup> |
| Aug 20 <sup>th</sup>         | 0.437±0.08                  | 4.75·10 <sup>-5</sup> |
| Aug 21 <sup>st</sup>         | 0.488±0.1                   | 1.55·10 <sup>-4</sup> |
| Aug 28 <sup>th</sup>         | 1.1±0.2                     | 2.51·10 <sup>-4</sup> |
| Sept 5 <sup>th</sup>         | 1.5±0.4                     | 9.85·10 <sup>-4</sup> |

Table 4.1: HONO fit concentrations and chi-squared values for when fitting the Aug 17<sup>th</sup> lamp spectra with other lamp spectra collected later in time

Table 4.1 indicates that the Chi-squared of the fit becomes progressively worse with progressively later lamp reference spectra and that simultaneous with this, the HONO fit coefficient and pseudo HONO mixing ratio, calculated using the 2.304 km path length gets progressively positive and statistically different from zero. This observed increase in both HONO fit concentration and chi squared is theorized to be due to a change in the DOAS lamp spectra over the course of the study, presumably with the formation of features within the lamp spectra that mimic HONO features. Fits performed using the DOASIS program are known to

display false output (positive or negative) when significant features present in the residual appear to be similar to a reference molecule being fit. In order to ensure that the development of the features present were primarily due to the lamp, the Aug 17<sup>th</sup> lamp spectrum was fit i) to a different Aug 17 lamp reference and ii) to the Sept 5<sup>th</sup> lamp reference. Both fits with the exclusion of HONO from the fit scenario, as shown in Figure 4.1:

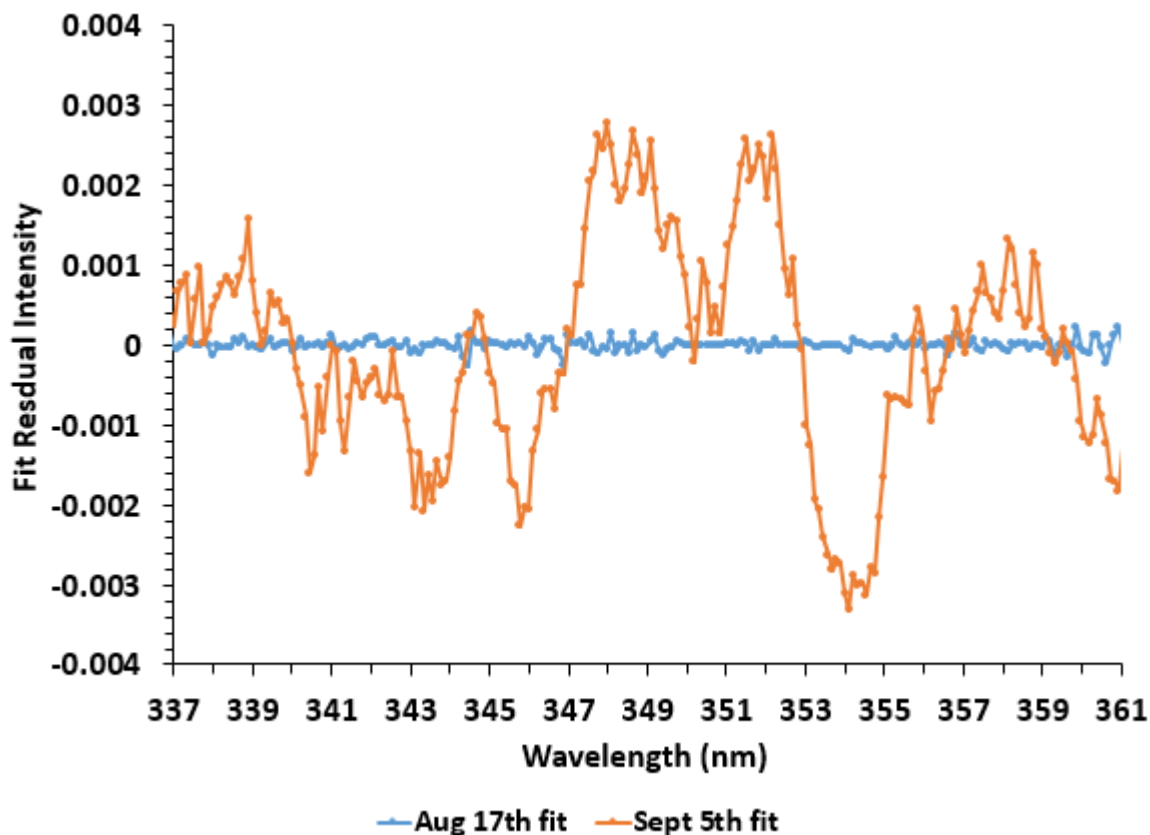


Figure 4.1: Fit residual for fitted lamp spectra collected on Aug 17<sup>th</sup> (blue) and Sept 5<sup>th</sup> (orange). Spectra were fit with a fit scenario containing a different Aug 17<sup>th</sup> lamp spectra in the 337-361 nm range excluding HONO from the fit.

It can be seen that significant features were found to be present in the Sept 5<sup>th</sup> fit even when HONO was excluded from the fit scenario, proving that the lamp spectra is changing with time. Attempting to offset this increasing lamp feature resulted in successively more negative HONO mixing ratios being determined through the sample HONO fits. Thus, the observed

features serve as an explanation for the original negative trend observed in the HONO mixing ratios with time.

It was theorized that the use of multiple lamp spectra in the fit scenario could eliminate the effects of the changing lamp features. By using reference lamp spectra that bracketed each sample spectrum in time, the lamp features that formed over time could be accounted for, resulting in a better fit residual and a more plausible HONO retrieval. In order to test this, median values of the nighttime lamp fit coefficients of sample spectra fit using a two lamp fitting scenario containing the Aug 28<sup>th</sup> lamp and the Sept 5<sup>th</sup> lamp were plotted using sample spectra from Aug 29<sup>th</sup> to Sept 5

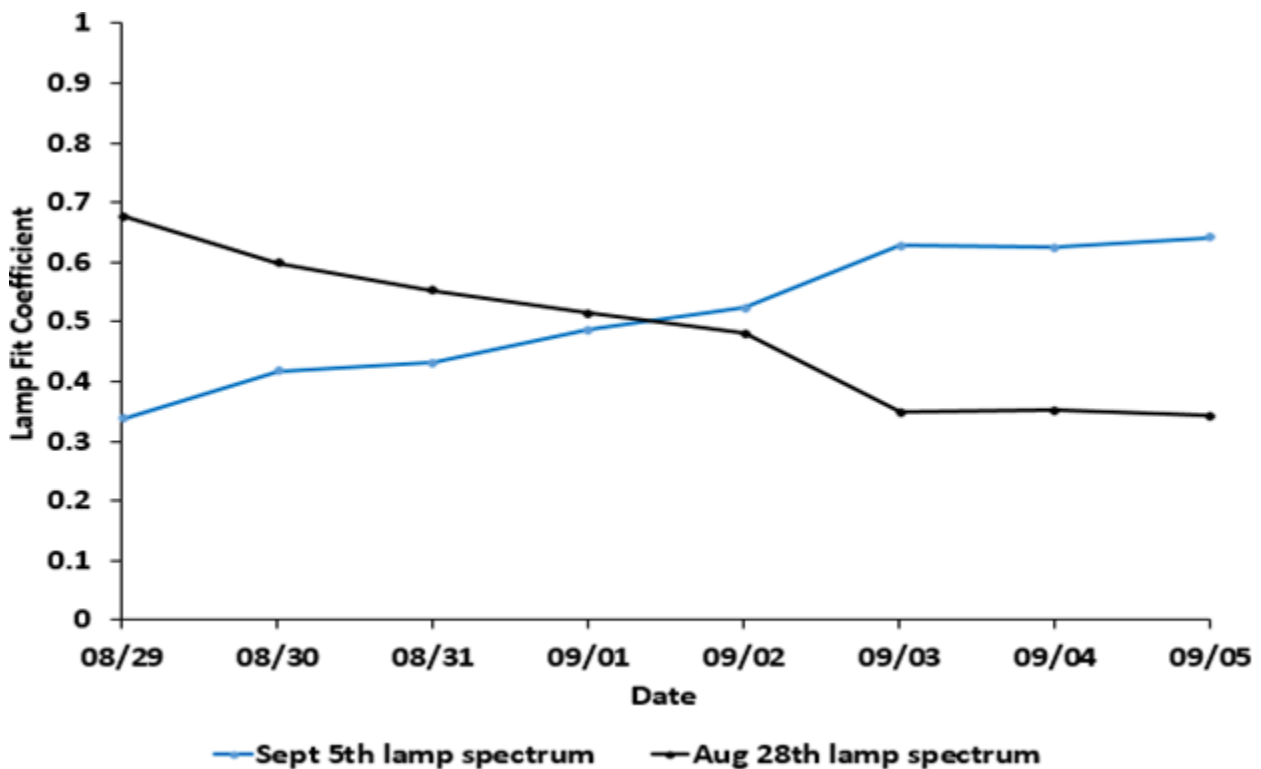


Fig 4.2: Median night-time lamp fit coefficients Aug 29th-Sept 5th

The lamp fit coefficient is shown to favor the most recent lamp spectrum taken in time. This allows the two-lamp fitting technique to be used even on days on which a lamp spectra was not taken, as it will favor the lamp collected on the analysis date. To demonstrate the effectiveness of the two lamp fit, the Sept 5<sup>th</sup> lamp spectrum was fit with a single fit scenario containing a lamp spectrum taken on Aug 17<sup>th</sup> to show the negative shift in HONO mixing ratios that occurs. The lamp was then fit with a two lamp fitting scenario containing the Aug 17<sup>th</sup> lamp spectrum and another lamp spectrum taken on Sept 5<sup>th</sup>. The results are shown in Table 4.2

| Lamp Spectrum used                                | HONO fit mixing ratio (ppb) | Chi-squared          |
|---|-----------------------------|----------------------|
| Aug 17 <sup>th</sup>                              | $-1.3 \pm 0.2$              | $4.25 \cdot 10^{-4}$ |
| Aug 17 <sup>th</sup> and Sept 5 <sup>th</sup> (b) | $0.02 \pm 0.05$             | $1.52 \cdot 10^{-5}$ |

Table 4.2: Comparison of one-lamp and two lamp fits using a lamp spectrum collected on Sept 5<sup>th</sup> (a)

The fit residuals are likewise presented in Figure 4.3:

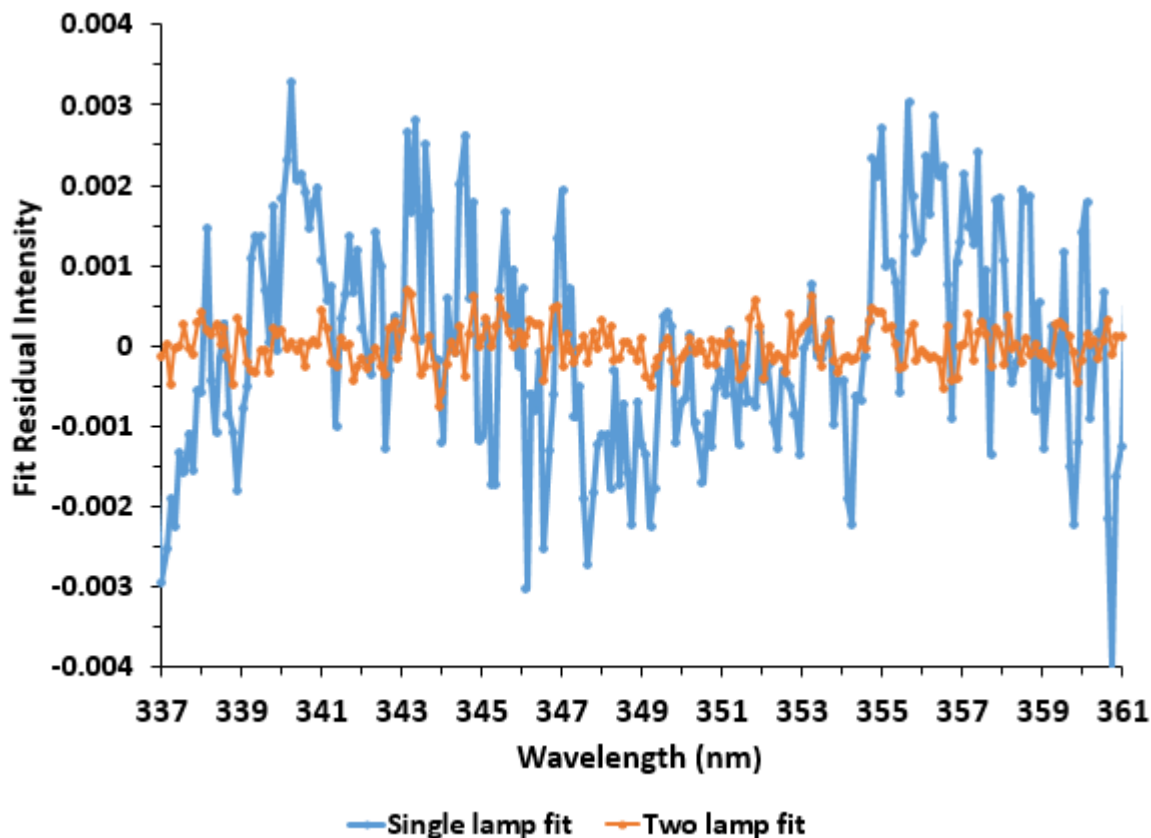


Figure 4.3: Fit residual for single and two lamp fits of Sept 5<sup>th</sup> lamp spectrum

The addition of the Sept 5<sup>th</sup> lamp was found to reduce both the negative HONO fit concentration observed in the single lamp fit, and the value of chi-squared. This serves as further indication that fitting the sample spectrum with the most recent lamp spectrum taken in time will reduce the observed artifact due to formation of new features within the lamp spectra. Further, it serves as indication that the use of a two-lamp fitting method is a successful procedure to correct the artifact produced by a lamp spectra that is changing in time. A potential problem with this theory is the fact that continuous running of the active DOAS system has previously been performed for HONO measurement at York University during work by Patryk Wojtala. The observed artifact of a changing lamp spectrum over time was not observed based on the DOASIS fits. We attribute this to the likely fact that in that work a single lamp was used for several years.

In the present work, a new lamp was installed in the DOAS telescope just prior to starting work at AMS 13. It is possible that any blackening or lamp deterioration is most significant within the first few hundred hours of lamp operation. The fact that there was significantly greater nighttime HONO mixing ratios were observed at York could also contribute to effect of this lamp artifact had in the AMS13 dataset.

### **4.3: HONO mixing ratios from Aug 17<sup>th</sup> - Sept 4<sup>th</sup>**

Day and night-time measurements of HONO mixing ratios were obtained through continuous running of the active DOAS instrument, pausing only to collect calibration, background and lamp spectra. High values of daytime HONO are observed early in the study (Aug 17<sup>th</sup>-23<sup>rd</sup>). These findings are presented in Figure 4.4:

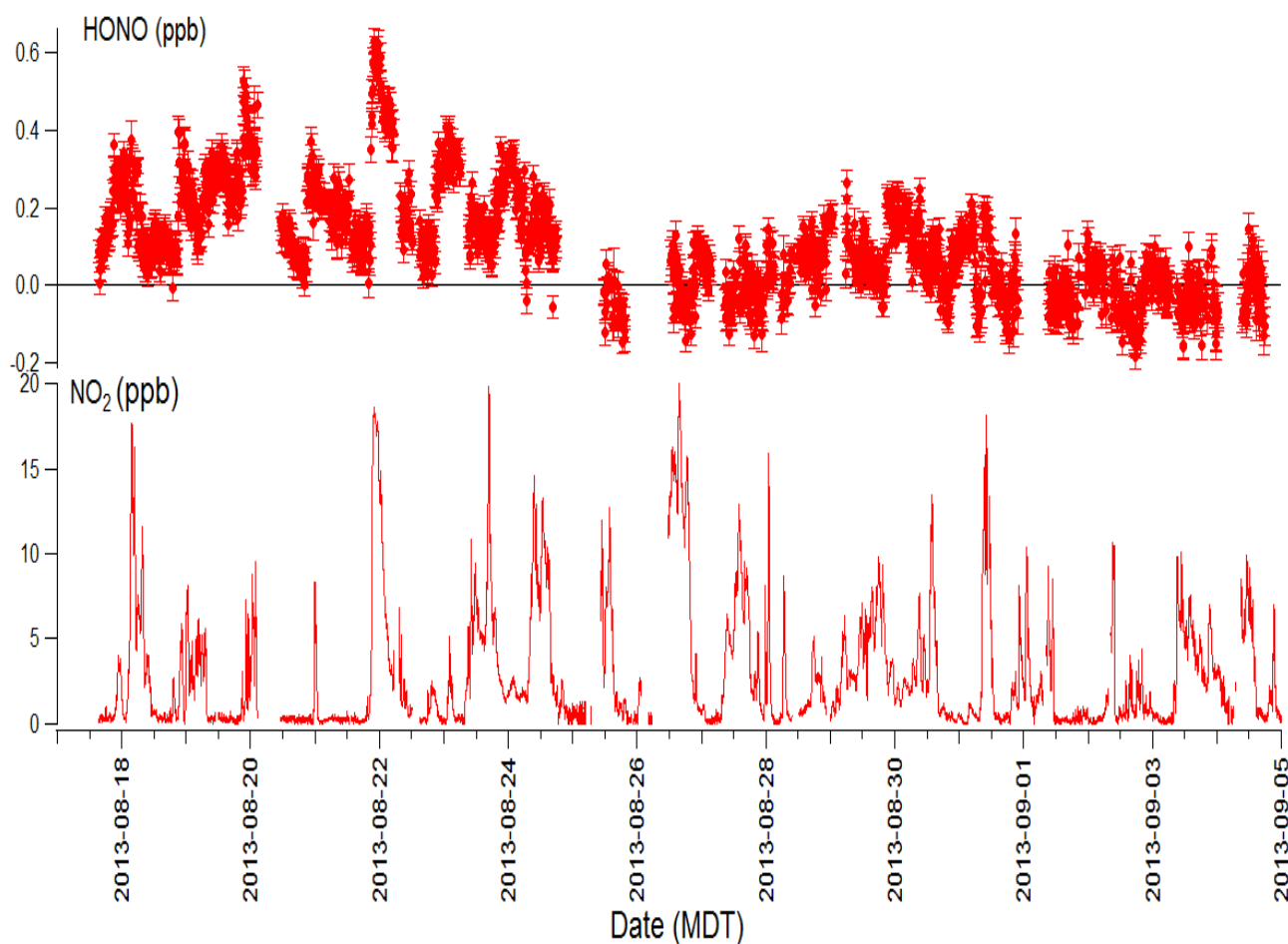


Figure 4.4: Measured HONO (10-minute averages) and NO<sub>2</sub> (2-minute averages) mixing ratios taken from Aug 17<sup>th</sup>-Sept 4<sup>th</sup>

Mixing ratios of HONO ranged from 0.0-0.64 ppb with a maximum value of 0.64 ppb on the night of Aug 21<sup>st</sup>. The resulting HONO maximum was found to occur at the same time as elevated levels in NO<sub>2</sub> mixing ratios, serving as an indication that the observed increase may have been due to a combustion event. A similar elevation in both HONO and NO<sub>2</sub> is observed on the morning of Aug 18<sup>th</sup>, with HONO concentration of 0.37 ppb being observed. All other instances of elevated NO<sub>2</sub> above 15 ppb during the study were found to occur either in the early morning, or afternoon. As such, focus was placed upon the 21<sup>st</sup> of August as a case study of the potential chemical and meteorological conditions necessary to observe elevated HONO during the summer in the forested region surrounding AMS13.

The wind direction on the night of Aug 21<sup>st</sup> was predominantly WSW Figure 4.5. This was confirmed through calculation of back trajectories using the NOAA Hysplit model (NOAA Air Resources Laboratory). The back trajectory suggested that the air did not pass through any of the main Suncor and Syncrude operations. This fact, coupled with the low wind speed found during the night of Aug 21<sup>st</sup> (0-1 m/s for most of the night) indicates that the observed elevation of NO<sub>2</sub> and HONO originated from an area near the site of analysis. Based on the back trajectory, it can be theorized that emissions originated from a region where in-situ mining is occurring, though further work would be necessary for confirmation.

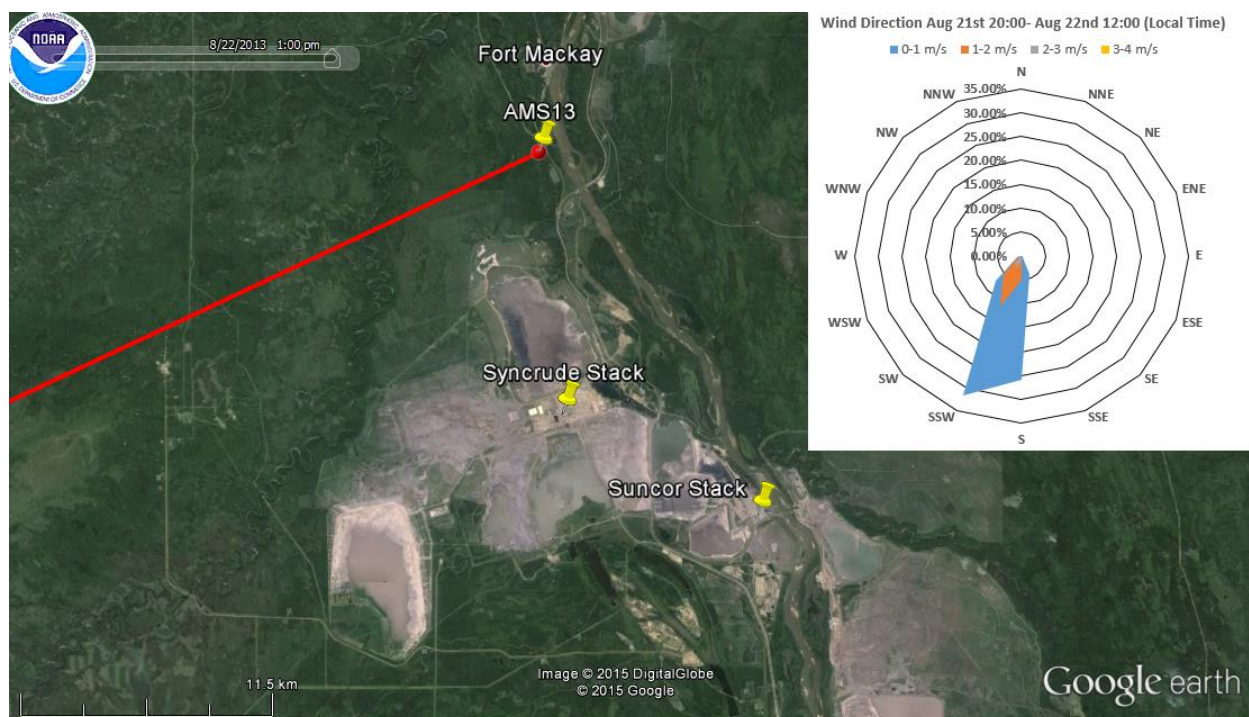


Figure 4.5: Calculated back trajectory of air mass at AMS13 site from 12:00 pm Aug 21<sup>st</sup> to 12:00 pm Aug 22<sup>nd</sup> local time (HYSPLIT model) Top Right: Wind direction and speed during NO<sub>2</sub> elevation on Aug 21<sup>st</sup>

Figure 4.6 shows atmospheric pollutants measured at the field site including HONO and NO<sub>2</sub>. There was no increase in the SO<sub>2</sub> mixing ratios at the time of HONO elevation on Aug 21<sup>st</sup>.

This serves as further indication that the wind direction on Aug 21<sup>st</sup> did not come from the main Syncrude and Suncor stacks. Thus, it seems likely that the elevation of both NO<sub>2</sub> and HONO seen to be present on this night are due to a surface source. Ozone is observed to undergo a rapid decrease on this night just after sunset, which is typical for this site. In respect to other trace gases in the atmosphere, CO<sub>2</sub> and methane were measured during the campaign, nighttime elevation due to biogenic contribution from the forested surroundings was observed on the night of Aug 21<sup>st</sup>, but does not correspond to the time of elevation observed for both HONO and NO<sub>2</sub> (10:00 pm). Finally, o-xylene mixing ratios, which can act as an indication of anthropogenic VOC emissions, and has sources from the tailings ponds present for Oil Sands production, and black carbon were measured at the AMS13 site. Both o-xylene and black carbon are seen to increase during the night due to the nighttime inversion of the PBL, but have no observed spike at the time of HONO and NO<sub>2</sub> elevation, and the mixing ratios of o-xylene are extremely low (~ 10 ppt). Thus it is difficult to identify the source of the NO<sub>x</sub> (and thus HONO) that impacts the site on this night. The resulting mixing ratios can be observed in figure 4.6:

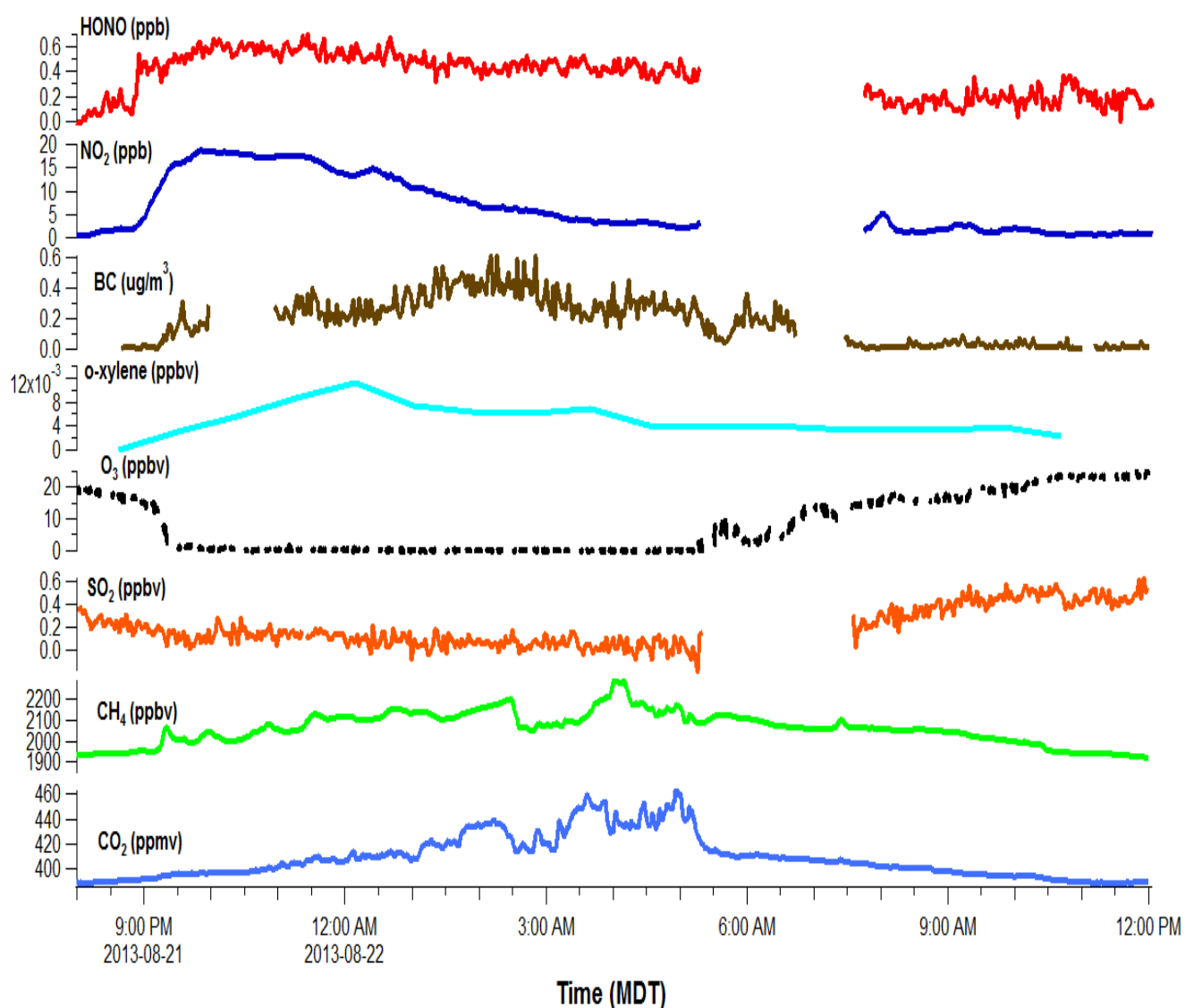


Figure 4.6: Concentration of various atmospheric species from 8:00pm Aug 21<sup>st</sup> to 12:00pm Aug 22<sup>nd</sup>

The HONO/NO<sub>2</sub> ratio (Fig 4.7) shows a small spike early in the evening (0.02-0.19). The ratio is then observed to settle to a constant value of ~ 3.0% that slowly increases over the course of the night, to a value of ~ 15%. A similar trend was observed in nocturnal measurements of HONO in a polluted marine boundary layer (Wojtala et al. 2011) and is used to suggest a common method of HONO formation on both terrestrial and aqueous surfaces due to

NO<sub>2</sub> hydrolysis (Finlayson-Pitts et al., 2003). In the paper by Wojtal et al. (2011), the observed increase in the HONO/NO<sub>2</sub> ratio was found to be due to HONO being in steady state, while NO<sub>2</sub> was lost to other processes over the course of the night.

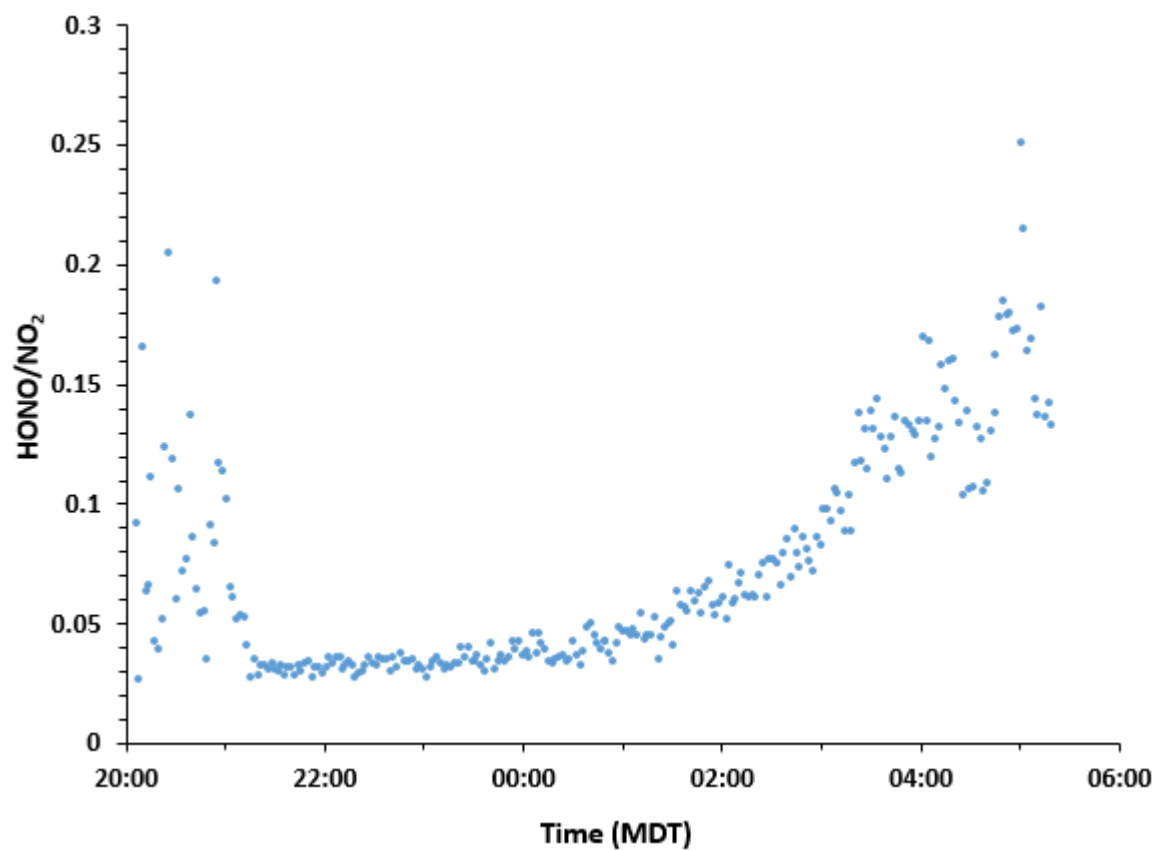


Figure 4.7: HONO/NO<sub>2</sub> ratio for Aug 21st night

### 4.4: Diurnal profile of HONO at AMS13

An average diurnal profile of HONO was calculated for the whole study, using 15-minute time bins for all measurement days. The results can be seen in Figure 4.8:

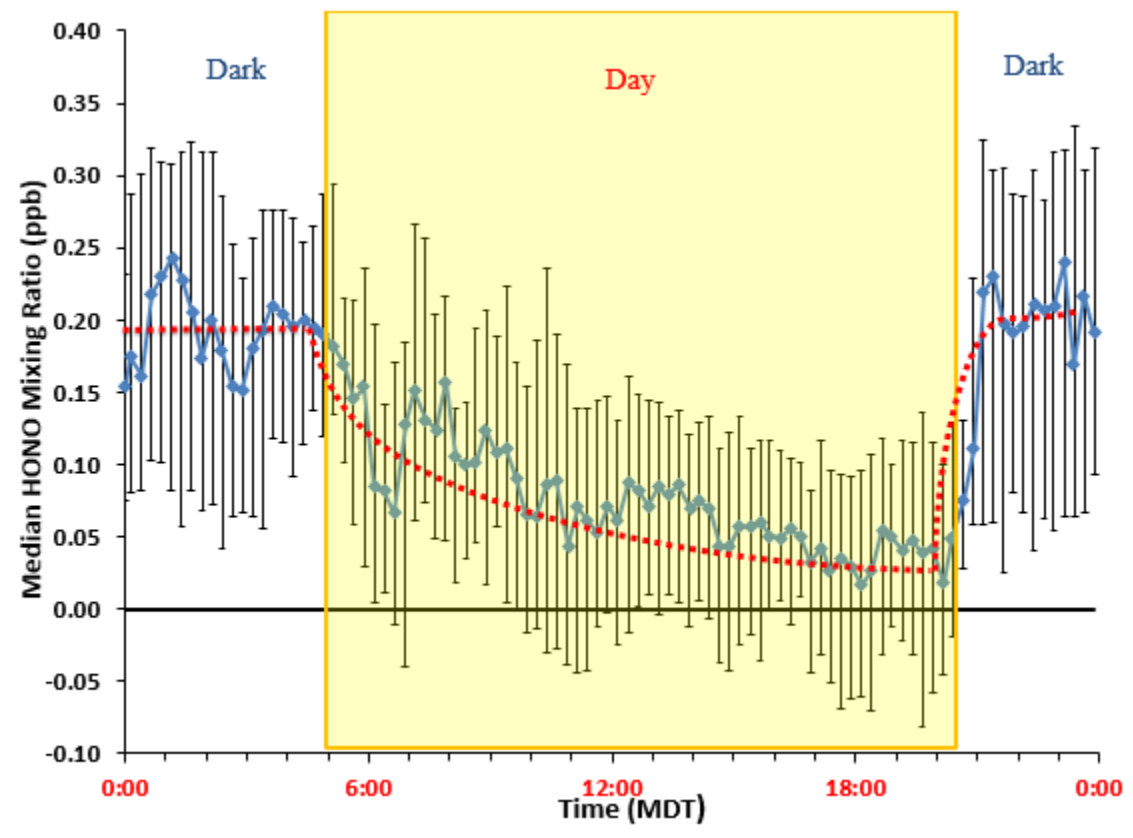


Figure 4.8: Diurnal HONO profile at AMS13 Aug 17<sup>th</sup>-Sept 4<sup>th</sup>. Error bars were calculated from the upper and lower limits of the HONO mixing ratios based on the 25<sup>th</sup> and 75<sup>th</sup> percentile

Profiles of diurnal  $\text{NO}_2$  and the  $\text{HONO}/\text{NO}_2$  mixing ratio were likewise produced:

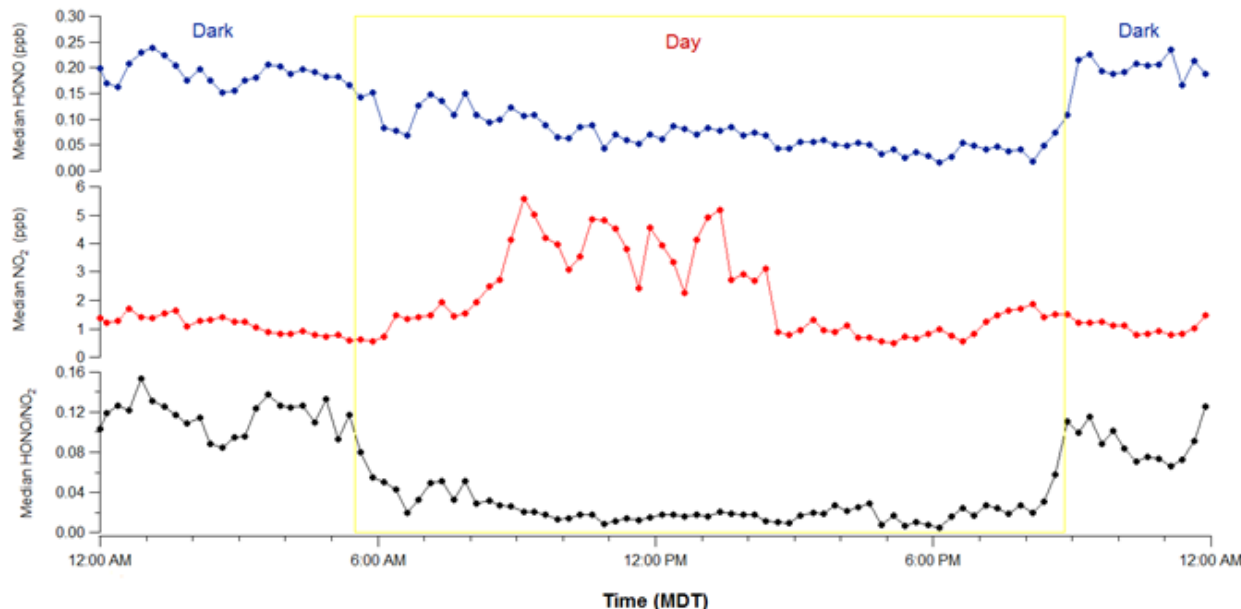


Figure 4.9: Diurnal HONO,  $\text{NO}_2$  and  $\text{HONO}/\text{NO}_2$  Ratio profiles from Aug 17th-Sept 4th

It can be seen from figure 4.8 that HONO profile has higher mixing ratios at night, before decreasing due to the rapid photolysis of HONO during daylight hours. HONO mixing ratios increased rapidly after sunset (~8:50 pm). Median  $\text{NO}_2$  levels during the night (Fig 4.9) were observed to be low, with the exception of the night of Aug 21<sup>st</sup> previously discussed. This is primarily due to the reduction of  $\text{NO}_2$  emission near AMS13 due to reduced facility emissions, as well as limited mixing of elevated plumes under stable nighttime conditions. Other sources may still have contributed, as evidenced by elevated levels seen during the night in some instances. In particular, the open pit mining operations present at both Syncrude and Suncor could act as a source of  $\text{NO}_x$  during the night. Daytime  $\text{NO}_2$  levels were found to be higher, with maximum values found to be 5 ppb at ~9:00 am. This increase represents the reformation of a well-mixed PBL, and increased emission from ground sources present during work hours. A rapid decrease is then observed in the afternoon (3:00 pm), followed by a small increase beginning at 6:00pm,

most likely the onset of the formation of a nocturnal boundary layer. Variation in  $\text{NO}_2$  mixing ratios was found to be high, with afternoon mixing ratios ranging from 0.5-13 ppb on different days, likely dependent on wind direction and the periodic mixing of elevated plume emissions from upgrader plumes to the surface. However, the  $\text{NO}_2$  mixing ratios measured during the study were still found to be lower overall than those seen in previous field studies performed in an urban environment (Elshorbany et al. 2012). This, in turn, could act to reduce the HONO mixing ratios present at the site. Finally, daytime levels of HONO are seen to be higher than anticipated, with noontime values of ~80 ppt measured. A reduced rate of HONO photolysis due the forest canopy at the site may cause the high daytime values of HONO, or alternatively, the high HONO level could be caused by emissions from a nocturnally deposited surface reservoir (Wojital et al. 2011, Vandenkoer et al. 2013). In order to determine if either of these two possibilities is indeed the case, theoretical daytime HONO mixing ratios using the photostationary state (PSS) approach were determined and compared to actual HONO mixing ratios.

#### **4.5: Determination of daytime levels and radical production rates of HONO**

Estimation of  $[\text{HONO}]_{\text{PSS}}$  during the field study is accomplished through use of equation E1.5 under the assumption that  $d[\text{HONO}]/dt \sim 0$ . The values of  $j_{\text{HONO}}$  during the study determined at the AMS13 site by the Osthoff group are shown in figure 4.10:

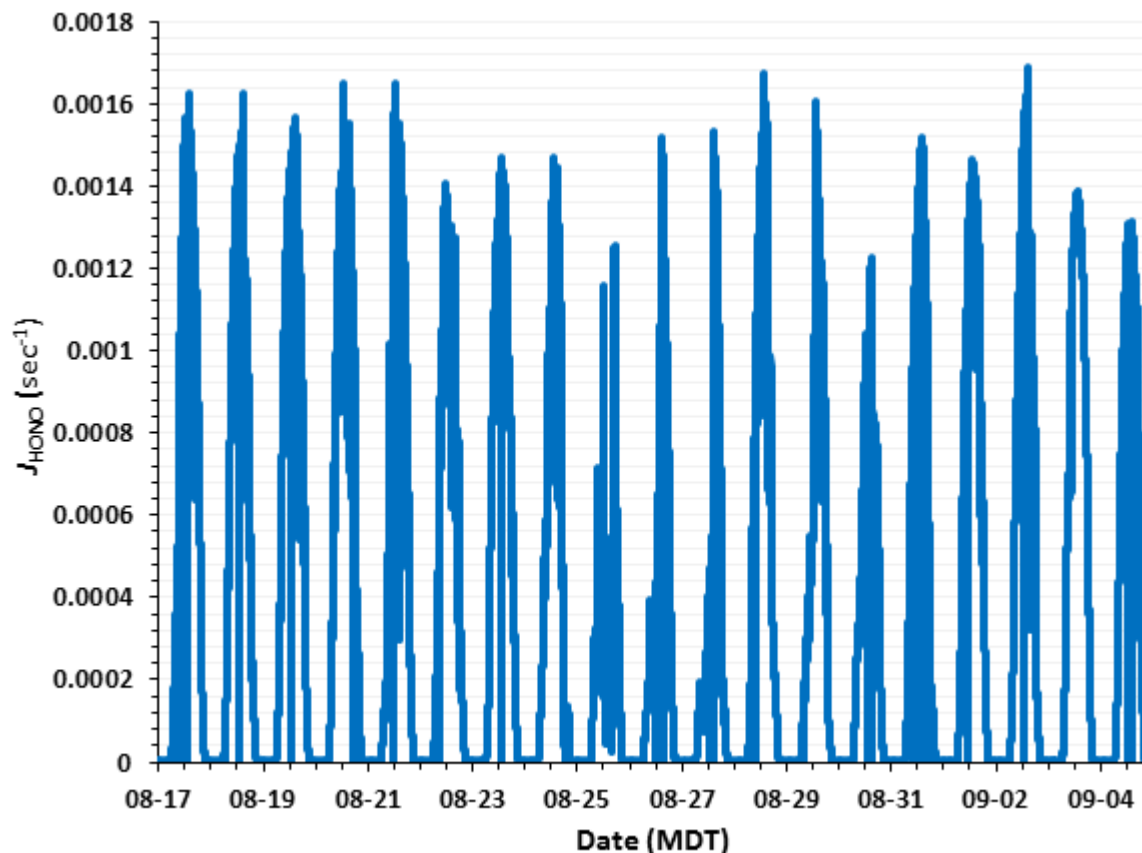


Figure 4.10:  $j_{\text{HONO}}$  Values at the AMS13 site from Aug 17th-Sept 4th

Maximum values were found to be roughly  $0.00166 \text{ sec}^{-1}$  during the early afternoon, corresponding to a HONO life-time of 602 seconds (10 minutes), consistent with previous measurements (Spataro et al. 2014). NO and NO<sub>y</sub> data was likewise collected at the AMS13 by the Osthoff group through use of chemiluminescence. Although OH levels were not measured at AMS13 during the study, afternoon OH concentrations were estimated to be between  $1\text{-}3 \cdot 10^7$  molecules·cm<sup>-3</sup> on select days (Hayden et al., 2015) using aircraft VOC measurements and their photochemical degradation downwind via the method presented in Kleinman et al. (2003). Using the temperature dependence of reaction 1.30 and 1.31, and the average temperature between 12:00 and 1:00 pm, the values of the rate constants used in this analysis were  $k_{(\text{HONO}+\text{OH})} = 6.0 \cdot 10^{-12} \text{ cm}^3 \cdot \text{molecule}^{-1} \cdot \text{sec}^{-1}$  and  $k_{(\text{NO}+\text{OH})} = 8.5 \cdot 10^{-12} \text{ cm}^3 \cdot \text{molecule}^{-1} \cdot \text{sec}^{-1}$  (Atkinson et al. 2004).

Based on these parameters, [HONO]<sub>PSS</sub> values from Aug 17<sup>th</sup>-Sept 4<sup>th</sup> were calculated using various assumptions of [OH] and the value of *j*HONO. An important distinction for the calculation of photo-stationary state is the assumption that the reaction of NO and the OH radical acts as the only specified pathway of HONO production. The possibility of deposition of HONO to the surface, direct HONO emissions from pollutant sources or other sources are not included in the assumption, and production via reaction R 1.31. The potential of a locally reduced photolysis rate of HONO close to the DOAS beam path in the forest was simulated by reducing values of *J*HONO by a factor of 2 and 3 as a sensitivity estimate. Calculation of [HONO] during daytime hours was performed during time periods when the AMS13 site was not impacted by plume events (NO < 1ppbv). This is due to the resulting influx of NO, and thus HONO from a different pathway than presented in equation E 1.5 breaking the PSS assumption. Data collected from Aug 17<sup>th</sup>-22<sup>nd</sup>, Aug 28<sup>th</sup>, and Sept 1<sup>st</sup> were used in the PSS determination from 12:00-1:00 pm. The values of [HONO]<sub>PSS</sub> calculated under the various assumptions, as well as the measured values are shown in Table 4.1:

| Average HONO mixing ratio (ppt) | [HONO] <sub>PSS</sub> (1.0·10 <sup>7</sup> OH) ppt | [HONO] <sub>PSS</sub> (3.0·10 <sup>7</sup> OH) ppt | [HONO] <sub>PSS</sub> (1.0·10 <sup>7</sup> OH) ppt ( <i>j</i> HONO/2) | [HONO] <sub>PSS</sub> (3.0·10 <sup>7</sup> OH) ppt ( <i>j</i> HONO/2) | [HONO] <sub>PSS</sub> (1.0·10 <sup>7</sup> OH) ppt ( <i>j</i> HONO/3) | [HONO] <sub>PSS</sub> (3.0·10 <sup>7</sup> OH) ppt ( <i>j</i> HONO/3) |
|---------------------------------|--|--|---|---|---|---|
|                                 | 5.5  | 15.0   | 10.4  | 26.5  | 15.0  | 35.7  |
| Measured HONO                   | <b>133 ppt</b>                                     |  |   |   |   |   |

Table 4.3: Comparison of average [HONO]<sub>PSS</sub> mixing ratios calculated using the PSS assumption (equation E 1.5) with measured values from 12:00pm-1:00pm

The measured HONO mixing ratios are observed to be much higher (133 ppt on average) than the calculated values of HONO PSS [5-36ppt] for the various assumptions. The measured results were found to be consistent with daytime mixing ratios previously observed in other

summer field campaigns (Michoud et al. 100-300 ppt). These results indicate that in this environment, as in other areas, there appears to be a daytime HONO source ( $P_{\text{unknown}}$ ) that is not being taken into account by the PSS assumption. There are many possible identities to this daytime source. Reduced photolysis of HONO during daylight hours acting as a reduced HONO sink due to the surrounding forest canopy present along the light path can be ruled out as a possibility due to the inclusion of reduced photolysis scenarios in the calculation of  $[\text{HONO}]_{\text{PSS}}$ . It can be seen that, even at 67% reduction of  $j\text{HONO}$ , the measured values are still considerably larger than those calculated using the photo-stationary state assumption.

Adsorbed  $\text{HNO}_3$  and nitrate ( $\text{NO}_3^-$ ) has been found to undergo photolysis at ultraviolet wavelengths ( $\sim 300\text{nm}$ ), which act to produce HONO (Zhou et al. 2011):



Given the abundance of surface area present in a forested setting, as well as Reaction 1.33 serving as the primary formation pathway for nocturnal HONO, the photolysis of  $\text{HNO}_3$  could help elevated daytime HONO levels observed during the field study. Soil emission (Siu et al, 2011) is a second possibility as is the release of HONO from surface reservoirs following surface deposition (Wojtala et al. 2011, Vandenboer et al. 2014).

#### **4.6: Importance of HONO as an OH source**

Based on the measured photolysis rate constants for HONO and the diurnal profile of HONO, the OH radical production rate due to HONO photolysis was calculated at ground level. These results are compared to OH production from the photolysis of  $\text{O}_3$  through reactions R 1.5 and R 1.6, calculated from measured photolysis rate constants ( $J_{\text{O}_3}$ ) and ozone mixing ratios (Osthoff personal data set). The concentration of water vapor present was calculated based on

the relative humidity and temperature at the AMS13 site, and the rate constant of the reaction of O(<sup>1</sup>D) with H<sub>2</sub>O was  $k_{(O(1D)+H_2O)} = 2.2 \cdot 10^{-10} \text{ cm}^3 \cdot \text{molecule}^{-1} \cdot \text{sec}^{-1}$  (Atkinson et al. 2004). The quenching of O(<sup>1</sup>D) → O(<sup>3</sup>P) by N<sub>2</sub> ( $k_{(O(1D)+N_2)} = 2.6 \cdot 10^{-11} \text{ cm}^3 \cdot \text{molecule}^{-1} \cdot \text{sec}^{-1}$ ) and O<sub>2</sub> ( $k_{(O(1D)+O_2)} = 4.0 \cdot 10^{-11} \text{ cm}^3 \cdot \text{molecule}^{-1} \cdot \text{sec}^{-1}$ ) was factored into the calculation of OH production, shown in equation E 4.1:

$$P_{OH(\text{ozone})} = 2 \cdot j_{O_3} [O_3] \cdot \frac{k_{(O(1D)+H_2O)} \cdot [H_2O]}{k_{(O(1D)+H_2O)} \cdot [H_2O] + k_{(O(1D)+N_2)} \cdot [N_2] + k_{(O(1D)+O_2)} \cdot [O_2]} \quad (\text{E 4.1})$$

The photolysis of formaldehyde is also known to contribute to production of OH, based on reaction R 4.2 and R 4.3:



A second photo-decomposition pathway for formaldehyde also occurs, yielding H<sub>2</sub> and CO. This pathway does not produce HO<sub>2</sub>, and thus does not directly contribute to OH radical production. Since HO<sub>2</sub> is known to undergo rapid reaction with NO to produce OH, it represents a potentially significant source during daylight hours:



The yield of HO<sub>2</sub>, and thus OH, was calculated based on measured HCHO mixing ratios (Wheeler, personal dataset) and J values (Osthoff et al., collected AMS13 data). The productions rates of OH from all three sources are displayed in figure 4.11:

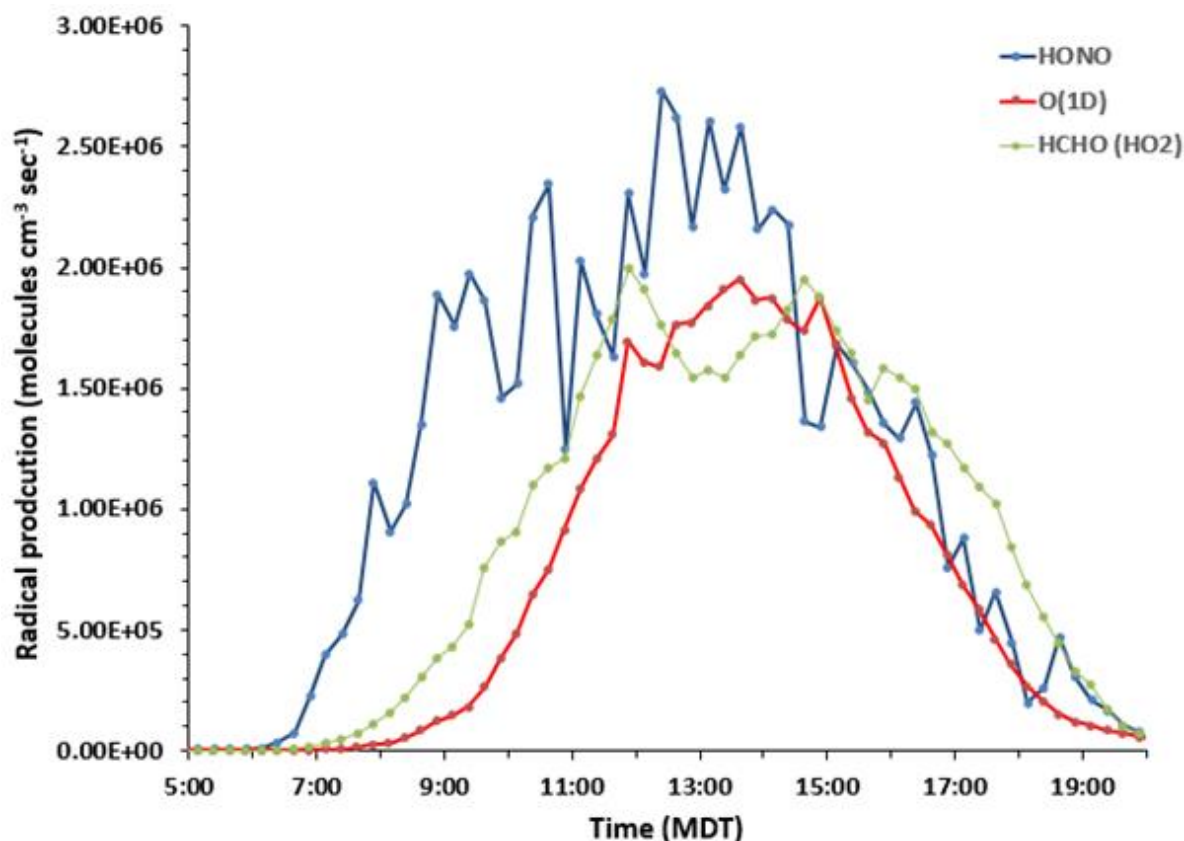


Figure 4.11: Comparison of OH production from HONO photolysis, reaction of O(<sup>1</sup>D) with water and HCHO photolysis at the AMS13 site

All three sources of OH included here have similar maximum OH production rates (2-2.5·10<sup>6</sup> molecules·cm<sup>-3</sup>·sec<sup>-1</sup>) although they differ in their timing and duration. The total OH radical production can be calculated by integrating the production rate with respect to time throughout the day. Based on these results, the photolysis of HONO is found to be the dominant source of radicals during the day, particularly in the early morning. Photolysis of HONO is found to contribute roughly 83% of total radical production from 6:00-9:00 am, vastly exceeding contributions from both the reaction of O(<sup>1</sup>D) and the photolysis of formaldehyde at this time. This is most likely due to accumulation of HONO over the course of the night, which then acts as an OH reservoir subsequent to sunrise. The contribution of HONO to radical production is then found to decrease in the early afternoon with increasing O<sub>3</sub> and HCHO levels. As the afternoon

progresses, the contribution of HONO to radical production decreases leaving the photolysis of formaldehyde as the primary source of OH at ~15:00. However, HONO photolysis is still found to be the dominant source of radical production over the full day (42 %). This low production of OH from O<sub>3</sub> photolysis was somewhat surprising and different than seen in other studies in more southerly locations (the CALNEX study for example, Young et al. 2012, Stutz et al. 2014). This is likely the combined results of low O<sub>3</sub> mixing ratios at the AMS13 site, the low values of J<sub>O(1D)</sub> due to the northerly location of the site (57° latitude) and the presence of sufficient ambient HONO mixing ratios during daylight hours. Figure 4.12 shows the variation in radical production observed both over the course of the day and during the early morning, based on fractional radical production by each source:

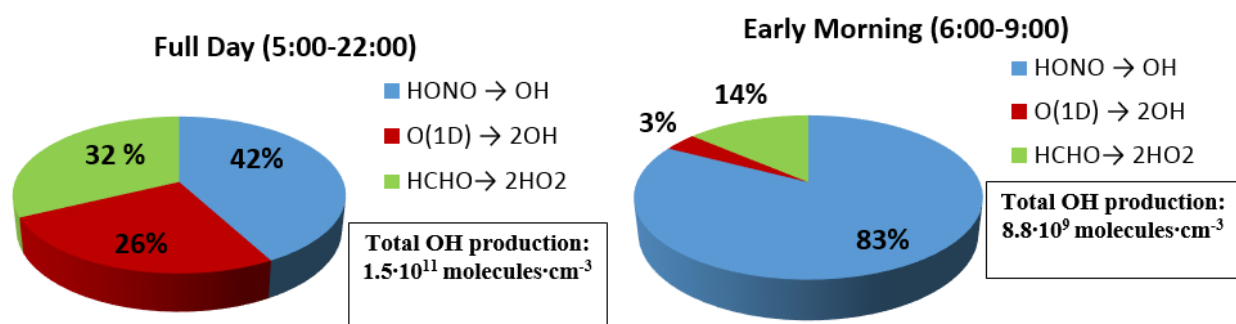


Figure 4.12: Pie charts showing the relative importance of primary radical sources during the full day (left) and the early morning (right)

The lack of inclusion of other sources of OH radical production, such as the reaction of ozone with alkenes, and the photolysis of hydrogen peroxide (H<sub>2</sub>O<sub>2</sub>) and ROOH, is primarily due to a lack of collected data for these species. Inclusion of these radical sources would act reduce the relative importance of HONO as a ground level OH source, but would likely not change the conclusion that HONO appears to be the dominant ground level OH source. In the current iteration, the values of P<sub>OH</sub> determined for HONO in the early morning are found to be similar to

measurements taken during the CalNex study (Young et al. 2012,  $2.0 \cdot 10^6$  molecules $\cdot$ cm $^{-3}$  $\cdot$ sec $^{-1}$ ). Contribution by ozone was found to be much lower than that observed in the CalNex study (maximum  $13 \cdot 10^6$  molecules $\cdot$ cm $^{-3}$  $\cdot$ sec $^{-1}$  at ground level), both due to the higher latitude of the measurement site, differences in emission levels between a populated urban area and the forested region surrounding the AMS13 site. Comparison between primary radical source strength with results taken during the Unitah Basin Winter Ozone study performed during the winter of 2011-2012 (Edwards et al. 2013), found similar findings to those found at AMS13, with HONO photolysis exceeding radical production by the reaction of O( $^1$ D) with water, though overall values for both were found to be lower in comparison to the ASM13 measurements. Based on the above results however, it can be seen that a daytime HONO source appears to be present in the forested region surrounding the Alberta Oil Sands, and serves as a dominant source of daytime radical production at surface level.

## 4.7: Comparison of forested and urban HONO mixing ratios

A summary table of both day and nighttime mixing ratios for both HONO and NO<sub>2</sub> is presented in

Table 4.4:

|                              | NO <sub>2</sub> (ppb) |             | HONO (ppb)    |               |
|------------------------------|-----------------------|-------------|---------------|---------------|
|                              | Daytime               | Nighttime   | Daytime       | Nighttime     |
| <b>90<sup>th</sup> perc.</b> | <b>11.59</b>          | <b>6.80</b> | <b>0.22</b>   | <b>0.40</b>   |
| <b>Mean</b>                  | <b>4.50</b>           | <b>2.22</b> | <b>0.077</b>  | <b>0.20</b>   |
| <b>Median</b>                | <b>5.48</b>           | <b>1.07</b> | <b>0.091</b>  | <b>0.19</b>   |
| <b>10<sup>th</sup> perc.</b> | <b>0.24</b>           | <b>0.13</b> | <b>-0.069</b> | <b>0.0042</b> |

Table 4.4: Summary Table of HONO and NO<sub>2</sub> mixing ratios from Aug 17<sup>th</sup>-Sept 4<sup>th</sup> of the AMS13 field study. Nighttime mixing ratios were taken from 10:00pm-5:00pm, while daytime values are from 12:00pm-2:00pm

The median values of NO<sub>2</sub> during the study were, despite peak mixing ratios up to 18 ppb, low overall. This in turn explains the low HONO mixing ratios seen at night, as NO<sub>2</sub> is the primary precursor for HONO production (R 1.32). The fact that peak NO<sub>2</sub> values observed during the field study occurred during daylight hours, with the exception of those seen on Aug 21<sup>st</sup>, lends further credence to this finding. The median daytime HONO mixing ratios were found to be consistent with other field campaigns (Spataro et al., 2013, Michoud et al., 2014, Sörgel et al, 2011), indicating consistency with the observation of an unknown daytime HONO source not accounted for by the reactions included in the photostationary state assumption. Comparison of the median nighttime levels of both NO<sub>2</sub> and HONO in the forested region near AMS13 and

those taken during a year-long dataset collected at York University (Wojital, 2013) is presented in Table 4.3:

| <b>Site of Analysis</b> | <b>Median NO<sub>2</sub> (ppb)</b> | <b>Median HONO (ppb)</b> |
|-------------------------|------------------------------------|--------------------------|
| <b>Site near AMS13</b>  | <b>1.07</b>                        | <b>0.20</b>              |
| <b>York University</b>  | <b>15.76</b>                       | <b>1.02</b>              |

Table 4.5: Comparison of median nighttime NO<sub>2</sub> and HONO mixing ratios taken both in a forested (AMS13) and urban (York University) setting

During the measurements at York, higher HONO and NO<sub>2</sub> mixing ratios were found during nights with low wind speeds and high values of  $\Delta T_{9.5-1.0}$ , which served as an indication of a stable nocturnal inversion. These conditions are similar to those seen on Aug 21<sup>st</sup>, but the resulting HONO mixing ratios are found to be considerably smaller in the Oil Sands. This indicates that the difference in NO<sub>2</sub> levels between the two settings is the primary reason for the observed difference in HONO mixing ratios. Replication of these experiments during the winter months would be beneficial in the determination of the annual ground level HONO profile present in the region surrounding the Oil Sands, especially since it is known that wintertime NO<sub>2</sub> levels are much higher than summer levels in the Oil Sands Region (unpublished data, WBEA).. However, it has been found that nighttime levels of both NO<sub>2</sub> and HONO are low in the forests surrounding Oil Sands processing. Daytime HONO levels were found to be higher than anticipated based on the PSS assumption, and are comparable to daytime HONO levels seen during other field studies, though much lower than those seen in polluted urban areas. Figure 4.12 shows a summary of observed HONO mixing ratios and calculated unknown daytime HONO sources, including those found at the AMS13 field study:

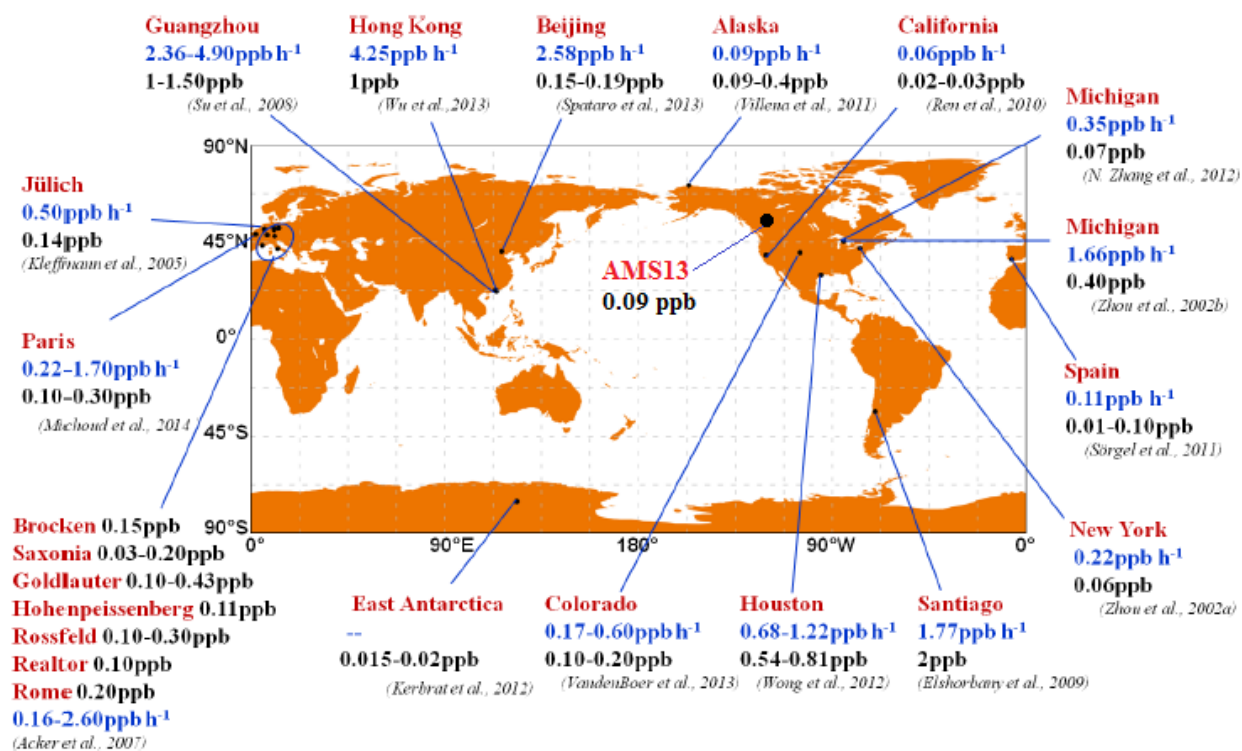


Figure 4.13: Summary of observed HONO mixing ratios at noon (black) and calculated unknown daytime HONO sources (blue), including findings taken during the AMS13 field study. Source: Tang et al. 2015

## Chapter 5: Conclusions and Future Work

### NO<sub>3</sub> at York University:

The vertical distribution of NO<sub>3</sub> at night is highly influenced by atmospheric stability, proximity to anthropogenic NO<sub>x</sub> sources, transport and the previous day's chemistry, a remnant of which can reside in the residual layer of the atmosphere. Measurements of NO<sub>3</sub> were made during two nights (June 3<sup>rd</sup> and July 2<sup>nd</sup>) in the summer of 2015, both as overall VCDs and mixing ratios in the nocturnal boundary layer. It was found that surface mixing ratios were insufficient to account for the NO<sub>3</sub> VCDs present on both nights of analysis (ranging from  $1.0\text{-}2.4\cdot 10^{14}$  molecules·cm<sup>-2</sup>). The stratospheric component of the overall NO<sub>3</sub> column was determined to be in the range of  $3.5\text{-}4.0\cdot 10^{13}$  molecules /cm<sup>2</sup> at the latitude of measurement, estimated from literature values and thus also insufficient to account for measured values. By constraining the amount of NO<sub>3</sub> present in the stratosphere based on literature, and constraining the amount of NO<sub>3</sub> in the NBL based on the measurements, we find that ~70-80% of the VCD is attributable to NO<sub>3</sub> present in the residual layer, with VCD<sub>RL</sub> of  $1.9\pm 0.1\cdot 10^{14}$  molecules/cm<sup>2</sup> for June 3<sup>rd</sup>-4<sup>th</sup> (81%) and  $1.5 \pm 0.1\cdot 10^{14}$  molecules/cm<sup>2</sup> for July 2<sup>nd</sup>-3<sup>rd</sup> (79%) being observed from 3:00-4:00 am. These results are much higher than those typically seen in the NBL and indicate that there is the potential that significant oxidation chemistry via the NO<sub>3</sub> radical can be occurring in the residual layer. The small number of nights of analysis for this study serves to limit these findings, however. The limitation on data collection for the lunar DOAS technique (five days centred on the full moon) serve to severely reduce nights in which combined analysis can be performed. Continued collection of both lunar and active DOAS measurement will be necessary in order to obtain a more accurate picture of the NO<sub>3</sub> vertical profile present at York University. Additionally, attempting this method of combined analysis of

NO<sub>3</sub> distribution in a dryer climate with reduced overall cloud cover would be a useful avenue of further research to explore, as it would drastically increase the available nights of measurement.

### **HONO at AMS13:**

HONO mixing ratios present in a forest clearing near the AMS13 site were collected and fit using a two-lamp fitting technique for full-day analysis from Aug 17<sup>th</sup>-Sept 4<sup>th</sup>. Based on the measurements, a diurnal profile of HONO was produced, which showed the expected nighttime elevation, followed by decreasing levels during the daylight hours due to photolysis. It was found that median nighttime HONO levels present at the site (0.20 ppb), as well as those of NO<sub>2</sub> (1.07ppb) were much lower than those seen at York University (1.0 ppb and 16 ppb respectively). Daytime HONO levels were found to be significantly higher than anticipated. Measured HONO levels at noon (133 ppt) found to be significantly higher than those calculated using the PSS assumption, even when the value of J<sub>HONO</sub> was reduced in order to account for light passing through the forest canopy. Furthermore, calculation of the overall contribution of HONO photolysis to daytime radical production found that HONO acted as the primary daytime OH radical source both in the early morning hours (83%) and during the entire day (42%). Both of these factors serve to indicate that a daytime HONO previously unaccounted for is present, and has a significant impact on the HONO level found to occur at the AMS13 site, in agreement with previous findings by other research groups. However, since the current dataset is limited only to the summer months (August-September), it is not effective at representing the annual profile of HONO mixing ratios present at AMS13. Thus, the next steps for further research would be to determine HONO levels during the winter months, and compare these findings with the data presented in this research.

## Chapter 6: References

- Allan, B., McFiggans, G., Plane, J. M. C., Coe, H., and McFayden, G. G.: The nitrate radical in the remote marine boundary layer, *Journal of Geophysical Research: Atmospheres*, **105**, 24191-24204, 2000.
- Alicke, B. et al.: OH formation by HONO photolysis during the BERLIOZ experiment, *Jour. Geophys. Res. Atmos.*, **108**, PHO 3-1-PHO 3-17, 2003.
- Aliwell, S.R and Jones, R.L., Measurement of Atmospheric NO<sub>3</sub> 1: Improved removal of water vapour absorption features in the analysis for NO<sub>3</sub>, *Geophys Res. Lett.*, **23**, vol. 19, pg 2585-2588, 1996.
- Amedro, D., Parker, A. E., Schoemaeker, C., and Fittschen, C.: Direct Observations of OH radicals after 565 nm multiphoton excitation of NO<sub>2</sub> in the presence of H<sub>2</sub>O, *Chemical Physics Letters*, **513**, 12-16, 2011.
- Amukudzi, L. K. et al.: Retrieval of stratospheric NO<sub>3</sub> vertical profiles from SCIAMACHY lunar occultation measurement over the Antarctic, *J. Geophys. Res.* **110**, D20304, 2005.
- Atkinson, R. et al.: Evaluated kinetic and photochemical data for atmospheric chemistry: Volume I-gas phase reactions of O<sub>x</sub>, HO<sub>x</sub>, NO<sub>x</sub> and SO<sub>x</sub> species, *Atmos. Chem. Phys.*, **4**, 1461-1738, 2004.
- Brown, S.S., et al.: Nocturnal odd-oxygen budget and its implications for ozone loss in the lower troposphere, *Geophys Res. Lett.*, **33**, L08801, doi:10.1029/2006GL025900, 2006.
- Brown, S.S. et al.: High resolution vertical distributions of NO<sub>3</sub> and N<sub>2</sub>O<sub>5</sub> through the nocturnal boundary layer, *Atmos. Chem. Phys.*, **7**, 139-149, 2007.
- Brown, S.S., de Grouw, J.A. et al.: *Atmos. Chem. Phys.*, **9**, 3027-3042, 2009.
- Brown, S.S. and Stutz, J.: Nighttime Radical Observations and Chemistry, *Chem. Soc. Rev.*, **41**, 6405-6447, 2012.
- Calvert, J. G., and Stockwell, W. R.: Deviations from the O<sub>3</sub> – NO- NO<sub>2</sub> photostationary state in the troposphere, *Canadian Journal of Chemistry*, **61**, 983-992, 1983.
- Cantrell, C.A., Calvert, J.G., Lind, J.A., Shetter, R.E., et al., Peroxy Radicals in the ROSE Experiment: Measurement and Theory, *Journ. Geophys. Res.*, **97**, 20671-20686, 1992.
- Dentener, F.J., and Crutzen, P.J.: Reaction of N<sub>2</sub>O<sub>5</sub> on tropospheric aerosols: Impact on the Global distributions of NO<sub>x</sub>, O<sub>3</sub> and OH, *Journal of Geophysical Research: Atmospheres*, **98**, 7149-7163, 1993.

- EC: Environment Canada, 2013 Nitrogen oxide emission and historical emission trends, <http://www.ec.gc.ca/indicateurs-indicators/default.asp?lang=en&n=0870FFFC-1>, 2013.
- Edwards, P.M., Young, C. J., McLaren, R.: Ozone photochemistry in an oil and natural gas extraction region during winter: simulations of a snow-free season in the Uintah Basin, Utah, *Atmos. Chem. Phys.*, **13**, 8955-8971, 2013.
- Elshorbany, Y.F. et al.: Impact of HONO on global atmospheric chemistry calculated with an empirical parameterization in the EMAC model. *Atmos. Chem. Phys.*, **12**, 9977-10000, 2012.
- Finlayson-Pitts, B. J. and Pitts Jr, J. N.: Chemistry of the upper and lower atmosphere: Theory, Experiments, and applications, Academic Press, 1999.
- Finlayson-Pitts, B. J. et al.: The heterogeneous hydrolysis of NO<sub>2</sub> in laboratory systems and in outdoor and indoor atmospheres: An integrated mechanism, *Phys. Chem. Chem. Phys.*, **5**, 223 -242, 2003.
- Friedelberg, C et al.: Derivation of tropospheric NO<sub>3</sub> profiles using off-axis differential optical absorption spectroscopy measurements during sunrise and comparison with simulations, *Journal of Geophysical Research*, **107**, 10.1029/2001JD000481, 2002.
- Halla, J.D.: The application of MAX-DOAS to the Measurement of Tropospheric Gases and Aerosols in Marine and Continental Environments. PHD Thesis, York University, Toronto, ON, June 2013.
- Hallquist, M., Stewart, D.J., Stephenson, S.K., Cox, R.A.: Hydrolysis of N<sub>2</sub>O<sub>5</sub> on sub-micron sulphate aerosols. *Phys. Chem. Chem. Phys.* **5**(16), 3453-3463, 2003.
- Harris, G. W. et al., An Investigation of the Dark Formation of Nitrous Acid in Environmental Chambers, *International Journal of Chemical Kinetics*, **16**(7), 919-939, 1984.
- Hauchcorne, A. et al.: First simultaneous global measurements of nighttime stratospheric NO<sub>2</sub> and NO<sub>3</sub> observed by Global Ozone Monitoring by Occultation of Stars (GOMOS)/Envisat in 2003, *J. Geophys. Res.* **110**, D18301, 2005.
- Hayden, K., Li, S.-M., Liu, P.S.K., O'Brien, J., **McLaren, R.**, Gordon, M., Darlington, A., Liggio, J., Mittermeier, R.L., Staebler, R., Makar, P., Stroud, C., Akingunola, A., Leithead, A., and Moussa S.G.: Determination of sulphate deposition from airborne measurements in the Oil Sands Region of Alberta, Canada, European Aerosol Conference, Milano, Italy, 3AAP\_P147, 2015.
- IPCC: Intergovernmental Panel on Climate Change (2014). Climate Change 2014 Basis. Cambridge University Press.

- Lal, M. et al., Atmospheric NO<sub>3</sub> Observations over Low-Latitude Northern Hemisphere During Night *J. Geophys. Res.*, VOL. **98**, NO. D12, pg 23,029-23,037, 1993.
- Leighton, P.A.: Photochemistry of Air Pollution. Academic, New York, 1961.
- Lenner, M.: Nitrogen dioxide in exhaust emissions from motor vehicles, *Atmospheric Environment*, **21**, 37-43, 1987.
- Levenburg, K.: A method for the solution of certain non-linear problems in least squares, *Quarterly of Applied Mathematics*, **2**, 164-168, 1944.
- Li, S., Matthews, J., and Sinha, A.: Atmospheric hydroxyl radical production from electronically excited NO<sub>2</sub> and H<sub>2</sub>O, *Science*, **319**, 1657-1660, 2008.
- Li, X. et al.: Missing Gas-Phase Source of HONO Inferred from Zeppelin Measurements in the Troposphere. *Science*, 344, 292-296, 2014
- Junkermann, W., Platt, U., Volz-Thomas, A.: A photoelectric detector for the measurement of photolysis frequencies of ozone and other atmospheric molecules, *J. Atmos. Chem*, **8**, 203-227, 1989.
- Kleinman, L. I. et al.: Photochemical age determinations in the Phoenix metropolitan area, *J. Geophys. Res.* **108**, doi:10.1029/2002JD002621, 2003.
- Kraus, S.: DOASIS: A Framework Design for DOAS, Ph.D. thesis, University of Mannheim, 2006.
- Kurtenbach, R. et al.: Investigation of emissions and heterogeneous of HONO in a road traffic tunnel, *Atmos. Chem. Phys.*, **35**, 3385-3394, 2001.
- McLaren, R., Wojtial, P., Majonis, D., McCourt, J., Halla, J. D., and Brook., J. NO<sub>3</sub> radical measurements in a polluted marine environment: links to ozone formation, *Atmos. Chem. Phys.*, **10**, 4187-4206, 2010
- Michoud, V. et al.: Study of the unknown HONO daytime source at a European suburban site during the MEGAPOLI summer and winter field campaigns, *Atmos. Chem. Phys.*, **14**, 2805-2822, 2014
- Middleton, J. T., Kendrick Jr, J., and Sudo, K.: Injury to herbaceous plants by smog or air pollution, *Plant Dis.:(United States)*, **34**, 1950.
- Mielke, L.H. et al.: Observation of ClNO<sub>2</sub> in a mid-continental urban environment, *Environ. Sci. Technol*, **45**(20), 8889-8896, 2011.
- Naudet, J.P., Rigaud P., and Pirre, M.: Altitude distribution of stratospheric NO<sub>3</sub> 1. Observations of NO<sub>3</sub> and related species, *J. Geophys. Res.*, **94**, 6374-6382, 1989.

- Norton, R. B., and J. F. Noxon: Dependence of stratospheric NO<sub>3</sub> upon latitude and season, *J. Geophys. Res.*, **91**, 5323–5330, 1986.
- Noxon, J. F., R. B. Norton, and Henderson, W. R.: Observation of atmospheric NO<sub>3</sub>, *Geophys. Res. Lett.*, **5**, 675, 1978.
- Noxon, J. F., Norton, R. B., and Henderson, W. R.: Comment on the problem of nighttime stratospheric NO<sub>3</sub> by Herman, J. R., *J. Geophys. Res.-Ocean. Atmos.*, **85**, 4556–4557, 1980.
- Orphal, J., Fellows, C. E., and Flaud, P.M: The visible absorption spectrum of NO<sub>3</sub> measured by high-resolution Fourier transform spectroscopy, *Journal of Geophysical Research*, **108**, 4077, 2003.
- Osthoff, H. D. et al.: Temperate dependence of the NO<sub>3</sub> absorption cross-section above 298K and determination of the equilibrium constant for NO<sub>3</sub> + NO<sub>2</sub> ↔ N<sub>2</sub>O<sub>5</sub> at atmospherically relevant conditions., *Phys. Chem. Chem. Phys.*, **9**, 5785-5793, 2007.
- Osthoff, H. D. et al.: High levels of nitryl chloride in the polluted subtropical marine boundary Layer, *Nature Geoscience*, **1**, 324-328, 2008.
- Osthoff, H. D. et al.: Values for *j*HONO, NO, *j*O(<sup>1</sup>D), and *j*HCHO, Personal correspondence, 2015.
- Perner, D., Ehhault, D. H., Pätz, H., W., Platt, U., Röth, E.P, and Volz, A.: OH – Radicals in the Lower Troposphere, *Geophys. Res. Lett.*, **3**, 466-468, 1976.
- Platt, U., Perner, D. et al.: Detection of NO<sub>3</sub> in the polluted troposphere by differential optical absorption, *Geophys. Res. Lett.*, **7**, 89-92, 1980.
- Platt, U., and Stutz J.: Differential Optical Absorption Spectroscopy Principles and Applications. Heidelberg, Germany: Springer Verlag Berlin Heidelberg, 2008.
- Poehler, D. DOASIS troubleshooting, Personal correspondence, 2015.
- Raff, J. D., Njagic, B., Chang, W. L., Gordon, M. S., Dabdub, D., Gerber R. B., and Finlayson-Pitts, B. J.: Chlorine activation indoors and outdoors via surface-mediated reactions of nitrogen oxides with hydrogen chloride, *Proceedings of the National Academy of Sciences*, **106**, 13647-13654, 2009.
- Renard, J. B., Taupan, F. B. et al.: Measurements and simulation of stratospheric NO<sub>3</sub> at mid and high latitudes in the Northern Hemisphere, *Journal of Geophysical Research*, **106**, NO. D23, 32,387-32,399, 2001.
- Renard, J. B., Taupan, F. B. et al.: NO<sub>3</sub> Vertical Profile Measurements from Remote Sensing Balloon-Borne Spectrometers and Comparison with Model Calculations, *Journal of Geophysical Research*, **51**, 65–78, 2005.

- Riedel, T.P. et al.: An MCM modeling study of nitryl chloride (ClNO<sub>2</sub>) impacts on oxidation, *Atmos. Chem. Phys.*, **14**, 3789–3800, 2014.
- Sander, S. P., Friedl, R. R., Golden, D. M., Kurylo, M. J., Moortgat, G. K., Keller-Rudek, H., Wine, P. H., Ravishankara, A. R., Kolb, C. E., Molina, M. J., Finlayson-Pitts, B. J., Huie, R. E., and Orkin, V. L.: Chemical Kinetics and Photochemical Data for Use in Atmospheric Studies, Evaluation Number 15, JPL Publication 06-2, Jet Propulsion Laboratory, Pasadena, CA, 2006.
- Sörgel, M. et al.: Quantification of the unknown HONO daytime source and its relation to NO<sub>2</sub>, *Atmos. Chem. Phys.*, **11**, 10433–10447, doi:10.5194/acp-11-10433-2011, 2011.
- Sörgel, M., Trebs, I., Wu, D., Held, A.: A comparison of measured HONO uptake and release with calculated source strengths in a heterogeneous forest environment, *Atmos. Chem. Phys.*, **15**, 9237–9251, 2015.
- Spataro, F., Ianniello, A.: Sources of atmospheric nitrous acid: State of the science, current research needs, and future prospect, *Journal of the Air & Waste Management Association*, **64**, 1232-1250, 2014.
- Stutz J.: Nocturnal Chemistry in the Urban Boundary Layer of Los Angeles: Final Report, Contract Number 08-318, 2014.
- Su, H. et al.: Observation of nighttime nitrous acid (HONO) formation at a non-urban site during PRIDE-PRD2004 in China, *Atmospheric Environment*, **42**, 6219-6232, 2008.
- Tang, Y., An, J., Wang, F., Li, Y., Qu, Y., Chen, Y., Lin, J.: Impacts of an unknown daytime HONO source on the mixing ratio and budget of HONO, and hydroxyl, hydroperoxyl, and organic peroxy radicals, in the coastal regions of China, *Atmos. Chem. and Phys.*, **15**, 9381-9398, 2015.
- Thomas, K., Volz-Thomas, A., Kley, D.: Zur Wechselwirkung von NO<sub>3</sub>-Radikalen mit wässrigen Lösungen: Bestimmung des Henry- und des Massenakkommodationskoeffizienten, Forschungszentrum Jülich, Dissertation K. Thomas Univ. Wuppertal D468, 2755, 1993.
- Thornton, J. A., et al.: A large atomic chlorine source inferred from mid-continental reactive nitrogen chemistry, *Nature*, **464**(7286), 271-274, 2010.
- Vairavamurthy, A., Roberts, J. M et al., Methods for determination of low molecular weight carbonyl compounds in the atmosphere a review, *Atmospheric Environment*, **26A**, 1965-1993, 1992.

Wagner, T. et al., DOAS moonlight observation of atmospheric NO<sub>3</sub> in the Arctic winter. *Geophys. Res. Lett.*, **20**, pg. 3441-3444, 2000.

Wheeler, M., J.: HCHO dataset, Personal correspondence, 2015.

Wojtala, P. R., Halla, J. D., and McLaren, R.: Pseudo steady states of HONO measured in the nocturnal marine boundary layer: a conceptual model for HONO formation on aqueous surfaces, *Atmos. Chem. Phys.*, **11**, pg. 3243-3261, 2011.

Wojtala, P. R.: Nocturnal Measurements of HONO, NO<sub>2</sub> and NO<sub>3</sub> by Differential Optical Absorption Spectroscopy in Polluted Marine and Urban Atmospheres, PHD Thesis, York University, Toronto, ON, December 2013.

VandenBoer, T. C., Brown, S. S., et al.: Understanding the role of the ground surface in HONO vertical structure: High resolution vertical profiles during NACHTT-11, *Journal of Geophysical Research: Atmospheres*. **118**, 10,155-110,171, 10.1002/jgrd.50721, 2013.

VandenBoer, T. C., Young C.J., et al.: Nocturnal loss and daytime source of nitrous acid through reactive uptake and displacement., *Nature Geoscience*, DOI:10.1038/NGEO2298, 2014.

Young, C.J. et al.: Vertically Resolved Measurements of Nighttime Radical Reservoirs in Los Angeles and Their Contribution to the Urban Radical Budget. *Environ. Sci. Technol.* **46**, 10965-10973, 2012.

Zeiss Microscopy Online Campus: Fundamentals of Xe Arc Lamps, <http://zeiss-campus.magnet.fsu.edu/articles/lightsources/xenonarc.html>, Accessed Aug 1<sup>st</sup>, 2015.

Zhou, X. et al.: Nitric acid photolysis on forest canopy surface as a source for tropospheric nitrous acid, *Nat. Geosci.*, **4**, 440-443, 2011.